3D Subject-Specific Shape and Density Modeling of the Lumbar Spine from 2D DXA Images for Osteoporosis Assessment

Mirella López Picazo

TESI DOCTORAL UPF / 2019

Directors de la tesi:

Prof. Miguel Ángel Gónzalez
Dr. Ludovic Humbert (Galgo Medical)

Department of Information and Communication Technologies

Directors:

Prof. Miguel Ángel González Ballester	*ICREA* Research Professor *Universitat Pompeu Fabra* Barcelona, Spain
Dr. Ludovic Humbert	Musculoskeletal Unit Director *Galgo Medical S.L.* Barcelona, Spain

This work was carried out in the research group Simulation, Imaging and Modeling for Biomedical Systems (SIMBioSys), at the Department of Information and Communication Technologies of BCN MedTech, Universitat Pompeu Fabra, Barcelona, Spain; and at the Musculoskeletal department of the company *Galgo Medical*, Barcelona, Spain.

This work was supported by: Industrial Doctorates program (*Generalitat de Catalunya*), QUAES Foundation - UPF Chair for Computational Technologies for Healthcare, *Programa Estatal de Investigación, Desarrollo e Innovación Orientada a los Retos de la Sociedad*, MINECO (Reference: RTC-2014-2740-1) and EuroStars program (Project ID: 9 140) funded by CDTI.

Lokah Samastah Sukhino Bhavantu

ABSTRACT/RESUMEN

Abstract - Osteoporosis is the most common bone disease, with a significant morbidity and mortality caused by the increase of bone fragility and susceptibility to fracture. Dual Energy X-ray Absorptiometry (DXA) is the gold standard technique for osteoporosis and fracture risk evaluation at the spine. However, the standard analysis of DXA images only provides 2D measurements and does not differentiate between bone compartments; neither specifically assess bone density in the vertebral body, which is where most of the osteoporotic fractures occur. Quantitative Computed Tomography (QCT) is an alternative technique that overcomes limitations of DXA-based diagnosis. However, due to the high cost and radiation dose, QCT is not used for osteoporosis management.

In this thesis, a method providing a 3D subject-specific shape and density estimation of the lumbar spine from a single anteroposterior DXA image is proposed. The method is based on a 3D statistical shape and density model built from a training set of QCT scans. The 3D subject-specific shape and density estimation is obtained by registering and fitting the statistical model onto the DXA image. Cortical and trabecular bone compartments are segmented using a model-based algorithm. 3D measurements are performed at different vertebral regions and bone compartments. The accuracy of the proposed methods is evaluated by comparing DXA-derived to QCT-derived 3D measurements.

Two case-control studies are also performed: a retrospective study evaluating the ability of DXA-derived 3D measurements at lumbar spine to discriminate between osteoporosis-related vertebral fractures and control groups; and a study evaluating the association between DXA-derived 3D measurements at lumbar spine and osteoporosis-related hip fractures. In both studies, stronger associations are found

between osteoporosis-related fractures and DXA-derived 3D measurements compared to standard 2D measurements.

The technology developed within this thesis offers an insightful 3D analysis of the lumbar spine, which could potentially improve osteoporosis and fracture risk assessment in patients who had a standard DXA scan of the lumbar spine without any additional examination

Resumen - La osteoporosis es la enfermedad ósea más común, con una morbilidad y mortalidad significativas causadas por el aumento de la fragilidad ósea y la susceptibilidad a las fracturas. La absorciometría de rayos X de energía dual (DXA, por sus siglas en inglés) es la técnica de referencia para la evaluación de la osteoporosis y del riesgo de fracturas en la columna vertebral. Sin embargo, el análisis estándar de las imágenes DXA solo proporciona mediciones 2D y no diferencia entre los compartimentos óseos; tampoco evalúa la densidad ósea en el cuerpo vertebral, que es donde se producen la mayoría de las fracturas osteoporóticas. La tomografía computarizada cuantitativa (QCT, por sus siglas en inglés) es una técnica alternativa que supera las limitaciones del diagnóstico basado en DXA. Sin embargo, debido al alto costo y la dosis de radiación, la QCT no se usa para el diagnóstico de la osteoporosis.

En esta tesis, se propone un método que proporciona una estimación personalizada de la forma 3D y la densidad de la columna vertebral en la zona lumbar a partir de una única imagen DXA anteroposterior. El método se basa en un modelo estadístico 3D de forma y densidad creado a partir de un conjunto de entrenamiento de exploraciones QCT. La estimación 3D personalizada de forma y densidad se obtiene al registrar y ajustar el modelo estadístico con la imagen DXA. Se segmentan los compartimentos óseos corticales y trabeculares utilizando un algoritmo basado en modelos. Se realizan mediciones 3D en diferentes regiones vertebrales y compartimentos óseos. La precisión de los métodos propuestos se evalúa comparando las mediciones 3D derivadas de DXA con las derivadas de QCT.

También se realizan dos estudios de casos y controles: un estudio retrospectivo que evalúa la capacidad de las mediciones 3D derivadas de DXA en la columna lumbar para discriminar entre sujetos con fracturas vertebrales relacionadas con la osteoporosis y sujetos control; y un estudio que evalúa la asociación entre las mediciones 3D derivadas de DXA en la columna lumbar y las fracturas de cadera relacionadas con la osteoporosis. En ambos estudios, se encuentran asociaciones más fuertes entre las fracturas relacionadas con la osteoporosis y las mediciones 3D derivadas de DXA en comparación con las mediciones estándar 2D.

La tecnología desarrollada dentro de esta tesis ofrece un análisis en 3D de la columna lumbar, que podría mejorar la evaluación de la

osteoporosis y el riesgo de fractura en pacientes que se sometieron a una exploración DXA estándar de la columna lumbar sin ningún examen adicional.

CONTENTS

ABSTRACT/RESUMEN **VII**

LIST OF FIGURES **XVI**

LIST OF TABLES **XVIII**

ACRONYMS **XIX**

1. INTRODUCTION **1**

1.1. CLINICAL CONTEXT **3**

1.2. METHODOLOGICAL CONTEXT **3**

1.3. INSTITUTIONAL CONTEXT **4**

1.3.1. GALGO MEDICAL S.L. 5

1.3.2. 3D-SHAPER® 5

1.3.3. EUROSTARS PROJECT 6

1.4. AIM AND OBJECTIVES OF THIS THESIS **7**

1.5. OUTLINE OF THE THESIS **8**

2. CLINICAL BACKGROUND **9**

2.1. SPINE **11**

2.2. VERTEBRAE **11**

2.3. BONE **12**

2.3.1. CORTICAL AND TRABECULAR BONE 12

2.3.2. BONE THROUGH LIFE 14

2.4. OSTEOPOROSIS 15

2.5. OSTEOPOROSIS-RELATED FRACTURES 17

2.6. DIAGNOSTIC METHODS AND TOOLS 19

2.6.1. DUAL ENERGY X-RAY ABSORPTIOMETRY 19

2.6.2. QUANTITATIVE COMPUTED TOMOGRAPHY 22

2.6.3. COMPLEMENTARY DIAGNOSTIC TOOLS 24

2.7. CLINICAL CHALLENGES 25

3. METHODOLOGICAL BACKGROUND 27

3.1. STATISTICAL MODELS 29

3.1.1. SHAPE MODELS 29

3.1.2. APPEARANCE MODELS 37

3.1.3. INDIVIDUAL AND GLOBAL MODELS 41

3.2. 3D SUBJECT-SPECIFIC SHAPE AND INTENSITY MODELLING FROM 2D IMAGES 42

3.2.1. FEATURE-BASED METHODS 43

3.2.2. INTENSITY-BASED METHODS 45

3.3. METHODOLOGICAL CHALLENGES 47

4. 3D SUBJECT-SPECIFIC SHAPE AND DENSITY ESTIMATION OF THE LUMBAR SPINE FROM A SINGLE ANTEROPOSTERIOR DXA IMAGE INCLUDING ASSESSMENT OF CORTICAL AND TRABECULAR BONE 49

4.1. INTRODUCTION 51

4.2. MATERIALS AND METHODS 52

4.2.1. STUDY SUBJECTS AND MEDICAL IMAGES 52

4.2.2. STATISTICAL SHAPE AND DENSITY MODEL GENERATION 53

4.2.3. 3D SUBJECT-SPECIFIC SHAPE AND DENSITY ESTIMATION FROM DXA IMAGES 61

4.2.4. GEOMETRICAL AND BONE MINERAL DENSITY MEASUREMENTS 64

4.2.5. VALIDATION METHOD 66

4.3. RESULTS 68

4.3.1. SHAPE ACCURACY 68

4.3.2. CORTICAL THICKNESS AND DENSITY DISTRIBUTION 68

4.3.3. CLINICAL MEASUREMENTS 69

4.4. DISCUSSION 74

4.5. CONCLUSION 78

5. DISCRIMINATION OF OSTEOPOROSIS-RELATED VERTEBRAL FRACTURES BY DXA-DERIVED 3D MEASUREMENTS: A RETROSPECTIVE CASE-CONTROL STUDY 79

5.1. INTRODUCTION 81

5.2. MATERIALS AND METHODS 83

5.2.1. STUDY POPULATION 83

5.2.2. MEDICAL IMAGES AND DXA-DERIVED 2D MEASUREMENTS 84

5.2.3. DXA-DERIVED 3D MEASUREMENTS 84

5.2.4. STATISTICAL ANALYSIS 85

5.3. RESULTS 86

5.3.1. SUBJECT´S CHARACTERISTIC 86

5.3.2. DXA-DERIVED 2D MEASUREMENTS 86

5.3.3. DXA-DERIVED 3D MEASUREMENTS 87

5.3.4. SUBGROUP ANALYSIS 89

5.4. DISCUSSION 95

5.5. CONCLUSIONS 99

6. ASSOCIATION BETWEEN OSTEOPOROTIC FEMORAL NECK FRACTURES AND DXA-DERIVED 3D MEASUREMENTS AT LUMBAR SPINE: A CASE-CONTROL STUDY 101

6.1. INTRODUCTION 103

6.2. MATERIALS AND METHODS 105

6.2.1. STUDY POPULATION 105

6.2.2. MEDICAL IMAGES AND DXA-DERIVED 2D MEASUREMENTS 105

6.2.3. DXA-DERIVED 3D MEASUREMENTS 106

6.2.4. STATISTICAL ANALYSIS 106

6.3. RESULTS 107

6.3.1. POPULATION CHARACTERISTICS 107

6.3.2. DIFFERENCES IN DXA-DERIVED MEASUREMENTS BETWEEN SUBJECTS WITH AND WITHOUT FRACTURES 107

6.3.3. ASSOCIATION BETWEEN DXA-DERIVED MEASUREMENTS AND HIP FRACTURE 107

6.3.4. ANATOMICAL DISTRIBUTION OF DIFFERENCES BETWEEN GROUPS 111

6.4. DISCUSSION 111

6.5. CONCLUSION 116

7. CONCLUSION 117

7.1. OVERVIEW 119

7.2. OUTLOOK AND FUTURE WORK 121

APPENDICES 129

A. SEGMENTATION 129

B. CLINICAL MEASUREMENTS 133

REFERENCES 137

ACKNOWLEDGEMENTS XXI

PUBLICATIONS XXIII

CURRICULUM VITAE XXV

LIST OF FIGURES

Figure 1.1: 3D-Shaper® technology applied to the femur (*Galgo* Medical S.L., Barcelona, Spain). 7

Figure 2.1: Main regions of the spine. 12

Figure 2.2: Main regions of the lumbar vertebra. 13

Figure 2.3: Trabecular and cortical bone compartments at the lumbar vertebra. 14

Figure 2.4: Differences between a normal and an osteoporotic bone. 17

Figure 2.5: Classification of vertebral fractures by Genant [43]. 20

Figure 2.6: Commercial DXA equipment to diagnose osteoporosis. 22

Figure 2.7: Volumetric QCT scan of the lumbar spine. 23

Figure 3.1: Statistical shape model of the lumbar spine. 36

Figure 3.2: Active Shape Models. 38

Figure 4.1: Close ups of AP DXA and QCT images. 54

Figure 4.2: Flowchart describing spine shape alignment. 57

Figure 4.3: Lumbar spine volume alignment. 59

Figure 4.4: Model instance generation. 61

Figure 4.5: 3D-2D registration process. 62

Figure 4.6: Model-based algorithm used to segment the cortical layer. 65

Figure 4.7: Comparison of the DXA-derived and QCT-derived 3D subject-specific shape and density of the lumbar spine for three subjects selected as examples. 67

Figure 4.8: Comparison of DXA-derived and QCT-derived cortical thickness distribution for the three subjects selected as examples. 71

Figure 4.9: Linear regressions between DXA and QCT-derived vBMD assessed in the L1-L4 segment for different regions of interest. 73

Figure 4.10: Workflow of the proposed method. 75

Figure 4.11: Screenshot of the developed method integrated into 3D-Shaper®. 76

Figure 5.1: Anatomical distribution of the average changes (difference between subjects included the fracture group and subgroups, and controls) in trabecular vBMD. 90

Figure 5.2: AUC map calculated using trabecular vBMD at each voxel of the volumetric images of subjects included in the fracture group and controls. 92

Figure 5.3: Cortical sBMD at the vertebral body. 94

Figure 6.1: Anatomical distribution of the average differences in vBMD between subjects included the fracture group and controls. . 112

Figure 6.2: AUC map calculated using vBMD at each voxel of the volumetric images of subjects included in the fracture group and controls. 113

Figure 6.3: Cortical sBMD at the vertebral body. 114

Figure A. 1: Pre-processing filters pipeline. 130

Figure A. 2: Comparison of QCT volumes before and after pre-processing filters for the three subjects selected as examples. 131

Figure A. 3: Segmented QCT volumes before and after smoothing for the three subjects selected as examples 132

LIST OF TABLES

Table I: Shape Accuracy. 69

Table II: DXA and QCT-derived cortical thickness and density measurements. 70

Table III: DXA and QCT-derived clinical measurements at L1-L4 segment. 72

Table IV: Characteristics at baseline of the subjects included in fracture and control groups according to fracture site. 87

Table V: Vertebral fracture (whole database): DXA-derived measurements at baseline of control and fracture groups, differences between groups, AUC and OR. 88

Table VI: Subgroups analysis according to fracture site: DXA-derived measurements at baseline of subjects included in the control and fracture groups, differences between groups, AUC and OR. 93

Table VII: Characteristics of the subjects included in fracture and control groups. 108

Table VIII: DXA-derived 2D measurements of control and fracture groups, differences between groups, AUC and OR. 109

Table IX: DXA-derived 3D measurements of control and fracture groups, differences between groups, AUC and OR. 110

Table X. DXA and QCT-derived clinical measurements at L1, L2, L3, L4 and L1-L4 segment. 133

ACRONYMS

2D	2-Dimensional
3D	3-Dimensional
aBMD	Areal Bone Mineral Density
AAM	Active Appearance Model
AP	Anteroposterior (projection)
ASM	Active Shape Model
AUC	Area Under Curve
BMC	Bone Mineral Content
BMD	Bone Mineral Density
BMI	Body Mass Index
CI	Confidence Interval
CPD	Coherent Point Drift
CT	Computed Tomography
CTh	Cortical Thickness
DRR	Digitally Reconstructed Radiograph
DXA	Dual-energy X-ray Absorptiometry
GMM	Gaussian Mixture Models
GPA	Generalized Procrustes Analysis
ICP	Iterative Closest Point
ISCD	International Society for Clinical Densitometry
OR	Odds Ratio
PCA	Principal Component Analysis
PDM	Point Distribution Model
QCT	Quantitative Computed Tomography
QUS	Quantitative ultrasound
SAM	Statistical Appearance Model
SSM	Statistical Shape Model
sBMD	Surface Bone Mineral Density
ROI	Region of Interest
SD	Standard Deviation

TPS	Thin Plate Spline
vBMD	Volumetric Bone Mineral Density
VFA	Vertebral Fractures Assessment
WHO	World Health Organization

Chapter 1

1. INTRODUCTION

This chapter first describes the clinical, methodological and institutional context within which this thesis is carried out. Then, the aim, objectives, and outline of the thesis are described.

1.1. Clinical context

Osteoporosis is the most common bone disease characterized by low bone mass and microarchitectural deterioration of bone tissue [1], [2]. The absence of symptoms in the early stage leads to millions of people remaining undiagnosed and untreated, increasing their bone fragility and susceptibility to fracture. Worldwide, 1 in 3 women and 1 in 5 men aged over 50 years old experience osteoporosis-related fractures [3], [4]. The most common osteoporosis-related fractures occur at the spine, although can occur at almost any bone.

Nowadays, the gold standard for osteoporosis diagnosis and fracture risk assessment at the spine is Dual Energy X-ray Absorptiometry (DXA). This technique supplies 2-Dimensional (2D) images with information about areal Bone Mineral Density (aBMD), but without information about 3-Dimensional (3D) shape, size or mineral content distribution of bones. The standard analysis of DXA images neither differentiates between bone compartments (integral, trabecular or cortical bone) or vertebral regions (vertebral body or posterior vertebral elements). Therefore, numerous patients with bone fragility are not diagnosed as such. Quantitative Computed Tomography (QCT) is an alternative technique that overcomes limitations of DXA-based diagnosis. However, due to the high cost and radiation dose, QCT is not used for osteoporosis management.

To overcome current clinical limitations, this thesis proposes the development of methods to analyze in 3D the shape and density of the lumbar spine using 2D DXA images.

1.2. Methodological context

Human anatomy presents high similarity across individuals, but at the same time inter-subject variations are of importance and must be considered for subject-specific analysis. Statistical modeling approaches proposed by Cootes *et al.* [5]–[12] focus on capturing the variability within a population from a training set of data. Statistical models can be fitted to the range of variation found in the type of object which it is modeling, but only deforms in ways implied by the training set. The

objective is to build statistical models that could be used to characterize and interpret similar structures in new data.

In the literature, methods are proposed to estimate the 3D subject-specific shape of the proximal femur from several X-ray images using statistical shape models and 3D-2D registration methods [13]–[15]. Other methods are proposed to estimate, in addition to bone shape, the BMD distribution from DXA images [16]–[18]. In [19] and [20], besides estimating the 3D subject-specific shape and BMD distribution of the proximal femur from a DXA image, different approaches are developed to provide a separate assessment of the cortical and trabecular bone.

However, applying such methodologies to obtain a 3D subject-specific shape and BMD estimation of the lumbar spine from DXA scans is not straightforward. In [21], a method to obtain 3D subject-specific estimates of the lumbar spine (from L2 to L4) using two DXA images (anteroposterior and lateral views) and a statistical shape and density model of each vertebra is proposed. However, no specific algorithm is proposed to quantify the cortical bone. Moreover, lateral DXA scans are not currently used in clinical practice for osteoporosis screening due to high precision errors [22].

To the best of our knowledge, no method has been reported in the literature to model the shape and density of the lumbar spine and the cortical and trabecular bone, using a single anteroposterior (AP) DXA scan. To overcome current methodological limitations, this thesis proposes the development and validation of methods providing 3D subject-specific shape and density estimations of the lumbar spine from a single AP DXA image. The method is based on a 3D statistical shape and density model that is registered onto the DXA image. Cortical and trabecular bone compartments are segmented using a model-based algorithm. 3D measurements are performed at different vertebral regions and bone compartments.

1.3. Institutional context

The present thesis was carried out in the framework of Industrial Doctorate, under the supervision of Prof. Miguel Ángel González Ballester, ICREA Research Professor at the Department of Information and Communication Technologies of *Universitat Pompeu Fabra* (UPF) in Barcelona, and Dr. Ludovic Humbert, Musculoskeletal Unit Director at

Galgo Medical S.L, in Barcelona.

The Industrial Doctorates Plan(http://doctoratsindustrials.gencat.cat/) is promoted by the *Generalitat de Catalunya* and helps companies to improve their competitiveness and productivity by making better use of knowledge, technology and skills within universities, colleges and research organizations.

Furthermore, the work in this thesis was performed within the framework of the EuroStars Project "3D-DXA Spine: 3D reconstruction of the shape and bone mineral density distribution of the spine from 2D DXA images", a European project including *Galgo Medical*, *CETIR Grup Mèdic* and *DMS Group*.

1.3.1. Galgo Medical S.L.

Galgo Medical S.L. (www.galgomedical.com) is a medical imaging software development company, spin-off from UPF, created in July 2013 and based in Barcelona. *Galgo Medical* currently works in four medical disciplines:

- Musculoskeletal imaging.
- Vascular interventional radiology planning.
- Interventional cardiology for arrhythmia treatment.
- Image-guided neurosurgical planning and navigation.

This thesis is part of the work of the Musculoskeletal imaging group, which develops the 3D-Shaper® software.

1.3.2. 3D-Shaper®

The musculoskeletal imaging group of *Galgo Medical* develops software solutions for advanced analysis of bony structure to improve the management of musculoskeletal diseases. *Galgo* has developed 3D-Shaper® (www.3d-shaper.com): a software solution that provides 3D subject-specific analysis of bony structures from DXA images (**Figure 1.1**). 3D-Shaper® provides additional information about the 3D geometry and bone mineral distribution that can be used to improve osteoporosis management.

The 3D modeling algorithm integrated into 3D-Shaper® have been mainly applied to the femur [20] and validated in collaboration with

several clinical centers, and in particular with *CETIR Grup Medic* [23], [24]. Lumbar spine and femur are preferred areas to measure bone density for diagnosis and management of osteoporosis. In this thesis, we will further develop the algorithm integrated into 3D-Shaper® for the femur to include the lumbar spine. However, this extension is far from being trivial (details can be found in Section 3.3).

Apart from the 3D-Shaper® software developed by *Galgo* Medical, there is no technology in the market that analyzes the 3D bony structure in 3D from DXA scans. A software to analyze the lumbar spine in 3D from clinical practice DXA scans could be a game changer in the bone densitometry market, as it could potentially improve the management of osteoporosis and fracture risk prevention.

1.3.3. EuroStars project

This thesis was also performed in the framework of a EuroStars project (Project ID: 9 104 "3D-DXA Spine: 3D reconstruction of the shape and bone mineral density distribution of the spine from 2D DXA images"). This project involved 3 entities with a very specific and complementary know-how: *Galgo Medical,* which is a company specialized in algorithm and software development for in medical imaging; *CETIR Grup Mèdic* (Barcelona, Spain) which is a medical center with a large experience in bone densitometry; and *DMS* (Mauguio, France) which is a leading manufacturer of DXA scanners.

This EuroStars project aims at developing a technology which will provide physicians with a 3D subject-specific estimation of the shape and bone mineral content of the lumbar spine from DXA images. The 3D-Shaper Spine product includes:

- An image acquisition protocol and a device to ensure the correct positioning of the patients on DXA scanner.
- An algorithm generating a 3D spine's subject-specific estimation from DXA images.
- A software integrating the 3D-2D registration algorithm and an innovative user interface to visualize the data and help the physician to exploit these data in clinical routine.
- A hardware solution embedding the 3D-2D registration software.

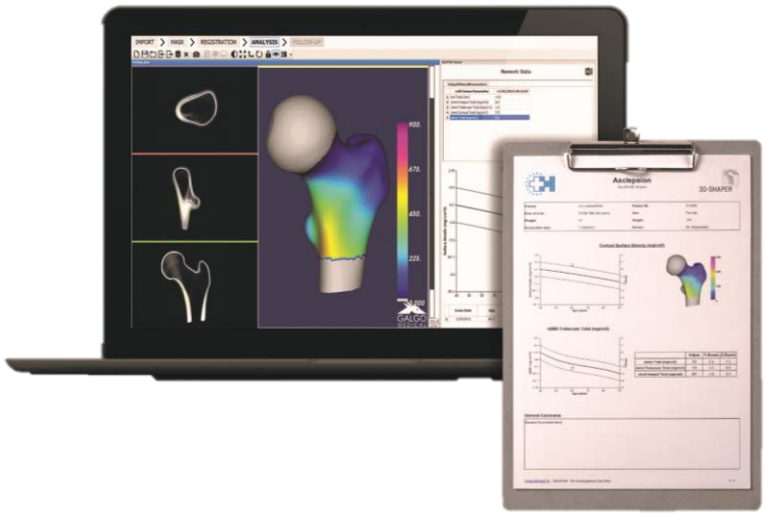

Figure 1.1: 3D-Shaper® technology applied to the femur (*Galgo* Medical S.L., Barcelona, Spain).

This thesis was in line with one of the work packages of the EuroStars project lead by *Galgo Medical*: the development and validation of a software for estimating the 3D subject-specific lumbar spine from 2D-DXA images.

1.4. Aim and objectives of this thesis

The aim of this thesis is the development and clinical evaluation of methods to analyze in 3D the bone shape and density of the lumbar spine, using 2D DXA images. This aims to provide an insightful 3D analysis of the lumbar spine from clinical practice imaging modality, which could potentially improve osteoporosis and fracture risk assessment in patients who had a DXA scan of the lumbar spine without any additional examination.

This thesis has been structured around the following specific objectives:

- To develop a method for the construction of a statistical shape a density model of the lumbar spine from a database of QCT images.
- To develop a method for the 3D subject-specific shape and density modeling of the lumbar spine from a single DXA image using statistical models and 3D-2D registration algorithms.

- To develop a method to provide clinical measurements at different vertebral regions and bone compartments using the 3D subject-specific model of the lumbar spine.
- To validate the accuracy of the DXA-derived 3D subject-specific shape and density models and measurements, in comparison with QCT.
- To evaluate the association of DXA-derived cortical and trabecular measurements at lumbar spine with osteoporosis-related vertebral fractures.
- To evaluate the association of DXA-derived cortical and trabecular measurements at lumbar spine with osteoporosis-related hip fractures.

1.5. Outline of the thesis

The core contents of this thesis are presented in five chapters.

Chapter 2 describes the clinical background of this thesis. Osteoporosis disease, its main clinical consequence (the fracture) and the main diagnostic methods are described.

Chapter 3 reviews the main concepts and methods used in this thesis, focusing on the description of statistical model generation and registration.

Chapter 4 proposes a method to provide a 3D subject-specific estimation of the lumbar spine, including personalized shape and bone density distribution from a single AP DXA image using a statistical model and a 3D-2D registration algorithm.

Chapter 5 evaluates the association of DXA-derived 3D measurements at lumbar spine with osteoporosis-related vertebral fractures.

Chapter 6 evaluates the association between transcervical hip fractures and DXA-derived 3D measurements at lumbar spine.

Finally, **Chapter 7** concludes the thesis and discusses the outlook and future work.

Chapters 4,5,6 are self-contained, and are adapted from articles that have been published or are under review in peer-reviewed journals.

Chapter 2

2. CLINICAL BACKGROUND

This chapter describes the clinical background of this thesis. First, the anatomy of the spine and bone structure is presented. Then, osteoporosis and its main clinical consequence – the fracture- are described. Last, the main methods and tools for osteoporosis and fracture risk assessment are briefly introduced.

2.1. Spine

The spine consists of 26 vertebral bones connected to each other by ligaments and muscles. The spine provides structural support and balance for the head and trunk of the body to maintain an upright posture; protects the spinal cord, nerve roots and several of the body's internal organs; provides connecting points for the ribs and muscles; and enables flexible motion.

The 26 vertebral bones are divided into 4 main regions (**Figure 2.1**): the cervical spine, the thoracic spine, the lumbar spine, and the sacral spine. The cervical spine is composed by 7 vertebrae, from C1 through C7 (top to bottom). Cervical vertebrae protect the brain stem and the spinal cord, support the skull and allow for a wide range of head movements. The thoracic spine is composed by 12 vertebrae, from Th1 through Th12 (top to bottom). Thoracic vertebrae are connected to the ribs and protect vital organs. The lumbar spine is composed by 5 vertebrae, from L1 through L5 (top to bottom). The lumbar spine has more range of motion than the thoracic spine, but less than the cervical spine. The sacral spine is composed by sacrum and coccyx, which are composed in turn by 5 fused vertebrae. The lower portion of the spine holds most of the body's weight. However, each segment relies upon the strength of the others to function properly.

2.2. Vertebrae

A vertebra can be divided into two main parts (**Figure 2.2**): vertebral body and posterior vertebral elements. The vertebral body has an irregular cylindrical shape, with a range of variations depending on the type of vertebra. It provides structural support for the head and trunk of the body. The posterior vertebral elements are the pedicles, laminae, transverse processes, articular processes, and spinous process. The pedicles protrude from the back of the vertebral body and connect the vertebral body to the processes. The pedicles and the laminae, also called vertebral arch, encase the spinal cord and its coverings. The

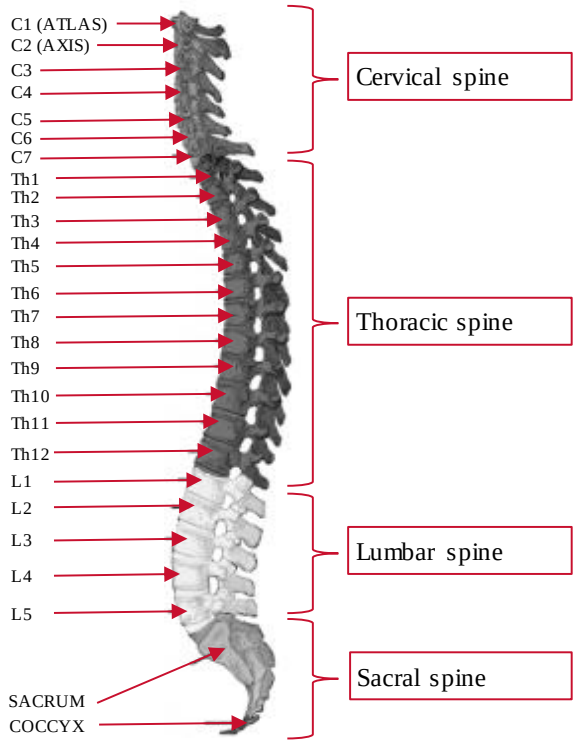

Figure 2.1: Main regions of the spine.

articular, transverse and spinous processes are projected from the laminae and are where muscle and ligaments attach enabling the articulation between vertebrae. The articular processes determine the direction of motion and restrict abnormal movement.

The vertebral body is weight bearing, shock absorbing, and supportive; and it plays an essentially static role. However, the posterior vertebral elements are non-weight-bearing but play an essentially dynamic role.

2.3. Bone

2.3.1. Cortical and trabecular bone

Bones are made of highly dynamic and metabolic active tissue, with an excellent capacity for self-repair and alter their properties in response to changes in mechanical demand. Bones are composed of 30% of organic materials, such as collagen, which provide flexibility and resilience; and 70% of inorganic materials, such as minerals, which provide strength

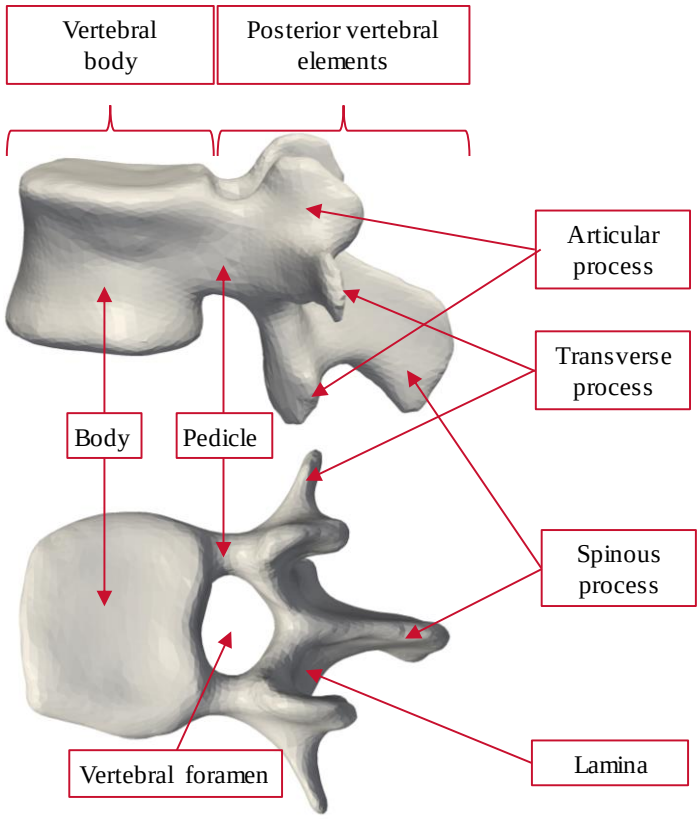

Figure 2.2: Main regions of the lumbar vertebra.

and stiffness. Organic and inorganic materials are not homogeneously distributed inside the bone. In fact, we can differentiate two main parts in bones: an outer compact shell, called cortical or compact bone; and a porous inner, called trabecular or cancellous bone (**Figure 2.3**).

Cortical bone is strong, dense and tough. It is responsible for providing mechanical and metabolic functions. Cortical bone consists of multiple microscopic columns, called osteons. Each osteon is formed by multiple layers of osteoblasts and osteocytes around a central canal called the Haversian canal. The columns are connected by Volkmann's canals. Cortical bone accounts for 80% of the total bone mass of an adult human skeleton. The outer shell formed by the cortical bone is called cortex. The outer surface of the cortex is covered by a periosteum and the inner surface by an endosteum. The endosteum is the boundary between the cortical bone and the trabecular bone.

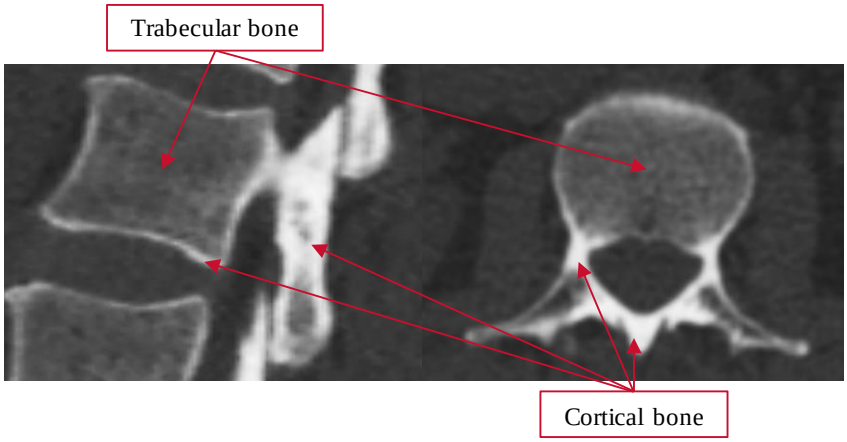

Figure 2.3: Trabecular and cortical bone compartments at the lumbar vertebra.

Trabecular bone is formed by a less dense tiny lattice-shaped structure. Thin formations of osteoblasts covered in the endosteum create an irregular network of spaces, known as trabeculae. Within these spaces are bone marrow and hematopoietic stem cells. Trabecular marrow is composed of a network of rod- and plate-like elements that make the overall organ lighter and allow room for blood vessels and marrow. Trabecular bone accounts for the remaining 20% of total bone mass but has nearly ten times the surface area of cortical bone.

The vertebral body is formed mostly by trabecular bone (80% of the volume) and covered with a thin cortical shell (20% of the volume). The posterior vertebral elements have thicker coverings of cortical bone. The pedicles are made of strong cortical bone.

2.3.2. Bone through life

Bones are constantly regenerated themselves throughout life (most of the adult skeleton is replaced about every 10 years). The regeneration process consists of two main antagonistic proceedings: resorption and formation. In the resorption stage, bone resorbing cells (osteoclasts) digest the existing bone matrix; whereas in the formation stage, bone forming cells (osteoblasts) deposit calcium phosphate over the bone surface and synthesize extracellular matrix around.

During childhood and adolescence bones are sculpted by modeling. This process allows individual bones to grow in size and to shift in

space. During childhood, bones grow because resorption occurs inside the bone while formation of new bone occurs on its outer surface of the cortex. During adolescence, bones get thicker because formation occurs on both the outer and inner surfaces of the cortex. Bones reach their peak mass typically by early 20s. Women achieve a lower peak bone mass than men [25].

Once in adulthood, bones are sculpted by remodeling. In the remodeling process, resorption occurs on inner surfaces while formation occurs on outer surfaces, which can partially compensate for the loss of strength due to the thinning of the cortex.

In healthy young adults, the overall amounts of resorbed and formed bone are balanced. The maintenance of the remodeling cycle in balance contributes keeping bones in strength and with a stable bone mass. However, sometimes building cells fail to form enough new bone or destructive cells dissolve too much, leading to a thinner shell and more porous inner than in a normal bone, **Figure 2.4**. This imbalance is the cause of osteoporosis disease.

2.4. Osteoporosis

Osteoporosis is derived from Greek, which literally means a bone with holes. It is defined by the World Health Organization (WHO) as "a systemic skeletal disease characterized by low bone mass and microarchitectural deterioration of bone tissue with a consequent increase in bone fragility and susceptibility to fracture" [1].

The WHO recommends the evaluation of Bone Mineral Density (BMD) to diagnose osteoporosis [2], [25], [26]. BMD is a measure that quantifies the grams of bone mineral per area (aBMD) or volume (vBMD).

The BMD is used to calculate the T-score, Eq.(1). This measure reveals how the resulting individual BMD deviates from a BMD reference measurement obtained in a healthy young adult population, represented by its mean and standard deviation (SD).

$$T - score = \frac{Measured\ BMD - Young\ adult\ mean\ BMD}{Young\ adult\ populaton\ SD} \quad (1)$$

The diagnosis criteria established by the T-score for diagnosing osteoporosis disease on postmenopausal women and men aged 50 years are [26]:

- Normal bone mass (Healthy): T-score ≥ -1 SD
- Low bone mass (Osteopenia): -1 SD > T-score > -2.5 SD
- Osteoporosis: T-score ≤ -2.5 SD

The International Society for Clinical Densitometry (ISCD) recommends using the projected density along the anteroposterior direction to diagnose osteoporosis at the lumbar spine [22]. The BMD should be measured at the lumbar spine, total hip, or femoral neck. The T-score of other regions should not be used for diagnosis according to the Adult Official Positions of the ISCD [22]. The WHO BMD diagnostic classification based on T-scores should not be applied in premenopausal women, men less than 50 years of age and children. In these groups, the ISCD recommends instead the use of the Z-score. The Z-score describes how the individual BMD deviates from the mean value expected for age and sex.

Osteoporosis is considered a "silent disease" since there is no evidence that bone loss itself causes any symptoms. Both women and men are likely to suffer osteoporosis, though several risk factors such as age, low body-mass index, previous fragility fractures, family history of fractures, glucocorticoid use, rheumatoid arthritis, or smoking, alcohol and poor calcium intake [27], [28]. However, osteoporosis is more common in women than in men, partly because women have a lower peak bone mass and partly because of the hormonal changes that occur at the menopause [25].

Estrogens have an important function in preserving the balance between the overall amounts of resorbed and formed bone. With aging, usually from around the age of 50 years and especially in women during menopause, estrogen levels decline. Consequently, the remodeling balance becomes negative, resulting in a decreased bone mass. Therefore, menopausal transition has turned out to be an evident trigger of an earlier expression of osteoporosis as well [29].

A distinction is made in the literature between the causes of osteoporosis. So-called primary osteoporosis is explained by the normal changes due to the aging process, as well as the hormonal changes at

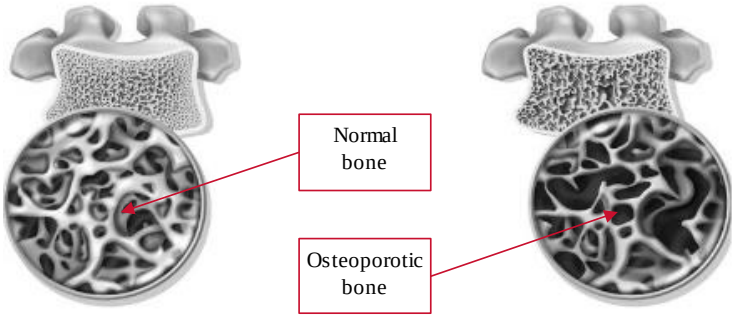

Figure 2.4: Differences between a normal and an osteoporotic bone. Adapted from International Osteoporosis Foundation [166].

menopause in women, whereas secondary osteoporosis is caused by other pathologies as: genetic, endocrine, gastrointestinal, hematologic, rheumatologic, nutritional, pharmacological diseases, or a combination of them.

Osteoporosis is the most common and costly bone disease: approximately 22 million women and 5.5 million men older than 50 years are estimated to have osteoporosis in the EU [30]. However, the absence of symptoms in the early stage leads to millions of people remaining undiagnosed and untreated [31], increasing their probabilities to suffer from a fracture. In fact, most people are diagnosed with osteoporosis after they suffer a bone fracture, the worst clinical consequence of osteoporosis.

2.5. Osteoporosis-related fractures

Each year 8.9 million osteoporosis-related fractures occur, resulting in a fracture every 3 seconds [32]. The estimated cost of osteoporosis-related fractures in the EU in 2010 was €37 billion [33]. A cost which is expected to by 25% by 2015 due to the aging population. The annual risk of fracture is greater than the combined risk of all cardiovascular disease and invasive breast cancer [34].

Osteoporosis-related or fragility fractures occur after low impact trauma, typically following a fall from standing height or less, but some occur spontaneously. Osteoporosis-related fractures are more likely to occur in the spine, hip, distal forearm or proximal humerus (major osteoporotic fractures); but other bones, such as pelvis, ribs and distal femur or tibia, are also susceptible to break.

Major osteoporotic fractures can be life-altering and/or life-threatening. The remaining life-time probability of a major osteoporotic fracture in postmenopausal women exceeds (approximately 12 %) that of breast cancer [35].

Major osteoporotic fractures are a major cause of morbidity in the population [35]. Hip fractures cause acute pain and loss of function. Recovery is slow and often incomplete, with many patients permanently institutionalized in nursing homes. Vertebral fractures may also cause acute pain and loss of function but may also occur without serious symptoms. In fact, approximately two-thirds of vertebral fractures are clinically silent, i.e. they do not cause enough pain to arouse suspicion of a fracture or request imaging [36]. However, vertebral fractures often recur, increasing the consequent disability with the number of fractures. Distal forearm or proximal humerus fracture cause acute pain and loss of function but the recovery is usually faster.

BMD is considered as the major determinant of bone strength and fracture risk [28], [37]–[39]. A standard deviation decrease in aBMD leads to a 1.5- to 3.0-fold increased risk of fracture depending on site-specific measurement and fracture site [38]. However, a low aBMD is not sufficient to explain all osteoporotic fractures [40]. In fact, low aBMD only explains 60 to 80 % of bone strength under laboratory conditions [39], and only 50 % of osteoporotic fractures are observed in postmenopausal women with a T-score below -2.5 [41].

Bone quality is also an important fracture risk [39], [42]. Bone quality refers to 3D structural characteristics of the skeleton, such as bone size, shape, mineral content distribution, trabecular bone architecture, damage accumulation, cortical bone thickness and geometry, turnover, osteon and osteocyte density and other factors such as structural proteins and crystal properties [42].

Clinical risk factors such as age, sex, body mass index (BMI), family history of fractures, glucocorticoid use, rheumatoid arthritis or smoking, alcohol and poor calcium intake also contribute to osteoporosis-related fracture risk independently of aBMD [28], [37].

Osteoporosis-related hip fractures are classified by the specific area of the break. Common types of hip fractures are: femoral neck fractures, which occur 2.5-5 cm from the hip joint; intertrochanteric fractures,

which occur between the neck of the femur and the lesser trochanter; and subtrochanteric fractures, which occur between the lesser trochanter and an area approximately 6 cm below.

Osteoporosis-related vertebral fractures are mainly located at the vertebral body, which is the area where the majority of compression load is borne [43]. Vertebral compression fractures are classified by type of deformity (wedge, biconcavity, or compression) and further by the degree of deformity (grades 0-3). A reduction in vertebral body height (anterior, posterior or middle) of 20- 25 % or more is considered a vertebral fracture [43]. The "semi-quantitative" method of grading deformities (the most popular one) distinguishes fractured vertebrae (grades 1, 2, and 3) from non-fractured vertebrae (deformities that do not reach the level of grade 1), **Figure 2.5**.

2.6. Diagnostic methods and tools

2.6.1. Dual Energy X-ray Absorptiometry

Dual Energy X-ray Absorptiometry (DXA) is the most widely used technique to evaluate BMD [44]. It is a painless technique which radiates a small amount of X-ray to a body area using two narrow-angle fan beams, one of high energy and the other of low energy. The different radiation energies and tissue absorption generate two images. Bone mineral content (BMC) is extracted from the combination of these images and divided by the measured body area to get the BMD.

DXA mainly benefits of the tissue absorption properties, being characterized by the high sensitivity that bone mineral has in front of the other body material compounds at these energies [45]. Thus, 2D-DXA images offer high contrast at bony structures, require short scanning times and low radiation dose. Other advantages of DXA include good precision, stable calibration, ease of use and ability to measure BMD at both hip and spine. For these reasons, DXA scans are widely used to diagnose osteoporosis, assist making decisions in treatment, and as a follow-up response to therapy.

However, this imaging modality also presents some limitations. BMD is computed from dividing the BMC (the amount of mineral at the specific scanned bone) by the measured area in the DXA. In consequence, the BMD is actually a projected areal density (in g/cm^2), rather than a true

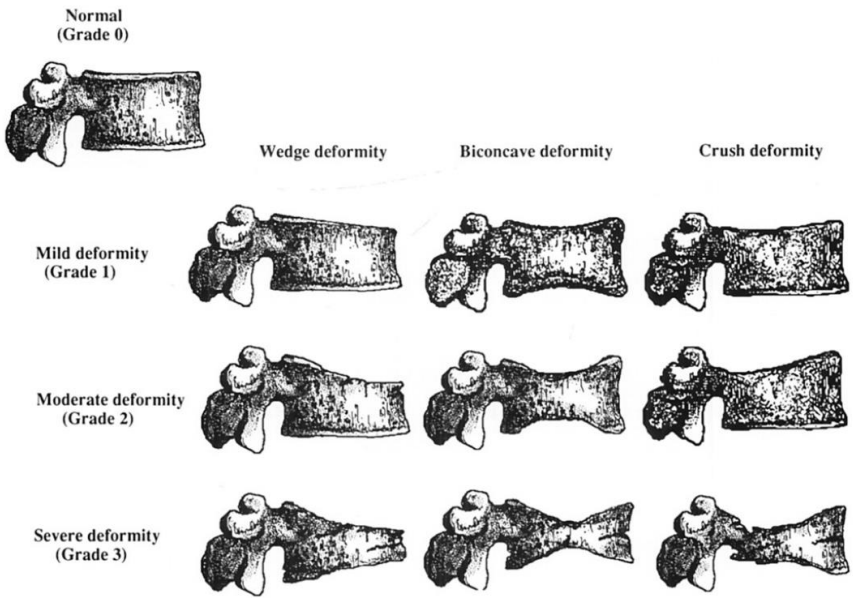

Figure 2.5: Classification of vertebral fractures by Genant [43].

volumetric density (in g/cm^3). This fact sometimes might turn to under- or over-estimation of the real value of BMD, when bones are smaller than usual or overlapping of bones occurs on the projection [21].

Besides, DXA does not provide information about the 3D shape, size or mineral content distribution of bones. Such information is of fundamental clinical importance, since it determines the mechanical response of the bone to external forces applied in real life, and hence the risk of fracture. Moreover, the trabecular and the cortical tissues are difficult to assess in separate ways through a DXA scan. Even so, this issue is also relevant for clinical experts, because both tissues have different metabolic processes and functions and should be treated through different medications.

Finally, DXA images can be affected by external artifacts (jewelry, coins), internal artifacts (tables, leads, surgical implants, enhancements), patient positioning, or other pathologies (osteoarthritis, fracture, aortic calcification, Paget's disease).

The ISCD [22] establishes the following indications of the study of the spine for osteoporosis diagnosis:

- Use AP DXA from vertebrae L1 to L4 (L1-L4 segment) for spine BMD measurement.
- Use all evaluable vertebrae and only exclude vertebrae that are affected by local structural change or artefacts. Use three vertebrae if four cannot be used and two if three cannot be used.
- aBMD based diagnostic classification should not be made using a single vertebra.
- If only one evaluable vertebra remains after excluding other vertebrae, diagnosis should be based on a different valid skeletal site.
- Anatomically abnormal vertebrae may be excluded from analysis if:
    - They are clearly abnormal and non-assessable within the resolution of the system; or
    - There is more than a 1.0 T-score difference between the vertebra in question and adjacent vertebrae
- When vertebrae are excluded, the aBMD of the remaining vertebrae is used to derive the T-score.
- The lateral spine should not be used for diagnosis but may have a role in monitoring.

Current DXA scan manufacturers include a software platform integrated with the hardware, in which the expert can evaluate the obtained image just after the acquisition, **Figure 2.6**. This software displays the aBMD at each single vertebra together with the total aBMD -the mean over the lumbar vertebrae-, computed over the segmented area (in red in **Figure 2.6**). It also locates the result over a reference curve established by the manufacturer, which relates the value of the total aBMD with the corresponding T-score and the age of the patient.

New DXA scans are capable to measure, besides aBMD, other bone parameters such as hip axis length and trabecular bone score, and other body tissues including fat mass, lean mass, and aortic calcification.

While only DXA can be used for diagnostic classification according to criteria established by the WHO, some other technologies may also be used for the management and follow-up of osteoporosis and fracture risk assessment. The main techniques are briefly introduced hereafter.

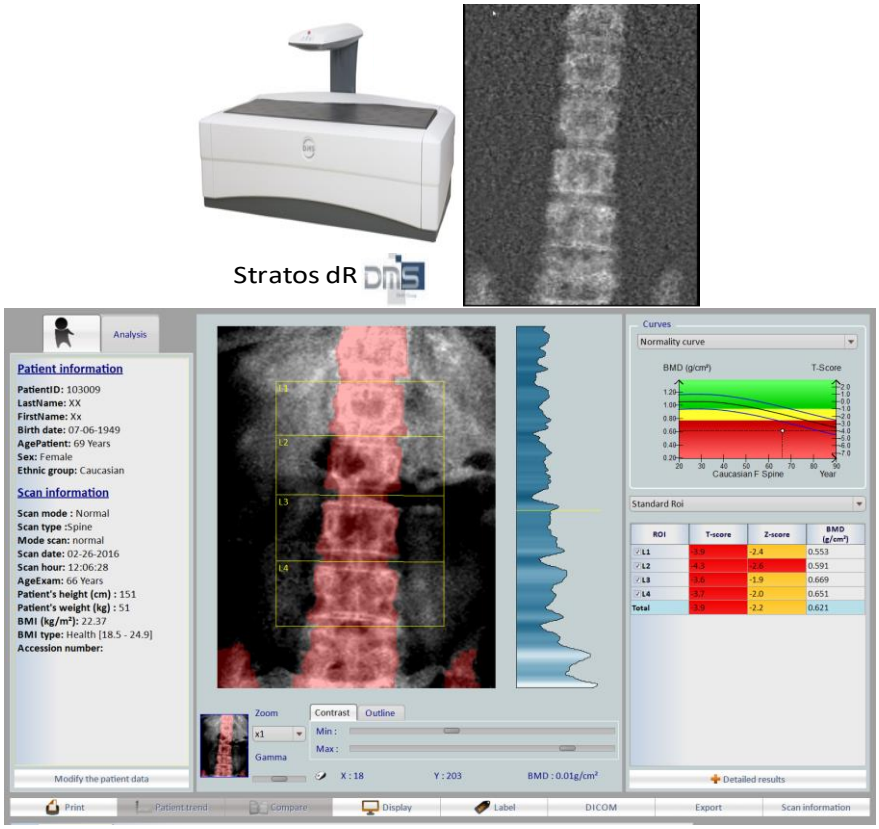

Figure 2.6: Commercial DXA equipment to diagnose osteoporosis.
Stratos dR platform (DMS, Montpellier, France) displaying: (left) the DXA-scan segmented with a red mask where the aBMD is computed; (middle) reference curve to locate the individual T-score; and (right) computation of the aBMD and T-scores for each single vertebra.

2.6.2. Quantitative Computed Tomography

Quantitative Computed Tomography (QCT) is the main alternative to DXA to evaluate BMD levels for osteoporosis assessment (**Figure 2.7**). QCT measures volumetric BMD (vBMD) expressed in units of grams of hydroxyapatite per cubic centimeter using a standard X-ray CT scanner with a calibration standard to convert Hounsfield Units of the CT image to BMD values. From this technology, a 3D analysis of the bony structure can be performed, vertebral body vBMD can be measured independently of the posterior part of the vertebra, and even trabecular or cortical structures can be evaluated separately.

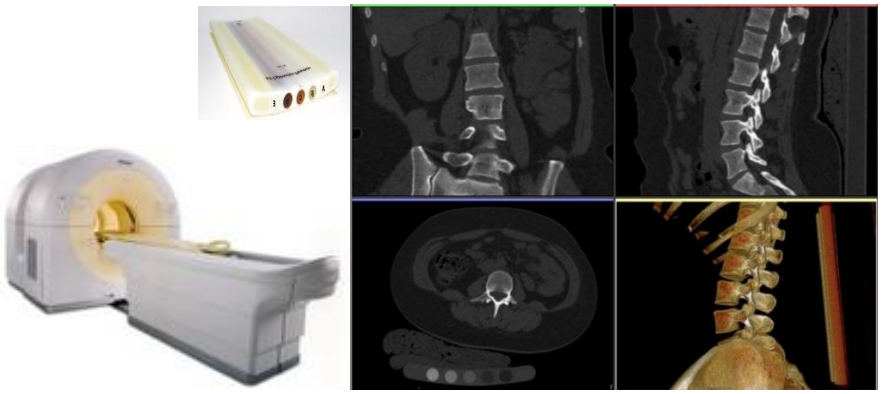

Figure 2.7: Volumetric QCT scan of the lumbar spine.
CT scan of Philips Gemini GXL PET/CT 16 (Philips Healthcare, Best, The Netherlands) and phantom of Mindways.

The main limitations are that QCT results in a higher dose of radiation (the CT radiation dose is between 1 and 3 mSv against 0.01 mSv used for DXA) and is more expensive than DXA (a CT scanner has a cost of between $175,000- $300,000 compared to a DXA scanner which costs from $30,000 – $90,000; and a DXA scan analysis costs between $85-$250, while a CT-scan analysis between $300-$1,500 [46]). In addition to the imaging device, the purchase of a QCT calibration phantom and a software to perform QCT measurements, such as the solution *QCT PRO*^{TM} proposed by Mindways (Austin, TX), is also necessary. Consequently, QCT is rarely used in clinical practice for osteoporosis management.

QCT measurements of the spine and hip are performed with clinical all-purpose, total body CT scanners equipped with special analysis software. QCT measurements of the forearm and tibia are performed with peripheral scanners specifically developed for the quantitative determination of BMD in these regions. According to previous ISCD Official Positions, QCT of the spine and peripheral QCT of the forearm can be used for fracture prediction and for treatment- or age-related monitoring of BMD, but not for the diagnosis of osteoporosis [47]. Peripheral QCT of the forearm can be used for fracture prediction. However, it is not appropriate for monitoring response to therapy at this time.

2.6.3. Complementary diagnostic tools

Besides the standard assessment presented above, other tools are also used by experts for osteoporosis screening or assessing fracture risk.

Quantitative ultrasound (QUS) is a peripheral technique which has been widely evaluated in the past years. QUS scans employ frequencies in the 200 to 1500 kHz range and measure broadband ultrasonic attenuation and the speed of sound in the bone (QUS scans do not measure BMD directly). The skeletal sites currently studied by QUS techniques are the calcaneus, distal metaphysis of the phalanx, the radius and the tibia. Most of the studies focused on the calcaneus because it is an easily accessible trabecular bone site. Several prospective studies have confirmed that QUS measurements in elderly women patients have predicted hip fracture and all nonvertebral fractures nearly as well as DXA at the femoral neck [42]. Moreover, QUS scanners do not use ionizing radiation and are smaller, more portable and less expensive than QCT and DXA scans. However, QUS measurements are affected by long term stability and issues related to cross-calibration, reference databases, precision, and technical diversity [48].

The most common method for measuring the risk of fracture is the *FRAX*® tool (WHO Fracture Risk Assessment Tool, University of Sheffield, UK). FRAX is a free tool, accessible via the web, and has country-specific reference databases. Clinical risk factors analyzed by the FRAX algorithm are: age, sex, BMI, prior osteoporotic fracture, family history of fractures, oral glucocorticoids use, rheumatoid arthritis, current smoking, alcohol intake, secondary osteoporosis and femoral neck aBMD (optional) [37]. There are many other risk factors for fracture that are not incorporated in assessment algorithms, such as: biochemical markers of bone turnover, risk factors for falls, total number of fractures, location of the fractures or previous exposure to pharmacologic intervention. Furthermore, FRAX has been proved to predict well hip fractures, but it is not as effective in predicting other kind of osteoporosis fractures, as vertebral fractures, because of differences in population characteristics, so further investigation has to be developed to find the best clinical predictors.

Another tool is *TBS iNsight*® of Medimaps (Geneva, Switzerland), which evaluates the quality of the vertebral bone in its micro-architecture using grey-level textural metrics. This tool provides an

index, the Trabecular Bones Score (TBS), which predicts fracture risk, independently of aBMD or FRAX, by studying vertebral bone texture in DXA scans [49], [50].

2.7. Clinical challenges

DXA is the most used technique to evaluate BMD, as it is a low radiation, painless and non-expensive technique. DXA provides 2D images in which the aBMD (g/cm^2) is measured. The ISCD recommends using the projected density along the AP direction to diagnose osteoporosis at the lumbar spine [22]. Vertebral fractures mainly take place in the vertebral body [43]. However, in AP DXA scans of the lumbar spine, the vertebral bodies superimpose with the posterior part of the vertebrae (pedicles, spinous processes and facets). Therefore, the vertebral body BMD cannot be estimated in AP DXA scans without including the posterior part of the vertebra, which is a limitation of DXA-based diagnosis of osteoporosis at the lumbar spine. Moreover, bone strength and fracture risk do not only depend on BMD but also on bone quality [42]. Trabecular bone architecture and cortical bone thickness are important elements that determine bone quality [51]. In osteoporotic bones, trabecular and cortical vBMD decrease (with different rates), as trabecular bone becomes more porous and cortical bone thickness decreases [47]. However, trabecular and cortical tissues are difficult to assess separately in a DXA scan.

An alternative technique to measure BMD is QCT. Using this technology, a 3D analysis of the bony structure can be performed, vertebral body vBMD can be measured independently of the posterior part of the vertebra, and even trabecular or cortical structures can be evaluated separately. However, QCT results in exposure to a higher dose of radiation and is more expensive, compared to DXA. Moreover, cortical thickness (especially at the vertebral body) has dimensions in the range of the spatial resolution of clinical QCT scans and thin cortices need advanced techniques to be measured accurately [52]. Consequently, QCT is rarely used in clinical practice for osteoporosis management [47].

To overcome the limitations of DXA and QCT, methods to obtain 3D subject-specific models of the bone from DXA scans are proposed and evaluated in within this thesis. The 3D model provides measurements at different vertebral regions (vertebral body or posterior vertebral

elements) and bone compartments (integral, trabecular or cortical bone). The accuracy is evaluated by comparing DXA-derived to QCT-derived 3D measurements for a validation set of women, men and subjects with normal bone healthy, low bone mass and osteoporosis. The ability of measurements from DXA-derived 3D models at lumbar spine to discriminate between osteoporosis-related fracture and control groups is also evaluated. Methodological challenges in relation to the objective of this thesis are described in the next chapter.

Chapter 3

3. METHODOLOGICAL BACKGROUND

This chapter reviews the methodological background of this thesis. First, statistical modeling methods that focus on capturing the statistical variability of anatomical structures within a population are briefly described. Then, methods to estimate a subject-specific 3D anatomical shape and appearance representation from 2D images are introduced.

3.1. Statistical models

3.1.1. Shape models

a) Modeling object shape: Statistical Shape Model

Statistical Shape Model (SSM) captures how the shape of an object of interest varies across a training set giving a compact representation of the allowable variation with enough specificity not to allow arbitrary variation different from that seen in the training set [5].

Shape representation

Different parameterizing techniques are used to encode a shape in some coordinate frame depending on its representation. The method employed to generate a statistical model strongly depends on the chosen shape representation.

Landmark-based representation is one of the most popular parameterization techniques used in anatomical models, thanks to its simplicity and ease to deal with anatomical structures [9], [53], [54]. In landmark-based representation, each object is described as a set of labeled points (also referred as landmarks) represented in a vector. Labeled points usually represent biological features, geometrical features, or even boundaries such as contours that surround an area or volume. Often, the coordinates of points are recorded along with their connectivity (how they are joined to form the boundaries). A set of labeled points with connectivity information is called a mesh. Labeled points are recorded through manual identification and/or semi-automated segmentation methods. The quality of the labeled points directly affects the statistical efficiency of the resulting shape model.

Medial models [55], [56], moment invariants [57], implicit representations [58], or parametric representations [59], [60] are some of shape representations also used in the analysis of anatomical structures. Due to the dominant role of landmark-based representations

as basis of SSM, next sections are focused on them. The use of landmarks as basis of SSM was introduced by Cootes *et al.* [5] as Point Distribution Model (PDM).

Shape correspondence

An essential requirement for building a PDM is that all shapes of the training set have the same topology (i.e. number and arrangement of points and connections) and their landmarks represent the same anatomic positions within the training set. If labeled points are recorded manually by experts, which locate a fixed number of landmarks in consistent positions throughout the different training samples, a shape correspondence method is not needed. However, landmark-based representations obtained by automatic or semi-automatic segmentation usually have different topologies. Therefore, once the landmarks are obtained in all shapes of the training set, spatial transformations are used to create correspondences between them. Establishing point set correspondences between all shapes of the training set is generally the most challenging part of SSM construction and at the same time one of the major factors influencing model quality [61]. Some methods to automatically compute shape correspondence are presented in this section.

Iterative Closest Point (ICP) [62] assumes that every point in shape $\boldsymbol{X}$ corresponds to the closest point in shape $\boldsymbol{Y}$. Rigid transformations are iteratively performed so that the sum of the squared distances between the corresponding points becomes minimal. This method works best if the initial poses of the shapes are close.

Robust Point Matching introduced by Gold *et al.* [63] uses deterministic annealing and soft assignment correspondence between point sets. A minimum description length approach is proposed by Davies *et al.* [64] and Cootes *et al.* [65] in which point correspondence is optimized along with model parameters. Syrkina *et al.* [66] proposed an optimization of the minimal description length function, based on an adaptive, hierarchical organization of surface patches to consider arbitrary surfaces.

Tsin and Kanade [67] introduced Kernel Correlation methods, which use multiple-linked registration algorithms and every point in shape $\boldsymbol{X}$ relates to every point in shape $\boldsymbol{Y}$, making it more robust to noise.

Gaussian Mixture Models (GMM) described by Jian and Vemuri [68], [69] are an extension of Kernel Correlation methods using sum of Gaussians as kernel density estimates. A GMM is a probabilistic model which states that all generated data points are derived from a mixture of a finite Gaussian distributions that has unknown parameters. The correspondence of the vertices is considered as a probability density estimation problem where the reference point set is represented by the centroids of the GMM and the rest of the point sets of the training database are generated from the GMM. The correspondence is obtained using the maximum of the GMM posterior probability for a given data point.

Coherent Point Drift (CPD), introduced by Myronenko and Song [70], [71] uses a probabilistic approach also based on GMM for rigid and non-rigid point set registrations. CPD takes the alignment of two-point sets as a probability density estimation problem. $\boldsymbol{Y} = (\boldsymbol{y}_1, \dots, \boldsymbol{y}_M)^T$ is the $M \times D$ matrix of the reference point set (source points) that should be registered onto $\boldsymbol{X} = (\boldsymbol{x}_1, \dots, \boldsymbol{x}_N)^T$, where $\boldsymbol{X}$ is the $N \times D$ matrix of the target point set. D is the dimension of the point sets. The points in $\boldsymbol{X}$ are the points generated by the GMM, and the points in $\boldsymbol{Y}$ represent the Gaussian Mixture Model centroids. The GMM probability density function is:

$$p(\boldsymbol{x}) = \sum_{m=1}^{M+1} P(m)p(\boldsymbol{x}|m) \tag{2}$$

where $p(\boldsymbol{x}|m) = \frac{1}{(2\pi\sigma^2)^{D/2}} exp^{\frac{-\|x-y_m\|^2}{2\sigma^2}}$. An additional uniform distribution $p(\boldsymbol{x}|M+1) = \frac{1}{N}$ is added to the mixture model to account for noise and outliers. Equal isotropic covariances σ^2 and equal membership probabilities $P(m) = \frac{1}{M}$ are used for all GMM components.

For rigid registration, the transformation is:

$$T(\boldsymbol{Y}, \boldsymbol{R}, t) = \boldsymbol{RY} + \boldsymbol{t} \tag{3}$$

where $\boldsymbol{t}$ is a 3-dimensional translation vector, $\boldsymbol{R}$ a 3×3 rotation matrix. The objective function to be minimized takes the form:

$$Q(\boldsymbol{R}, \boldsymbol{t}, \sigma^2) = \frac{1}{2\sigma^2} \sum_{m=1}^{M} \sum_{n=1}^{N} P^{old}(m|\boldsymbol{x}_n) \, \|\boldsymbol{x}_n - \boldsymbol{R}\boldsymbol{y}_m - t\|^2 + \frac{3N_P}{2} \log \sigma^2 \tag{4}$$

where P^{old} denotes the posterior probabilities of GMM components calculated using the previous parameter values, $N_P = \sum_{m=1}^{M} \sum_{n=1}^{N} P^{old}(m|\boldsymbol{x}_n)$.

For non-rigid registration, the transformation is defined as the initial position plus a displacement function v:

$$T(\boldsymbol{Y}, v) = \boldsymbol{Y} + v(\boldsymbol{Y}) \tag{5}$$

The objective function to be minimized takes the form:

$$Q(v, \sigma^2) = \frac{1}{2\sigma^2} \sum_{m=1}^{M} \sum_{n=1}^{N} P^{old}(m|\boldsymbol{x}_n) \left\|\boldsymbol{x}_n - \left(\boldsymbol{y}_m - v(\boldsymbol{y}_m)\right)\right\|^2 + \frac{3N_P}{2} \log \sigma^2 + \frac{\lambda}{2} \|P_v\|^2 \tag{6}$$

where P^{old} denotes the posterior probabilities of GMM components calculated using the previous parameter values, $N_P = \sum_{m=1}^{M} \sum_{n=1}^{N} P^{old}(m|x_n)$, P_v is a regularization term and λ a trade-off parameter. The variational calculus is used to minimize the objective function and derive the optimal displacement function v that transform the points in $\boldsymbol{Y}$.

Shape alignment

Once correspondences between the shapes of the training set are established, shapes are aligned in a common coordinate system to

remove the pose variability. The objective is to maximize the alignment of the spatial position of the point sets, through similarity transform (translation, rotation and scaling). If shape correspondence methods are applied, shapes are already aligned. However, the shape correspondence process could be biased by the choice of the reference shape. In this case, an iterative shape alignment process is needed to correct the bias.

Generalized Procrustes Analysis (GPA) [72] is the most common method used to this end. The algorithm minimizes the sum of distances of each shape to a reference shape. In this method a shape is arbitrarily chosen as reference shape, and all shapes are rotated, scaled and translated to align with it. A mean is estimated from the current set of aligned shapes, which then is rotate, scale and translate to align to the reference shape. Each shape is rotate, sale and translate again to match to the adjusted mean. Convergence is tested by examining the average difference between the transformations required to align each shape to the calculated mean and the identity transformation. If the distance is above a threshold, the reference is set to the calculated mean shape and the process is repeated until the mean shape does not significantly change.

Dimensionality reduction

Each i^{th} shape obtained after the shape alignment process is represented by an Dn element vector with $\boldsymbol{x}$ gathering the position of its n vertices in the D-dimensional space:

$$\boldsymbol{s}_i = (\boldsymbol{x}_1, \boldsymbol{x}_2, \ldots \boldsymbol{x}_n)^T \; with \; \boldsymbol{s}_i \in \mathbb{R}^{Dn} \; and \; i = 1, \ldots, k \tag{7}$$

where k is the number of images of the training set.

All shapes in the training dataset are assumed to follow a Gaussian distribution (i.e. they form an ellipsoidal cloud in this high-dimensional space). Therefore, it is possible to model shape variations as:

$$\boldsymbol{s} \sim \boldsymbol{\mathcal{N}}(\bar{\boldsymbol{s}}, \boldsymbol{\Sigma}) \tag{8}$$

where the mean $\bar{\boldsymbol{s}}$ and covariance $\boldsymbol{\Sigma}$ of the training k shapes are

calculated as:

$$\bar{\boldsymbol{s}} = \frac{1}{k}\sum_{i=1}^{k}\boldsymbol{s}_i \tag{9}$$

$$\Sigma = \frac{1}{k-1}\sum_{i=1}^{k}(\boldsymbol{s}_i - \bar{\boldsymbol{s}})(\boldsymbol{s}_i - \bar{\boldsymbol{s}})^T \tag{10}$$

Principal Component Analysis (PCA) [73] is applied to determine common variations of the shapes and build a compact model of shape variability (with less than Dn parameters) by computing the main axes of the cloud. The modes of variation (the ways in which the points of the shape tend to move together) are described by the eigenvectors $\boldsymbol{\rho}_j$ of the $(Dn \times Dn)$ covariance matrix $\boldsymbol{\Sigma}$ such that:

$$\Sigma\boldsymbol{\rho}_j = \lambda_j\boldsymbol{\rho}_j \; with \; j = 1, \ldots, Dn \tag{11}$$

$$\rho_j^T\boldsymbol{\rho}_j = 1 \tag{12}$$

where λ_j is the j[th] eigenvalue of Σ (with $\lambda_j \geq \lambda_{j+1}$) representing the variance of the data about the mean, in the direction of the corresponding eigenvectors $\boldsymbol{\rho}_j$. Therefore, a SSM is defined as the mean position of the vertices and the main modes of variation describing the linear displacements of the vertices from their mean position [6]. A new instance of the shape can be modeled as:

$$\boldsymbol{s} = \bar{\boldsymbol{s}} + \boldsymbol{P}\boldsymbol{a} \tag{13}$$

where $\boldsymbol{P} = (\boldsymbol{\rho}_1\boldsymbol{\rho}_2 \ldots \boldsymbol{\rho}_p)$ is the matrix of the first p principal components and $\boldsymbol{a}$ is a vector of scalar coefficients weighting the contribution of each principal component. Therefore, each principal

component changes the shape by moving the landmarks $\boldsymbol{x}$ along straight lines defined by the eigenvectors $\boldsymbol{\rho}_j$, passing through their mean position defined by $\bar{\boldsymbol{s}}$. An instance of an SSM of the lumbar spine is showed in **Figure 3.1.**

Since the model parameters are uncorrelated, the variance of $\bar{\boldsymbol{s}}$ is equal to the sum of the individual component variances:

$$V_{Total} = \frac{1}{k}\sum_{j=1}^{Dn}\lambda_j \tag{14}$$

The number of p eigenvalues to use are typically selected according to the proportion of the total variance to be explained.

The space domain of the shapes (subspace of allowed shapes) is derived by examining the distribution of the parameter values required to generate the shapes of the training set. Since the variance of a_j over the training set can be shown to be λ_j, the space domain is approximated by a hyper-rectangle around the mean shape:

$$|a_j| < 3\sqrt{\lambda_j} \tag{15}$$

Alternative approximations for the subspace of allowed shapes are proposed by several authors. Stegmann *et al.* [74] proposed an alternative approximation using a hyper-elliptical space. Cerrolaza *et al.* [75] presented an efficient hyper-elliptical approximation based on the Newton-Raphson optimization method. Cootes and Taylor [76] proposed a mixture of Gaussians that approximates the probability density function of the shape. Ruiz *et al.* [77] proposed a weighted regularized projection where the contribution of each point of the SSM is weighted based on prior constraints.

PCA is the most used technique to reduce dimensionality in SSM, but other methods can be found in the literature such as: Principal Factor Analysis [78] [79], Independent Component Analysis [80], Kernel Principal Component Analysis [81], Isomap [82], Local Lineal Embedding [83], or Laplacian Eigen map [84].

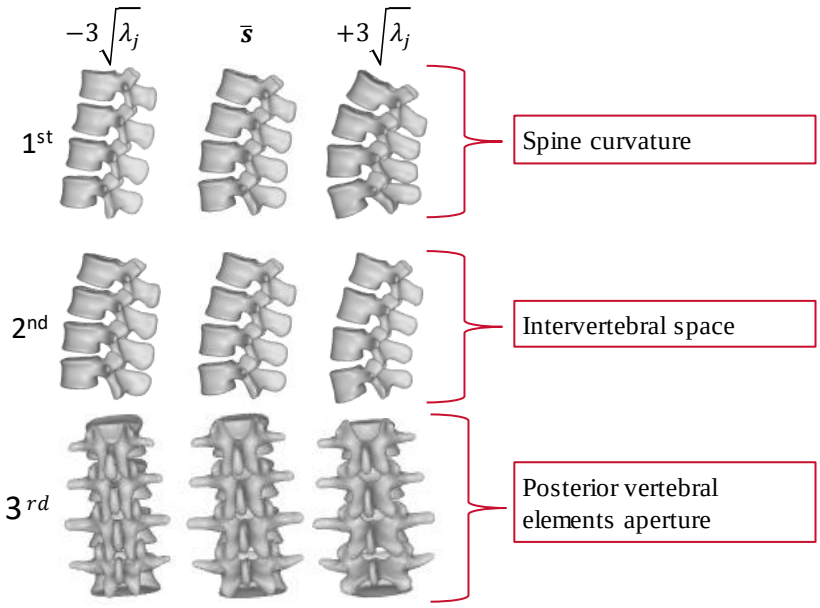

Figure 3.1: Statistical shape model of the lumbar spine.
1st to 3rd principal components. The first variation mode shows variations of the spine curvature (lordosis), the second shows variations of the intervertebral space and the third shows variations of the transversal process aperture.

b) Searching object shape: Active Shape Model

Active Shape Model (ASM) uses an instance of the SSM as template to characterize and interpret similar structures in new data [6], [9]. An SSM instance is generated by deforming the mean shape $\bar{\boldsymbol{s}}$ using (13) and by subsequently applying a similarity transform $\boldsymbol{T}$:

$$\boldsymbol{T}(s) = \alpha \boldsymbol{R}\boldsymbol{s} + \boldsymbol{t} \tag{16}$$

where α is the scaling, $\boldsymbol{R}$ the rotation matrix and $\mathbf{t}$ the translation vector. ASM searches the set of parameters which best match the SSM instance to the new image. This set of parameters defines the shape and position of the target object in the new image.

The first step of the ASM algorithm is to initialize the position of the SSM instance in the new image. Then, an iterative approach is performed to improve the fit of the model instance in the new image and find the best set of parameters. In this iterative approach, a region

of the image around each point $\boldsymbol{x}_i$ of the SSM instance is examined to find the best nearby match for the point $\boldsymbol{x'}_i$. Shape and pose parameters are updated to fit the new points $\boldsymbol{s'}_i$. Constrains are applied to the shape parameters to ensure plausible shapes using (15). Th new SSM instance is compared with the target image using a fit function and a local optimization technique, such as Powell's method or Simplex, is used to find the local minimum. The process is repeated until convergence.

If the SSM represents boundaries and strong edges of the object (**Figure 3.2**a), the distance between a given model point and the nearest strong edge in the image could be used as fit function:

$$F(\boldsymbol{a}, \alpha, \boldsymbol{R}, \boldsymbol{t}) = |\boldsymbol{s'} - \boldsymbol{s}|^2 \quad (17)$$

In this case, the region of the image around each shape model landmark is examined to determine a displacement of the landmark to a better position. Local deformations are transformed into adjustments to the pose and shape parameters of the SSM instance.

An alternative approach is to sample the image around the current model point and compare with the intensity profile of the model learned from the training set (**Figure 3.2**b). The new landmark's position of the SSM instance is computed by minimizing the distance between the measured intensity profile and profile computed from the training set. In this case, the Mahalanobis distance of the sample from the model mean is commonly used as fit function.

3.1.2. Appearance models

a) Modeling appearance: Statistical Appearance Model

Statistical appearance model (SAM) captures how the shape of an object of interest and the image texture within (or surrounding) that shape vary across a training set [7], [8], [10], [12]. The combination of shape and textural information is referred to as the appearance of an object.

Appearance representation

The image texture from statistical appearance models can be refer to simple grey level pixel values or other descriptors such as image

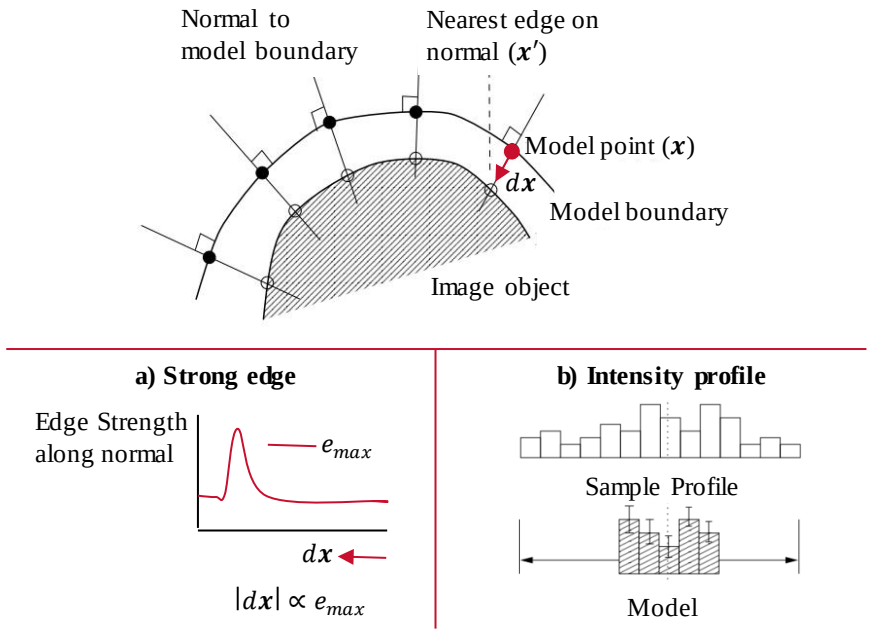

Figure 3.2: Active Shape Models.
a) Searching strong edges in the normal direction to the model boundary; b) Searching in the intensity profile normal to the model boundary. Adapted from Cootes *et al.* [9] and [12].

gradients. Moreover, the image intensity could be represented by the intensity in the object, the intensity profiles along the perpendicular direction of a surface mesh at each of the points, or the intensity in patches around the points of the mesh.

Normalization

The first step to build a SAM is to remove the shape variability of the training images generating a shape-normalized version of the object of interest. Therefore, each image of the training set is warped using a triangulation algorithm so that its control points match the mean shape of the SSM to assure that the statistical texture model captures only variations related to grey-level information.

Then, grey level information is sampled from the shape-normalized image over the region covered by the mean shape. Intensity values are normalized to eliminate the effects of machine settings and global illumination properties.

Each texture image obtained after the normalization process is represented by an m element vector gathering the grey-level values contained in the m points inside the object of interest.

$$\mathbf{g}_\mathrm{i} = (g_1, g_2, \ldots, g_m)^T, \boldsymbol{d}_i \in \mathbb{R}^m \tag{18}$$

Dimensionality reduction

PCA is computed over the training set of aligned texture vectors to describe the intensity patterns as described in Section 3.1.1.a). New texture patterns are defined as:

$$\boldsymbol{g} = \overline{\boldsymbol{g}} + \boldsymbol{Q}\boldsymbol{b} \tag{19}$$

where $\overline{\boldsymbol{g}}$ is the mean normalized grey-level vector, $\boldsymbol{Q} = (\boldsymbol{\rho}_1\boldsymbol{\rho}_2 \ldots \boldsymbol{\rho}_q)$ is the matrix of the first q principal components and $\boldsymbol{b}$ is a vector of scalar coefficients weighting the contribution of each principal component.

Once the texture model is obtained, it is combined with the shape model as follows:

$$\mathbf{c} = \begin{pmatrix} \mathbf{W_s a} \\ \boldsymbol{b} \end{pmatrix} = \begin{pmatrix} \boldsymbol{W_s P^T}(\boldsymbol{s} - \overline{\boldsymbol{s}}) \\ \boldsymbol{Q^T}(\boldsymbol{g} - \overline{\boldsymbol{g}}) \end{pmatrix} \tag{20}$$

As the shape model parameters $\boldsymbol{a}$ and the texture model parameters $\boldsymbol{b}$ work with different units (i.e. distance and intensity units respectively), weights $\mathbf{W}_s$ are imposed to commensurate these parameters:

$$\boldsymbol{W}_s = \beta \boldsymbol{I} \tag{21}$$

where $\boldsymbol{I}$ is a unit matrix a β is the ratio of total texture variation to the total shape variation.

Finally, a global PCA is applied to $\boldsymbol{c}$ to obtain a SAM:

$$\boldsymbol{c} = \boldsymbol{O}\boldsymbol{d} \tag{22}$$

where $\boldsymbol{O}$ is the matrix of principal components and $\boldsymbol{d}$ is a vector of appearance parameters controlling both the shape and grey-levels of the models. The shape and grey-levels could be expressed directly as:

$$\boldsymbol{s} = \bar{\boldsymbol{s}} + \boldsymbol{P}\boldsymbol{W}_{\boldsymbol{s}}\boldsymbol{O}_{\boldsymbol{s}}\boldsymbol{d} \tag{23}$$

$$\boldsymbol{g} = \bar{\boldsymbol{g}} + \boldsymbol{Q}\boldsymbol{O}_{\boldsymbol{g}}\boldsymbol{b} \tag{24}$$

$$\boldsymbol{O} = \begin{pmatrix} \boldsymbol{O}_s \\ \boldsymbol{O}_g \end{pmatrix} \tag{25}$$

b) Searching appearance: Active Appearance Model

Active Appearance Model (AAM) can be considered as an extension of ASM, since AAM uses models with texture besides shape information as template to characterize and interpret similar structures in new data.

Given a SAM instance and a reasonable starting approximation, AAM searches the set of parameters which best match the SAM instance to the new image by iteratively minimizing the difference ($\boldsymbol{\delta I}$) between a new image ($\boldsymbol{I_i}$) and one synthesized by the model ($\boldsymbol{I_{Model}}$). An instance of the AAM can be generated applying (23) and (24), inverting the grey-level normalization, applying the appropriate pose to the points and projecting the grey-level vector into the image.

In AAM, three types of parameters are optimized to search for the target object in the image: pose parameters (scaling, rotation and translation), appearance parameters (shape and texture) of the combined model, and texture normalization parameters. As several parameters need to be adjusted, Cootes *et al.* [10], [11] observe that displacing each model parameter induces a particular pattern in the residuals. This pattern can be learned and provide a-priori knowledge of how to adjust the model parameters during image search. Therefore, instead of attempt to solve a general optimization each time, the AAM learns a linear model of the correlation between parameter displacements and the induced residuals, in a training phase; and it

measures the residuals and uses this model to correct the current parameters, during search.

3.1.3. Individual and global models

Statistical models must meet two requirements in order to accurately identify target objects in new data: generality and specificity. Models must be generic and extract as much variability as possible from the training set. Hence, the training set must be chosen carefully to collect the global and local variability of the population. Models also must be specific, and only allow for plausible characteristics of the population. Complex structures (i.e. with large variability or composed by several objects) could be also modelled with statistical models. However, more sophisticate methods are needed in order meet generality and specificity requirements. In this section, two traditional approaches to model complex structures are introduced: individual and global models.

A simple approach to deal with complex structures is to model each organ individually [85], [86]. Dividing structures and modeling them as several individual statistical models increases generality and reduce the dimensionality of each statistical model, while limiting their capacity to represent high-level anatomical patterns. Individual models do not allow to enforce inter-object constrains. Therefore, they often require the pre-alignment of the training set, projecting the complex structure to a common normalized shape space to guarantee the anatomical coherence [85], [87].

Another approach to model complex structures is to use a single statistical model. Integrating complex structures into a global model increases specificity, as global shape and spatial interrelations between organs are embedded intrinsically in the statistical model. Other advantages of global models are the computational simplicity of the approach, and the ability to overcome the weak image features that may be present in parts of multi-organ complexes. The use of a global model can thus help to impose strong anatomical constraints that may facilitate the definition of those parts suffering from missing data, occlusion, or image artifacts. On the other hand, global models capture global variability but underestimate the local variations, are often inflexible and can be severely affected by the high-dimension-low-sample-size (HDLSS) problem (i.e. the dimensionality of the problem is significantly higher than the number of training images available), of particular

relevance in a multi-organ context [88]. This approach has been extensively exploited by early [89]–[93], and more recent works [94]–[96], and has been effectively applied to different anatomical contexts and image modalities.

3.2. 3D subject-specific shape and intensity modelling from 2D images

3D subject-specific models of anatomical structures are useful tools to improve the visualization, interaction and interpretation of the volumetric data from 3D imaging modalities. However, 3D imaging technologies are more expensive, have longer acquisition times, result in exposure to a higher radiation dose (in case of computed tomography, CT) and are not always available. In order to overcome those limitations, researchers have investigated ways to obtain 3D subject-specific models of anatomical structures from 2D imaging modalities [97], [98]. One solution is to use statistical models that capture the anatomical variability of the object of interest and a 3D-2D model-to-image registration methods. This approach makes use of a prior statistical 3D model of what it is expected in the image to find the best match of the 3D model to a new 2D image.

First, 3D models and 2D images have to be brought into the same coordinate system. Dimensional correspondence can be achieved either by bringing the 3D data into 2D coordinate system, or by bringing the 2D data into 3D coordinate system. In projection strategy, 3D data are projected onto the 2D data plane. In back-projection strategy, each 2D data is back-projected into the 3D space by connecting 2D points with the X-ray source.

Moreover, 3D-2D model-to-image registration methods could be divided based on the nature of the registration. Feature-based registration methods search the correspondence between model features and image data. Intensity-based registration methods search the correspondence between intensity from voxels of the model and intensity from the pixels of the image. Feature and intensity-based methods for 3D subject-specific shape and density modeling of bones from 2D images and statistical models are commonly used in the literature. The main methods are briefly described in the next sections.

3.2.1. Feature-based methods

Feature-based registration methods use geometrical entities (points, edges, contours, or surfaces) to minimize the distance between 3D features extracted from 3D data (images or models) and the corresponding 2D features obtained from 2D images. Feature-based methods can be further classified as point-to-point, curve-to-curve and surface-to-curve registrations.

Point-to-point registration methods are normally based on anatomical landmarks which are manually identified. The proper extraction of landmarks depends on user ability. 3D-2D point-to-point registration methods are usually used as initialization step before applying more complex methods [99]–[101].

Boisvert *et al.* [102] estimate 3D subject-specific spines from posterior-anterior and a lateral radiograph using an articulated statistical shape model and a point-to-point 3D-2D registration method. In this registration method, the 3D anatomical landmarks are projected to the 2D plane. Then, the articulated shape model parameters that minimize the Mahalanobis distance and the quadratic error between the projected anatomical landmarks and respective landmarks on the radiographs are searched. The error is minimized for all the radiographs at a time. Intervertebral rigid transformations used to build the articulated model are also used to project the landmarks. Moura *et al.* [103] modified the method proposed by Boisvert *et al.* by adding a spline passing through the vertebra bodies, achieving a faster and higher accuracy.

Fleute *et al.* [13] used a 3D SSM and a curve-to-curve 3D-2D registration method to recover the shape of the femur from four 2D X-ray images acquired with a C-arm. A generalization of the Iterative Closest Point (ICP) algorithm [62] to nonrigid registration is used to fitting the 3D model to the 2D images. First, a global search based on ICP is used to estimate rigid transformations. Then, registration is refined using local search based on simulated annealing technique and the downhill simplex algorithm.

Benameur *et al.* [99] proposed a curve-to-curve 3D-2D registration method for scoliotic spine from two radiographs. 3D data are used to generate an SSM for each vertebra. Vertebrae contours in the radiographs are extracted using a Canny detector. Then, registration is

initialized with an estimation of the scale and pose parameters using anatomical landmarks and least square method. The squared distances between the anatomical landmarks of the mean shape and the associated points estimated from the stereo-corresponding landmarks is minimized. The second step of the 3D/2D registration is the minimization of a cost function composed by a likelihood energy term and a prior energy term. The first term is measured as the similarity between the external contour of the lateral and the posteroanterior perspective projections of the model and an edge potential field estimated on the two radiographic views. The second term is based on the Mahalanobis distance of the SSM. It is important to note that they worked with each vertebra individually, i.e. no multi-object statistical model was used. Besides, they did not use explicit 3D/2D feature correspondence. The initialization of the model instance over the image is a crucial step in the accuracy of this registration method.

Baka *et al.* [15] estimated the 3D subject-specific shape of the femur from calibrated X-ray images. They relied on the method developed to Benameur *et al.* [99]. Instead of minimizing the distance between the 2D contours, Baka *et al.* [15] minimized the 3D distance of the silhouette landmarks.

Zhen *et al.* [14] proposed a 3D-2D registration method to obtain a subject-specific femur surface from calibrated X-ray images; but using a more sophisticated 2D-3D correspondence method than ICP. The 3D-2D registration method start generating an SSM with the 3D data. Then, apparent contours of the SSM surface are projected onto 2D image planes in which edges of the shape are extracted. The projected apparent contours and the edges are associated using an iterative non-rigid 2D matching process. The proposed correspondence method uses a symmetric injective nearest-neighbor mapping operator and a thin-plate spline deformation. Once correspondence is established, matched points are back-projected into 3D and a 3D-3D registration is done. Surface registration is solved in three stages: affine registration, statistical extrapolation and regularized shape deformation. Besides the image-to-model correspondence method, the regularized shape deformation is an advantage of this method. Due to regularized shape deformation allows to estimate pathology shapes even when the SSM is constructed from only normal anatomy shapes.

3.2.2. Intensity-based methods

Intensity-based methods use all the information containing in the images to be registered and optimize similarity between them.

A popular approach of the intensity-based 3D-2D registration methods is to project the 3D data (CT image or model) onto the 2D plane(s) using ray-casting. Rays start off a source point and pass through the 3D data up to the 2D plane generating a simulated X-ray projection image called Digitally Reconstructed Radiographs (DRRs). The value associated to each position of the DRR image is the sum of the 3D data lying on the connecting ray. After generating the DRR image, registration method optimizes the similarity measure between the generated DRRs and the X- ray image(s).

The grey-level values of the model instance $\boldsymbol{I}_{Model}$ are projected to generate the simulated 2D image $\boldsymbol{I}_{Sim}$:

$$\boldsymbol{I}_{Proj}(x,y) = \sum_{z} \boldsymbol{I}_{Model}(x,y,z) \tag{26}$$

The **w** model instance parameters are optimized to maximize the similarity between the projection of the model instance $\boldsymbol{I}_{2D\_Proj}$ and the 2D image $\boldsymbol{I}_{2d\_Img}$. The similarity between $\boldsymbol{I}_{2D\_Proj}$ and $\boldsymbol{I}_{2D\_Img}$ is measured in the 2D binary mask region of interest as:

$$sim_{tot}(\boldsymbol{w}) = \sum_{k} sim(\boldsymbol{I}_{2D\_Proj} - \boldsymbol{I}_{2D\_Img}(v))^2 \tag{27}$$

Similarity could be measured using mutual information, cross correlation, sum of square differences, entropy of difference image, pattern intensity, gradient correlation, gradient difference, variance weighted sum of local normalized correlation, normalized mutual information, chi-square, and correlation ratio [98].

Lamecker *et al.* [104] proposed a 3D-2D intensity-based registration method for the pelvis. A multi-level approach is used to align and map the training images used to generate an SSM. From this SSM, a thickness

image which is the propagation length of simulated rays through the volume enclosed by the shape model. In order to compare the projected 3D data with the 2D data, volume rendering technique is applied to generate synthetic x-ray images from the same CT data used to build the model. Then, a gradient-descent method is used to minimize the distance between the silhouettes of the shapes in the thickness image and the simulated X-ray image. Although they used multi-level methods to align the training images, they generated a single SSM. They evaluated their method with one and two simulated X-ray images.

Tang and Ellis [105] generated a hybrid statistical atlas based on in-spheres to estimate the shape of femur in 3D from X-ray images. They optimized a similarity measure (non-gradient-based optimization technique) between the DRRs of the shape model and the 2D interventional images. As their statistical atlas only provides the shape, the surface of the shape is increased inward to simulate image volume and the thickness of the cortical bone.

Ahmad *et al.* [17] proposed a method to estimate not only the shape but also the BMD distribution of the femur from four 2D-DXA images. First, they generated a statistical atlas by fitting a deformable template (tetrahedral model) with shape and density information onto each CT of the training set. Then, deformation fields between each subject's tetrahedral model and an average of them is computed. Finally, PCA is applied to the deformation fields. The generated statistical model is used to estimate the 3D subject-specific shape and density of the femur from four 2D-DXA images. The parameters of the generated statistical model are varied to minimize the difference between the simulated DXA images from projections of the model and the four acquired DXA images. In the iterative 3D-2D registration method the summed mutual information of the four images is minimized.

Humbert *et al.* [106] also proposed a method to estimate the shape and the BMD distribution of the proximal femur from a single 2D-DXA image. First, they used a semi-automatic method to segment the proximal femur in the QCT images of the training set. Then, point-set registrations methods are used to align the shapes, and PCA is applied to generate the 3D statistical shape and density model. Finally, pose, scale and statistical shape and density model parameters are iteratively modified to optimize the similarity between projection of the 3D statistical model and the DXA image. Powell's multi-dimensional

optimization method is used as 3D-2D registration method to search for the parameters. The first registration is done using the mean shape and density and only pose and scale are optimized.

Whitmarsh *et al.* [21], applied the method that they developed for the femur [18] to subject-specific modeling of the lumbar spine (from L2 to L4) using two 2D-DXA images (AP and Lateral views). For each vertebra, a statistical shape and density model (based on the work of Cootes *et al.* [10]) is generated. The three models are simultaneously registered onto the AP and lateral DXA scans to generate a 3D model of the lumbar spine. The 3D-2D registration method is divided in three steps. First, mean vertebral shapes are aligned with both DXA views by coarse manual alignment. Second, rigid transformations and a simplified model composed by the first variation mode of the SSM (which describes the size of the vertebra) and the first variation mode of the SAM (which describes the global density) are optimized using the mean squared error as a similarity measure. Finally, fine registration is done using a more complex model composed by 13 shape modes and 5 density modes.

Featured-based methods produce faster registrations than intensity-based methods as they use only a part on the information included in the data [107]. However, featured-based methods depend on the accurate feature extraction and correspondence. Intensity-based methods usually need a longer computation time, but generate more accurate registration by relying on intensity information included in the data [107].

3.3. Methodological challenges

3D subject-specific models of the bone are useful for a number of clinical applications such as surgery planning, postoperative evaluation as well as implant and prosthesis design [97]. In the literature, methods using statistical models and registration algorithms were proposed to estimate the 3D shape and density of bones from a limited number of DXA scans.

SSMs, generated from CT images, are used to recover the 3D shape of the proximal femur from a few radiographs [13]–[15]. Other methods are proposed to estimate, in addition to bone shape, the BMD distribution, [16]–[18]. However, in the above-described methods, no

specific algorithm is proposed to quantify the cortical and the trabecular bone. Väänänen *et al.* [19] rely on a 3D-2D modeling method, and estimate the cortical thickness using thresholding and morphological operations. Thresholding techniques, however, have been shown to be less accurate when estimating thin cortices [108]. Humbert *et al.* [20] propose a method to assess the cortex and trabecular macrostructure of the proximal femur in 3D from an AP DXA scan. A model-based approach is used to estimate the cortical thickness and density [109], providing accurate measurements even for thin cortices.

Applying such methodologies to obtain 3D subject-specific shape and density estimation of the lumbar spine from DXA scans is not straightforward: DXA spine images are much noisier than hip DXA scans because rays have more biological tissue to penetrate; geometry of the spine is more complex than the one of the femur; and the presence of more than one anatomical structure (i.e. 4 lumbar vertebrae) requires modeling inter-object relationships besides shape and density. Moreover, the cortex of the vertebral body is very thin (from 180 to 600 μm with a mean thickness of 380 μm [110], [111]), which makes the segmentation of the cortical and trabecular bone very challenging. Whitmarsh *et al.* [21] obtain 3D subject-specific estimates of the lumbar spine (from L2 to L4) using two DXA images (AP and lateral views). Although measurements are performed in the trabecular compartment, no specific algorithm is proposed to quantify the cortical bone. Furthermore, lateral spine imaging with densitometric Vertebral Fracture Assessment (VFA) is used in clinical practices to evaluate the presence of vertebral fractures. However, VFA (which uses single-energy X-rays) does not measure BMD. Due to high precision errors, lateral DXA (i.e. double-energy) scans should not be used for osteoporosis screening [22].

To the best of our knowledge, no 3D modeling methods of the shape and density of the lumbar spine, including cortical and trabecular bone assessment, using a single AP DXA scan, has been reported in the literature.

Chapter 4

4. 3D SUBJECT-SPECIFIC SHAPE AND DENSITY ESTIMATION OF THE LUMBAR SPINE FROM A SINGLE ANTEROPOSTERIOR DXA IMAGE INCLUDING ASSESSMENT OF CORTICAL AND TRABECULAR BONE

The content of this chapter is adapted from the following publication:

M. López Picazo, A. Magallón Baro, L. M. del Río Barquero, S. Di Gregorio, Y. Martelli, J. Romera, M. Steghöfer, M. A. González Ballester, and L. Humbert."3D Subject-Specific Shape and Density Estimation of the Lumbar Spine from a Single Anteroposterior DXA Image Including Assessment of Cortical and Trabecular Bone", IEEE Transactions on Medical Imaging, vol. 37, no. 12, pg. 2651-2662, 2018

This chapter propose the development and validation of a method to provide a 3D subject-specific shape and density estimation of the lumbar spine from a single AP DXA image including assessment of cortical and trabecular bone.

4.1. Introduction

DXA is the standard exam for osteoporosis diagnosis and fracture risk evaluation at the spine. However, numerous patients with bone fragility are not diagnosed as such. In fact, standard analysis of DXA images does not differentiate between trabecular and cortical bone; neither specifically assess of the bone density in the vertebral body, which is where most of the osteoporotic fractures occur. QCT is an alternative technique that overcomes limitations of DXA-based diagnosis. However, due to the high cost and radiation dose, QCT is not used for osteoporosis management.

To overcome the limitations of DXA and QCT, methods using statistical models and registration algorithms are proposed to estimate the 3D shape and density of the femur from a limited number of DXA scans [13]–[20]. A method to estimate the 3D subject-specific shape and density of the lumbar spine (from L2 to L4) using two DXA images (AP and lateral views) is also proposed in [21]. However, no 3D modeling methods of the shape and density of the lumbar spine, or its cortical and trabecular bone assessment, using a single AP DXA scan, has been reported in the literature.

In this chapter, we propose a method to estimate the shape and vBMD at the lumbar spine (from vertebra L1 to L4) using a single AP DXA image. The method is based on a 3D statistical shape and density model built from a training set of 90 QCT scans. The model describes the principal statistical variations in shape and density observed in the training database. A 3D shape and density estimation of the lumbar spine is obtained by registering and fitting the statistical model onto the AP DXA image. Then, a model-based algorithm is used to segment the cortical layer and propose a separate assessment of the trabecular and cortical bone at the vertebral body. Clinical measurements are performed at different vertebral regions and bone compartments. Finally, the accuracy of the method is evaluated by comparing DXA-derived with QCT-derived 3D subject-specific models and clinical measurements for a validation set of 180 subjects.

4.2. Materials and Methods

4.2.1. Study subjects and medical images

Two different databases collected by the *CETIR Centre Mèdic* (Barcelona, Spain) were used in this study: a training database (90 subjects) to generate the statistical shape and density model (Section 4.2.2), and a validation database (180 subjects) to evaluate the accuracy of the DXA-derived 3D measurements (Section 4.2.5).

Subjects included in both databases were adult men and women. Exclusion criteria included skeletal disease other than osteoporosis, such as severe osteoarthritis, severe scoliosis or abnormal bone growth and vertebral fracture. An additional criterion to recruit the subjects included in the validation database was to obtain the same number of subjects in each category used to define bone density: 30 subjects with osteoporosis, 30 with osteopenia and 30 with normal bone density; with a 2/3 female and 1/3 male ratio.

All subjects included in the training and validation database presented clinical indications for an AP DXA scan at the lumbar spine. When DXA scan confirmed that inclusion/exclusion criteria were met, the subjects were invited to participate to the study and abdominal QCT scans were performed. AP DXA and QCT scans were therefore performed for all participants. Both scans were analyzed and interpreted by radiologists. AP DXA scans of the training set were used to ensure inclusion/exclusion criteria were met; whereas AP DXA scans of the validation set were also used to generate the 3D subject-specific estimations. QCT scans of the training set were used to generate the statistical shape and density model; whereas QCT scans of the validation set were used as ground truth to evaluate the accuracy of the estimated DXA-derived 3D measurements. Volunteers were informed about the purpose of the study, the potential risks of undergoing explorations in which they would be subjected to ionizing radiations and the subsequent use of their anonymized scans. Volunteers were recruited until achieving the desired number of subjects in each group. The study was approved by the Committee of Clinical Investigation of "*Fundació d'unió Catalana d'hospitals*" and written informed consent was obtained from all subjects. Subjects included in the training and validation sets were collected prospectively within the European EuroStars Project (ID: 9 140).

The AP DXA scans were performed at CETIR Centre Mèdic using a Lunar iDXA scanner (GE Healthcare, Madison, WI) or a Stratos dR DXA scanner (DMS, Mauguio, France). aBMD at vertebrae L1 to L4 (L1-L4 segment) was measured in the DXA images and T-score was computed using the enCORE software (GE Healthcare) or Stratos software (DMS), respectively. Participants were categorized using the T-score of the L1-L4 segment, following the ISCD recommendations [8], as: normal bone mass or healthy (T-score $\geq$ -1), low bone mass or osteopenia (-2.5 < T-score < -1) or osteoporosis (T-score $\leq$ -2.5). Vertebrae affected by local structural changes or artefacts were excluded to derive the T-score. However, this criterion was not used as exclusion criteria for the subject, neither to discard vertebrae for the statistical model generation nor for the 3D estimation.

The QCT scans were performed at the lumbar spine, in a region of interest including at least vertebrae L1 to L4. The study subjects were scanned at CETIR Esplugues PET (*Esplugues de Llobregat*, Spain) using a Philips Gemini GXL 16 (Philips Healthcare, Best, The Netherlands) or a GE HiSpeed QX/I scanner (GE Healthcare), and at CETIR *Clinica del Pilar* (Barcelona, Spain) using a GE Discovery CT750 HD scanner (GE Healthcare). The QCT voxel size ranged from 0.64 mm × 0.64 mm × 0.5 mm to 1.10 mm × 1.10 mm × 0.5 mm (average pixel size: 0.86 mm × 0.86 mm), with a matrix size of 512 × 512 pixels. The scans were acquired with a distance between consecutive slices of 0.5 mm, slice thickness ranging from 1 to 1.25 mm, convolution kernel A (Philips scanner) and standard (GE scanners), x-ray source potential of 120 kVp, tube current ranging from 138 to 188 mA, resulting in a dose index (CTDIvol) ranging from 10.0 to 11.6 mGy. A calibration phantom (Mindways Software Inc., Austin, TX) was scanned together with the subjects.

Three subjects of the validation set were selected as examples for some of the figures presented in this chapter: a healthy female (T-score of 1.1), a female with osteopenia (T-score of -2) and a female with osteoporosis (T-score of -3.9), **Figure 4.1**.

4.2.2. Statistical shape and density model generation

A statistical shape and density model was built using the 90 QCT scans collected from the training database as follows.

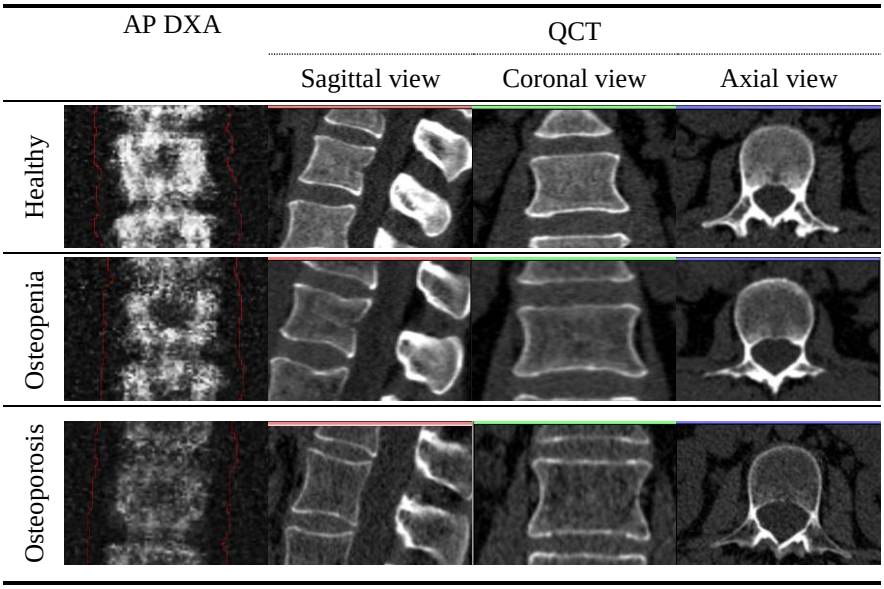

Figure 4.1: Close ups of AP DXA and QCT images.
Close ups of the L2 vertebra of subjects with normal bone density, osteopenia and osteoporosis. 1st column: AP DXA scan. 2nd to 4th columns: QCT scans (sagittal, coronal and axial view).

a) Data pre-processing

DICOM images from QCT scans were converted in volumetric images (i.e. 3-dimensional matrices where each element is a sampled density) and calibrated using the Mindways phantom. The calibration process was performed for each L1-L4 segment, for the 90 subjects in the training set, following the protocol recommended by the manufacturer.

The calibrated QCT volumes were filtered to enhance the contrast in the facet joints, thereby helping the individual segmentation of each vertebra [112], as follows. First, small groups of bright voxels at vertebral joint space were darkened using a 3D opening filter. Then, a top-hat filter was applied to highlight the brightest areas (vertebral bone); and a bottom-hat filter was applied to highlight the darkest areas (facet joints). Finally, the contrast between bone and facet joints was enhanced adding to the QCT volume the top-hat filtered volume and subtracting the bottom-hat filtered volume. The filtered QCT volumes were used only to help segmentation, not to generate the statistical density model.

Vertebrae were semi-automatically segmented in the pre-processed QCT volumes using the software TurtleSeg [113], [114], which implements the following process. The vertebral contours are manually identified in a set of non-parallel slices. The software automatically interpolates the contours to form a 3D segmentation, resulting in a volumetric mask for each vertebra. If the results are not satisfactory, additional contours are identified and the interpolation is repeated. Local deformities, such as spurs, were manually segmented by painting and erasing techniques. The segmentation process was performed for each vertebra, and for the 90 subjects in the training set. The segmentation process took between forty minutes and two hours to segment each vertebra of the L1-L4 segment, depending on the image quality and the presence of local deformities of the vertebrae.

Finally, the resulting 3D vertebral masks are subsampled and smoothed with a Gaussian filter. A triangulated surface mesh between 5638 and 15368 vertices and between 11276 and 30772 faces is generated for each vertebra[1].

b) Shape alignment

The surface meshes resulting from the segmentation process have different number and arrangement of vertices and faces. Point set registration techniques are used at each vertebral level (L1, L2, L3 and L4) to create correspondence between the vertices of the surface meshes. First, a lumbar spine having a normal aBMD (T-score $\geq$ -1) and without local deformities, such as bone spurs, is chosen among the subjects of the training set. The vertebrae L1 to L4 of the chosen lumbar spine are used as reference for its respective vertebral level. Then, the vertices of the reference mesh are non-rigidly registered onto the vertices of each surface mesh of the training set using the Coherent Point Drift (CPD) algorithm. Details of CPD algorithm can be found elsewhere [70], [71].

To improve the accuracy of the meshes resulting from the CPD registration process, each surface mesh is projected onto its

[1] Details and images showing the segmentation process are provided in Appendix A.

corresponding original surface mesh using the normal vectors of the vertices of the meshes. This sometimes results in meshes including flipped faces, which are detected by comparing the orientation of the normal vectors to the faces of the meshes after and before projection. Flipped faces are then corrected by replacing the projected vertices by its nearest point on the original surface mesh, and by smoothing the neighboring region. Projection of the mesh vertices and flipped faces detection/correction algorithm is repeated iteratively until no flipped face is detected. This results in a set of surface meshes having the same number and arrangement of vertices and faces within each vertebral level (4545, 5025, 5437 and 5421 vertices and 9090, 10050, 10874 and 10842 faces for L1, L2, L3 and L4, respectively). The accuracy of the point set registration process was evaluated by computing the signed distance between each vertex of registered reference mesh and its nearest point in the original surface mesh. At the end of the process, the mean distance ($\pm$ SD) computed for all vertebrae of the training database was -0.0017 $\pm$ 0.0765 mm, with a maximum distance of 1 mm.

Finally, the surface meshes of the L1-L4 segment obtained for the 90 subjects are aligned (scaled, rotated and translated) using Generalized Procrustes Analysis (GPA) [72].

The above-described registration process is biased by the choice of the reference shape that is used at the beginning of the process. The shape alignment process is thus iterated to correct for this bias (**Figure 4.2**). At each iteration it, the reference mesh is replaced by the average shape of the surface meshes obtained at the end of iteration $it-1$ (i.e. after GPA alignment). The point-to-surface distances between the reference shapes at iterations it and $it-1$ are computed to study the convergence of the process. The process converged after five iterations.

c) Statistical shape model

The SSM of the lumbar spine is defined as the mean position of the vertices and the main modes of variation describing the linear displacements of the vertices from their mean position [6]. Each i^{th} lumbar spine (L1-L4 segment) obtained after the shape alignment process is represented by a $3n$ element vector $\boldsymbol{s}_i = (\boldsymbol{x}_1, \boldsymbol{x}_2, \ldots \boldsymbol{x}_n)^T$ with $\boldsymbol{x} = [x, y, z]$ gathering the position of its n vertices. Principal Component Analysis (PCA) [73] is used to reduce the space dimensionality, assuming all lumbar spine shapes in the training dataset

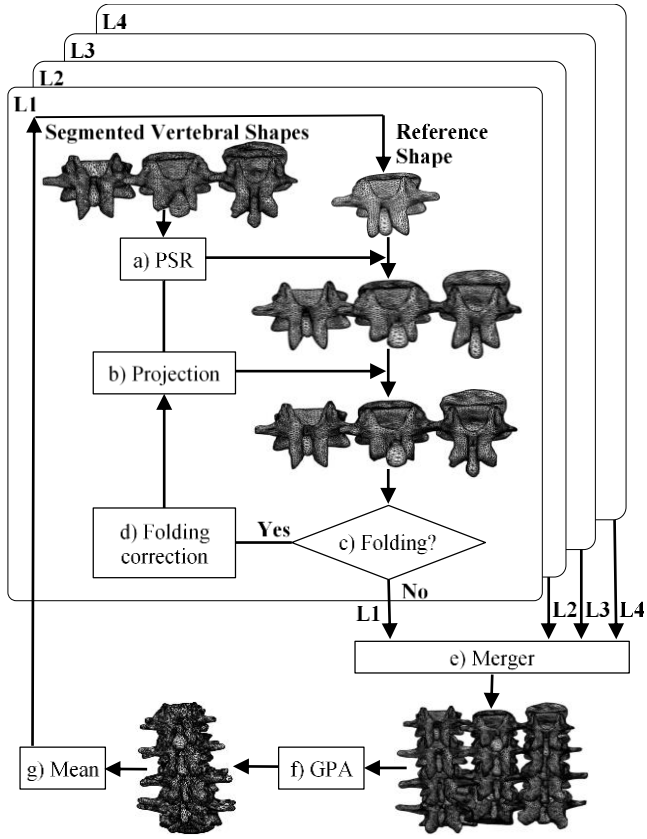

Figure 4.2: Flowchart describing spine shape alignment.
a) Point Set Registration (PSR); b) Projection using normal; c) Folded faces detection; d) Folded faces correction; e) Merge vertebrae L1 to L4 to reform spine; f) Generalized Procrustes Analysis (GPA); g) Mean of spine shapes.

follow a Gaussian distribution. The mean $\bar{\boldsymbol{s}}$ and covariance $\boldsymbol{\Sigma}$ of the point cloud take the form:

$$\bar{\boldsymbol{s}} = \frac{1}{k}\sum_{i=1}^{k} \boldsymbol{s}_i \tag{28}$$

$$\boldsymbol{\Sigma} = \frac{1}{k-1}\sum_{i=1}^{k} (\boldsymbol{s}_i - \bar{\boldsymbol{s}})(\boldsymbol{s}_i - \bar{\boldsymbol{s}})^T \tag{29}$$

where k is the number of training shapes. Eigenvectors $\boldsymbol{\rho}_j$ and eigenvalues λ_j with $j = 1, \ldots, k-1$ of the covariance matrix $\boldsymbol{\Sigma}$ are computed as described by Cootes *et al.* [9]. The eigenvectors $\boldsymbol{\rho}_j$ represent the principal modes of variation, and the eigenvalues λ_j represent the variance of the data around the mean in the direction of the corresponding eigenvector $\boldsymbol{\rho}_j$. Lumbar spine shapes in the PCA domain can be expressed as:

$$\boldsymbol{s} = \bar{\boldsymbol{s}} + \boldsymbol{P}\boldsymbol{a} \tag{30}$$

where $\boldsymbol{P} = (\boldsymbol{\rho}_1 \boldsymbol{\rho}_2 \ldots \boldsymbol{\rho}_p)$ is the matrix of the principal components (the first p modes of variation, corresponding to the most significant eigenvectors) and $\boldsymbol{a}$ is a *p*-dimensional vector of scalar coefficients weighting the contribution of each principal component.

The range of variation of the shape parameters $\boldsymbol{a}$ is bounded to avoid that implausible lumbar spine shapes are modelled. After examining the distribution of the $\boldsymbol{a}$ values required to generate the shapes of the training set [9], we choose to approximate the shape space domain (subspace of allowed shapes) by a hyperrectangular space, applying hard limits of ± 3 times the standard deviations along each principal component:

$$|a_j| < 3\sqrt{\lambda_j} \tag{31}$$

d) Volume alignment

The calibrated QCT volumes at the L1-L4 segment are aligned to remove the shape variability and to assure that the statistical density model captures only variations related to density. Thin Plate Spline (TPS) transformations [115] are computed between the mean SSM ($\bar{\boldsymbol{s}}$) of the L1-L4 segment and each one of the spine shapes obtained before GPA alignment (and after the correspondence of the vertices), **Figure 4.3**.a. 8000 vertices (resulting from the decimation of the mean shape) are used as control points to compute the TPS transformations. The accuracy of the TPS transformations was evaluated by applying the transformations to the mean shape $\bar{\boldsymbol{s}}$ and computing the signed distance between each vertex of the transformed shape and its nearest point in

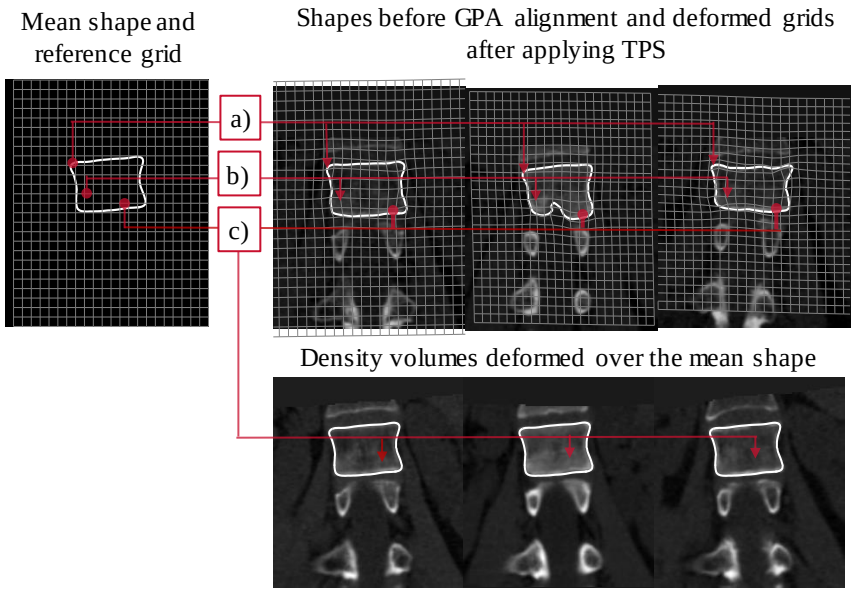

Figure 4.3: Lumbar spine volume alignment.
a) Compute TPS transformations between the mean shape and surface shapes; b) Apply TPS transformations to the reference volumetric grid; c) Interpolate and assign density values to the reference grid. The alignment process is applied to the four vertebrae simultaneously (L1-L4 segment); in this figure, only one vertebra is shown for better visualization.

the surface mesh obtained before GPA alignment. The mean distance (± SD) computed for all spine shapes of the training database was 0.00023 ± 0.14830 mm. A volumetric grid initialized over $\bar{\boldsymbol{s}}$ is used as template for sampling. The grid size is set up so that it encompasses the mean L1-L4 segment shape plus 15 mm in each direction, with a voxel size of 1 mm^3. The reference volumetric grid is filled with null values. The computed TPS transformations are applied to the reference grid to obtain 3D displacement fields, **Figure 4.3**.b. Density values at the deformed grid coordinates are computed by tri-linear interpolation in the original calibrated QCT volumes. The computed density values are used to fill the reference 3D template, **Figure 4.3**.c. This results in a set of volumetric images with the size and resolution of the 3D reference template, and the shape of the mean SSM, however maintaining their original density content.

e) Statistical density model

The statistical density model of the lumbar spine is defined as the mean density values, each one corresponding to a voxel in the reference 3D template image, and the main modes of variation describing the density distribution from their mean value. A binary mask is generated over the mean SSM ($\bar{\boldsymbol{s}}$) and applied to the aligned volumetric density images to capture only the density variations inside the 4 lumbar vertebrae. Each lumbar spine obtained after the volume alignment process is represented by an m element vector $\mathbf{g_i} = (d_1, d_2, \ldots, d_m)^T$ gathering the bone density values contained in the m voxels inside the binary mask. PCA is used to extract principal density variation modes using the computed density matrix as inputs. New density volumes are defined as:

$$\boldsymbol{g} = \bar{\boldsymbol{g}} + \boldsymbol{Q}\boldsymbol{b} \tag{32}$$

where $\bar{\mathbf{g}}$ is the mean density volume of the training set, $\boldsymbol{Q} = (\boldsymbol{\rho}_1\boldsymbol{\rho}_2 \ldots \boldsymbol{\rho}_q)$ is the matrix of the principal components (the first q modes of variation) and $\boldsymbol{b}$ is a q-dimensional vector of scalar coefficients weighting the contribution of each principal component. The parameters are calculated as in Section 4.2.2.c). Density parameters $\boldsymbol{b}$ are constrained as in *(31)*.

f) Model instance

The statistical shape and density model built is composed by a mean shape and density volume, and a set of components modelling the principal variations observed in the training set, **Figure 4.10**. An instance of the statistical model is generated as follows.

Starting from the mean density $\bar{\boldsymbol{g}}$ and the mean shape $\bar{\boldsymbol{s}}$ of the statistical model, a temporary density instance $\boldsymbol{g}$ is generated, using *(32)*, over the mean shape $\bar{\boldsymbol{s}}$, **Figure 4.4**.a. Then, a shape instance $\mathbf{s}$ is generated by deforming the mean shape $\bar{\boldsymbol{s}}$ using (30) and by subsequently applying a similarity transform $\boldsymbol{T}$:

$$\boldsymbol{T}(s) = \alpha\boldsymbol{R}\boldsymbol{s} + \boldsymbol{t} \tag{33}$$

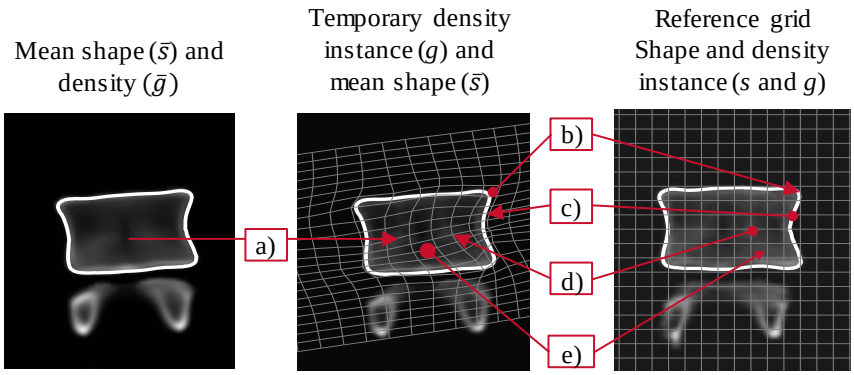

Figure 4.4: Model instance generation.
a) Generate density instance; b) Generate shape instance; c) Compute TPS transformation; d) Apply TPS transformation; e) Interpolate. The model instance is generated for the four vertebrae simultaneously (L1-L4 segment); in this figure, only one vertebra is shown for better visualization.

where α is the scaling, $\boldsymbol{R}$ the 3x3 rotation matrix determined by the rotation angles $(\theta_x, \theta_y, \theta_z)$ around $(\vec{x}, \vec{y}, \vec{z})$ axes and $\mathrm{t} = (t_x, t_y, t_z)^T$ the translation vector, **Figure 4.4**.b. Then, the temporary density instance $\boldsymbol{g}$ is deformed onto the shape instance $\mathbf{s}$ as follows. A TPS transformation between the shape instance $\mathbf{s}$ and the mean shape $\bar{\boldsymbol{s}}$ is computed using 1000 vertices as control points, **Figure 4.4**.c. The control points are obtained by decimation of the original shapes. A reference volumetric grid is created over the shape instance $\mathbf{s}$ and the calculated TPS transformation is applied to the reference grid, **Figure 4.4**.d. The density values at the transformed grid are interpolated in the temporary density instance. Finally, the reference volumetric grid is filled using the interpolated density values, **Figure 4.4**.e.

4.2.3. 3D subject-specific shape and density estimation from DXA images

A 3D subject-specific shape and density lumbar spine estimation is obtained by performing a 3D-2D registration of the statistical shape and density model onto the AP DXA scan of the patient, **Figure 4.5**. The AP DXA scans from the validation database are used to generate the DXA-derived 3D subject-specific estimations.

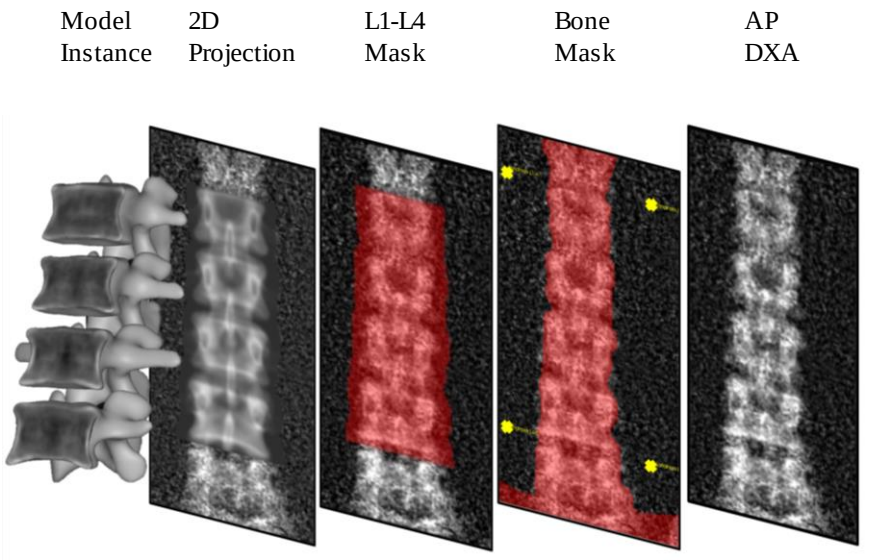

Figure 4.5: 3D-2D registration process.
Left to right: instance of the statistical shape and density model, parallel projection of the 3D model in the AP direction, 2D mask over the L1-L4 segment, mask over bony structures and landmarks, and AP DXA image.

a) 2D Mask

A 2D binary mask is automatically generated over the lumbar spine region to define the region of interest of the DXA image to be used in the 3D-2D registration process. A mask over the bony structures and a set of landmarks that defines a quadrilateral over each vertebra, both provided by the DXA scanner manufacturer software, are used. The mask over the bony structures is cropped over L1 and below L4, using the landmarks associated with these two vertebrae, (**Figure 4.5** "Bone Mask" image). Then, the resulting mask is slightly dilated in the lateral direction using a disk-shaped structural element (radius 8), (**Figure 4.5** "L1-L4 Mask" image).

b) 3D-2D Registration

The 3D-2D registration is an iterative process of registration and fitting based on a 3D-2D intensity-based registration method, **Figure 4.10**. At each iteration, an instance of the 3D model is created, and a 2D image is generated using a parallel projection of the 3D model in the AP direction, **Figure 4.5**. ("Model Instance" and "2D Projection" images). Current narrow-angle fan beam DXA scanners, such as Lunar iDXA

(GE) and Stratos dR DXA (DMS), generate AP DXA images essentially without magnification. Therefore, the density of the model instance $\boldsymbol{I}_{Model}$ is projected, using a parallel projection in the $\vec{z}$ direction, to generate the simulated 2D image $\boldsymbol{I}_{Sim}$:

$$\boldsymbol{I}_{\mathrm{Sim}}(x,y) = \sum_{z} \boldsymbol{I}_{Model}(x,y,z) \tag{34}$$

The following model instance parameters are optimized to maximize the similarity between the projection of the model instance $\boldsymbol{I}_{Sim}$ and the DXA image $\boldsymbol{I}_{DXA}$: the pose parameters $(\alpha, \theta_x, \theta_y, \theta_z, t_x, t_y)$, the shape model parameters $\boldsymbol{a}$ and the density model parameters $\boldsymbol{b}$. The translation in the $\vec{z}$ direction is not optimized because the model is projected in that direction.

The similarity between $\boldsymbol{I}_{Sim}$ and $\boldsymbol{I}_{DXA}$ is measured in the 2D binary mask region of interest as:

$$E(\alpha, \boldsymbol{\theta}, \boldsymbol{t}, \boldsymbol{a}, \boldsymbol{b}) = \frac{1}{P} \sum_{v \in Mask} (\boldsymbol{I}_{Sim}(v) - \boldsymbol{I}_{DXA}(v))^2 \tag{35}$$

where P is the number of pixels set to 1 in the mask. The parameters of the model are optimized in a 3-step process using Powell's conjugate direction method [116]. In the first step, translation and scale parameters are optimized. In the second step, the rotation is optimized in addition to the translation and scale parameters. In the third step, a non-rigid registration is performed, and all parameters are optimized. Each step is iterated until the cost function values at the current parameter and at the local extrema are within a tolerance of 0.01.

c) Model initialization

The model is initialized as follows. The scale is set to 1 and the rotation angles to 0. The initial translation is set up to align the center of the model with the center of the 2D mask (**Figure 4.5**, "L1-L4 Mask" image). The mean density and shape instance of the statistical model is used in the first iteration (shape and density parameters $\boldsymbol{a}$ and $\boldsymbol{b}$ set to 0). Shape and density model parameters $\boldsymbol{a}$ and $\boldsymbol{b}$ are bounded by (31),

thereby guaranteeing new model instances deform into lumbar spines conforming to global constraints imposed by the training set. The accurate model initialization obtained using the L1-L4 mask (**Figure 4.5**) and the coarse-to-fine registration described in Section 4.2.3.b) helps the convergence of the optimization process.

4.2.4. Geometrical and bone mineral density measurements

a) Periosteal and endocortical shapes

The cortical layer is segmented in the density volumes resulting from the 3D-2D registration process to perform a separate assessment of the cortical and trabecular bone. The periosteal (outer) and endocortical (inner) surfaces of the cortical layer are found by adapting the model-based algorithm described in Humbert *et al.* [109] as described below and illustrated in **Figure 4.6**. At each vertex of the shape model instance **s**, the density profile along the normal vector to the vertebral surface is measured by linearly interpolating in the density volume **g** (black line in **Figure 4.6**). The profile extends 2 mm outside the vertebral surface shape and 4 mm inside. The modelled density profile (grey line in **Figure 4.6**) is described as:

$$d_{mod}(\boldsymbol{x}) = d_0 + \frac{d_1 - d_0}{2}\left(1 + \operatorname{erf}\left(\frac{\boldsymbol{x} - \left(x_1 - \frac{\Delta}{2}\right)}{\sigma\sqrt{2}}\right)\right) + \frac{d_2 - d_1}{2}\left(1 + \operatorname{erf}\left(\frac{x - \left(x_1 + \frac{\Delta}{2}\right)}{\sigma\sqrt{2}}\right)\right) \quad (36)$$

where d_0,d_1 and d_2 represent the density values in the surrounding tissue, within the cortex and within the trabeculae, respectively; $\boldsymbol{x_1}$ the central position of the cortical shell; Δ is the cortical thickness; and σ is the standard deviation of the blur caused for the response of the imaging system and modelled as a normalized Gaussian function.

The position of the outer and inner surfaces of the cortical layer are determined by searching the optimal values of the cortical thickness Δ and the center position of the cortical shell $\mathbf{x_1}$, so that the modelled density matches the measured density profile. The Levenberg-Marquardt algorithm is used to find the optimal values. **Figure 4.6**

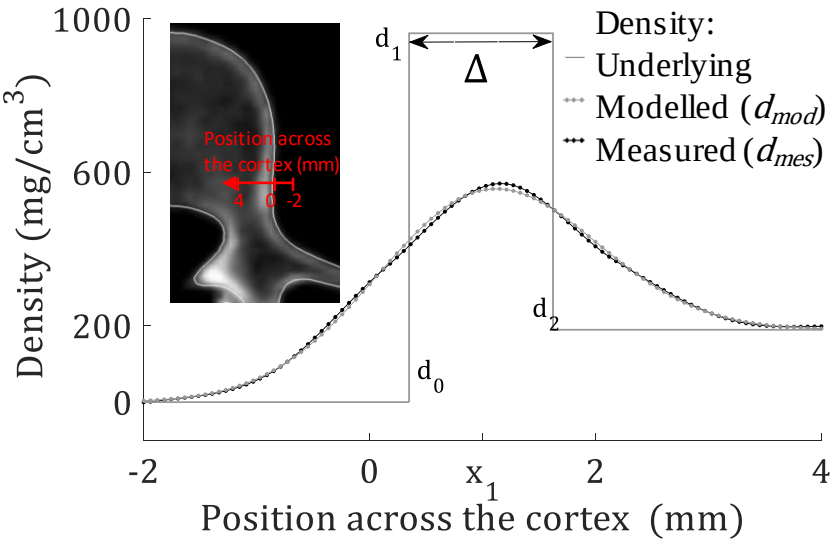

Figure 4.6: Model-based algorithm used to segment the cortical layer.
(Left) Shape and density model instance (axial view) with red line crossing the cortex shell where the density profile is measured. (Right) Density profile measured along the red line (d_{mes}) and modelled density (d_{mod}) resulting from the Gaussian blur applied to the underlying density variations. d_0, d_1, d_2 are the density values in the surrounding tissue, within the cortex, and within the trabecular bone, respectively; Δ is the cortical thickness, and x_1 the location of the center of the cortex.

shows a density model instance with line crossing the cortex shell where the density profile is measured. The measured density profile across the line is represented by the black dashed line.

In the optimization the model is constrained using prior information about the relationship between the cortical thickness Δ and the cortical density d_1, in the form of a look-up table, thus eliminating d_1 from the optimization. The periosteal and endocortical surfaces are only estimated at the vertebral body, **Figure 4.10**. The interior of the endocortical shape defines the trabecular compartment, and the volume between the periosteal and endocortical shapes the cortical one. The integral bone is the union of the cortical and trabecular bone compartments.

b) Clinical measurements

Geometry and density measurements are provided for clinical practice

purposes. Volume, BMC and vBMD are measured at the integral bone of the total vertebra and vertebral body. These measurements are also obtained for the trabecular and cortical compartments individually at the vertebral body. The cortical thickness is obtained by measuring the distance between the periosteal and endocortical surfaces. The mean cortical thickness at the vertebral body (CTh) is provided. Besides individual measurements for each vertebral level, measurements of the L1-L4 segment are also provided. In total, 65 features are measured for each subject. Finally, a surface map of the cortical thickness distribution of each vertebra is generated.

4.2.5. Validation method

The developed method was validated by comparing DXA-derived with QCT-derived 3D subject-specific shape and density estimates and clinical measurements using the validation set (180 subjects). The DXA and QCT-derived shape and density obtained for the three subjects selected as examples are shown in **Figure 4.7**.

3D subject-specific shape and density estimations (**Figure 4.7** 2nd column) were generated from the AP DXA scans of the validation set (**Figure 4.7** 1st column) by using the methodology proposed in Section 4.2.3. Two surfaces delimiting the cortical shell (periosteal and endocortical surfaces) at the vertebral bodies were estimated, and the cortical thickness and density were measured at each vertex of the surface meshes as described in Section 4.2.4.a). The clinical measurements were computed as described in Section 4.2.4.b).

On the other hand, QCT scans from the validation set were calibrated and segmented using the method described in Section 4.2.2.a) (**Figure 4.7** 3rd column). Position and curvature of the L1-L4 segments slightly differed between QCT and DXA acquisitions. For comparison purposes, each DXA-derived vertebral surface was aligned with its corresponding QCT-derived surface using rigid transformations (**Figure 4.7** 4th column). Rigid alignments were performed using the CPD algorithm [70], [71]. The region corresponding to the vertebral body of each aligned DXA-derived mesh was projected onto its corresponding QCT-derived mesh. The resulting vertebral body regions of interest, defined over the QCT surfaces, were used to estimate the cortical shell (using the model-based approach described in Section 4.2.4.a) and to compute the clinical measurements (Section 4.2.4.b).

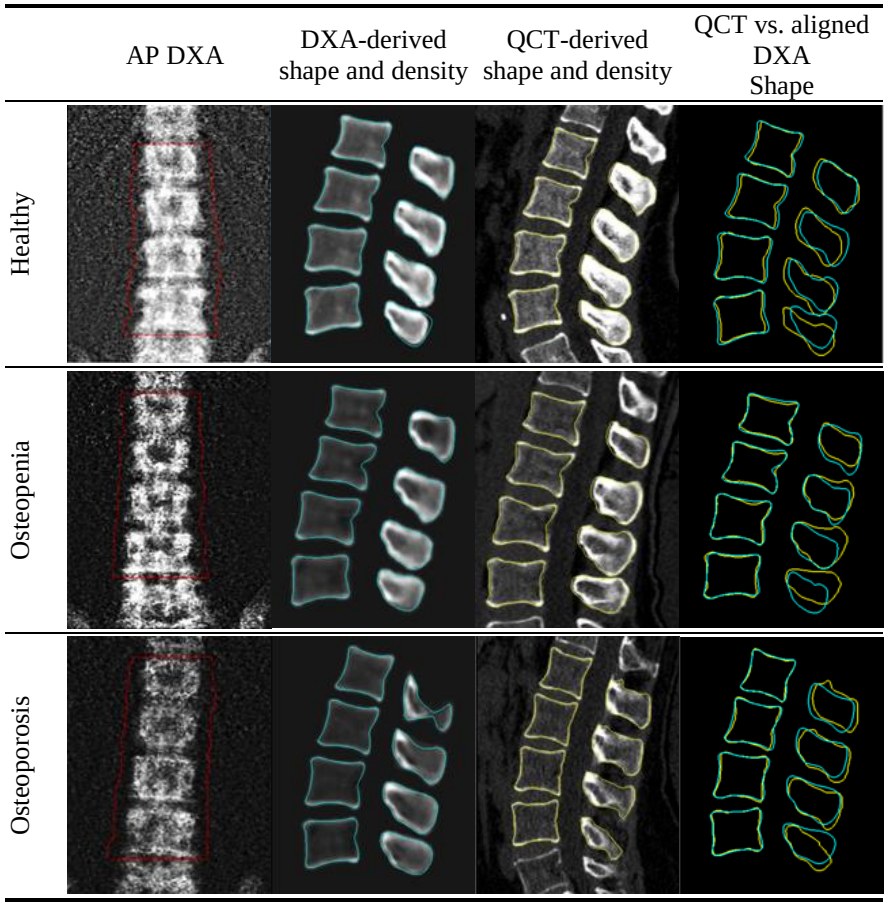

Figure 4.7: Comparison of the DXA-derived and QCT-derived 3D subject-specific shape and density of the lumbar spine for three subjects selected as examples. 1st column: AP DXA image with its 2D mask over the L1-L4 segment. 2nd column: Frontal slice of the 3D subject-specific shape and density estimated from the AP DXA image. 3rd column: Frontal slice of the QCT density and segmented shape. 4th column: QCT segmented shape and DXA-derived shape rigidly aligned onto the QCT shape.

At each vertebral level, shape accuracy was measured using the point-to-surface distances between the vertices of the aligned DXA-derived and their corresponding QCT-derived periosteal surfaces. The cortical thickness and density distributions obtained with the two modalities were compared. The linear correlations between DXA and QCT-derived measurements were evaluated using the Pearson's correlation coefficient. The statistical significance of the differences between measurements was evaluated using the Student's t-test. The experiments were done using an Intel Core i7-4790K CPU 3.60 GHz, 4 cores (8

treads), 64-bit, 16 GB of RAM with Windows 10.

4.3. Results

The training set was formed by 90 subjects (66 females and 24 males) with a mean age of 55.2 ± 11.3 years and a range between 30 and 83 years. The set was composed by 36 subjects with normal bone mass, 37 with low bone mass and 17 with osteoporosis. Mean T-score was -1.29 ± 1.31 with a range between -3.5 and 2.4.

The validation set was formed by 180 participants. 90 subjects (60 females and 30 males) with a mean age of 59.1 ± 10.5 years and a range between 28 and 84 years were scanned using the Lunar iDXA device. 90 other subjects (60 females and 30 males) with a mean age of 54.1 ± 12.3 years and a range between 22 and 84 years were scanned using the Stratos dR device. Mean T-score was -1.26 ± 1.83 with a range between -4.4 and 3.4.

4.3.1. Shape accuracy

Shape accuracy was measured at each vertebral level as described in Section 4.2.5. Average point-to-surface distance between subject-specific periosteal surfaces obtained by DXA and QCT was 1.51 mm for the L1-L4 segments Table I. A shape accuracy of 0.66 mm was achieved at the vertebral body. Similar point-to-surface distances were obtained for different vertebrae (L1 to L4) and datasets (using GE and DMS scanner). The systematic error (or bias) for the total vertebra shape was low (-0.05 mm for the L1-L4 segment), however significant (p-value < 0.01). The systematic error at the vertebral body was slightly higher (0.13 mm for the L1-L4 segment, p-value < 0.01). The random error was lower for the vertebral body (SD of 0.84 mm), compared to total vertebra (SD of 2.02 mm), due to larger errors in modeling the back process.

4.3.2. Cortical thickness and density distribution

DXA-derived and QCT-derived cortical thickness and density were compared. An average difference of -0.01 ± 0.14 mm and a mean absolute error of 0.10 mm were found for the cortical thickness in the L1-L4 segment. An average difference of -4.07 ± 74.49 mg/cm^3 and a mean absolute error of 47.00 mg/cm^3 was measured for the cortical density. The systematic error for the cortical thickness and density were

Table I: Shape Accuracy.
Point-to-surface distances (mm) between the aligned periosteal surfaces of the 3D subject-specific shapes estimated by DXA and QCT.

		All (N =180)		GE (N =90)		DMS (N =90)	
		Mean ± SD	Mean (uns.)	Mean ± SD	Mean (uns.)	Mean ± SD	Mean (uns.)
L1	Total	0.02 ± 1.80*	1.37	0.02 ± 1.82*	1.39	0.03 ± 1.78*	1.36
	Body	0.22 ± 0.85*	0.68	0.20 ± 0.86*	0.68	0.25 ± 0.85*	0.68
L2	Total	-0.03 ± 1.82*	1.39	-0.03 ± 1.83*	1.39	-0.04 ± 1.81*	1.38
	Body	0.17 ± 0.83*	0.65	0.16 ± 0.84*	0.66	0.18 ± 0.83*	0.65
L3	Total	-0.06 ± 4.05*	1.53	-0.09 ± 2.03*	1.52	-0.04 ± 2.06*	1.53
	Body	0.09 ± 0.82*	0.63	0.06 ± 0.81*	0.63	0.13 ± 0.83*	0.64
L4	Total	-0.10 ± 2.35*	1.72	-0.15 ± 2.34*	1.71	-0.05 ± 2.35*	1.73
	Body	0.06 ± 0.86*	0.67	0.02 ± 0.86*	0.68	0.10 ± 0.86*	0.67
L1-L4 segment	Total	-0.05 ± 2.02*	1.51	-0.06 ± 2.02*	1.51	-0.03 ± 2.0*	1.51
	Body	0.13 ± 0.84*	0.66	0.11 ± 0.85*	0.66	0.16 ± 0.93*	0.66

* p-value < 0.01, Student's Test

Mean ± Standard Deviation (SD) of the signed distances and mean of the unsigned (uns.) distances. Region of interest: vertebral shape ("Total") and vertebral body ("Body").

low, however significant (p-value < 0.01). Differences for each vertebral level and each dataset were similar, Table II.

The DXA and QCT-derived cortical thickness distribution obtained for the three example subjects are shown in **Figure 4.8**. Cortical thicknesses follow a similar distribution between each pair, although the DXA-derived cortical thickness tends to be slightly thinner than the QCT-derived. The figure also shows that the healthy subject has a higher cortical thickness, compared to the subject with osteopenia and osteoporosis.

4.3.3. Clinical measurements

DXA and QCT-derived clinical measurements for the L1-L4 segment were compared, Table III. DXA and QCT-derived clinical measurements and their comparison for each vertebral level (i.e. L1, L2, L3 and L4) are provided in Appendix B. A correlation coefficient (R) of 0.91 was found between DXA and QCT-derived integral vBMD at the total vertebra, and of 0.85 at the vertebral body (whole database).

Table II: DXA and QCT-derived cortical thickness and density measurements. Comparison between the cortical thickness and density computed at each node of the DXA-derived and QCT-derived periosteal surfaces: values, differences (Mean ± Standard Deviation (SD)) and Mean Absolute Error (MAE).

		ALL (N = 180)				GE (N = 90)		DMS (N = 90)	
		QCT-derived	DXA-derived	Difference (DXA - QCT)		Difference (DXA - QCT)		Difference (DXA - QCT)	
		Mean ± SD	Mean ± SD	Mean ± SD	MAE	Mean ± SD	MAE	Mean ± SD	MAE
Cortical Thickness (mm)	L1	0.69 ± 0.16	0.71 ± 0.15	0.02 ± 0.13*	0.10	0.02 ± 0.14*	0.11	0.01 ± 0.13*	0.10
	L2	0.71 ± 0.17	0.69 ± 0.16	-0.02 ± 0.13*	0.10	-0.01 ± 0.13*	0.10	-0.03 ± 0.12*	0.09
	L3	0.73 ± 0.18	0.70 ± 0.17	-0.02 ± 0.13*	0.10	-0.01 ± 0.13*	0.10	-0.04 ± 0.12*	0.10
	L4	0.75 ± 0.18	0.73 ± 0.17	-0.02 ± 0.14*	0.11	-0.01 ± 0.15*	0.12	-0.03 ± 0.13*	0.10
	L1-L4 segment	0.72 ± 0.18	0.71 ± 0.16	-0.01 ± 0.14*	0.10	0.00 ± 0.15*	0.11	-0.02 ± 0.14*	0.10
Cortical Density (mg/cm^3)	L1	783.01 ± 80.65	792.84 ± 68.30	9.83 ± 75.40*	48.86	12.92 ± 75.37*	50.20	6.73 ± 75.29*	47.52
	L2	793.46 ± 78.69	784.11 ± 73.24	-9.35 ± 70.78*	45.74	-4.94 ± 70.18*	45.15	-13.77 ± 71.11*	46.33
	L3	797.49 ± 81.70	788.49 ± 75.50	-8.99 ± 72.20*	44.78	-3.03 ± 72.07*	44.06	-14.95 ± 71.84*	45.49
	L4	804.86 ± 83.35	797.81 ± 75.35	-7.05 ± 77.84*	48.78	-2.70 ± 80.44*	50.47	-11.40 ± 74.90*	47.11
	L1-L4 segment	794.83 ± 81.49	790.76 ± 73.39	-4.07 ± 74.49*	47.00	0.41 ± 74.91*	47.41	-8.55 ± 73.79*	46.59

*p-value < 0.01, Student's Test

The R-values ranged from 0.81 to 0.97, depending on the clinical measurements and datasets used. R-values obtained for vBMD and BMC in the cortical layer were slightly higher than the ones found for the trabecular compartment. Using the whole database of subjects, the integral vBMD of total vertebra was on average higher when estimated by DXA, compared to QCT (4.63 ± 23.82 mg/cm^3), although this difference was not significant. A statistically significant difference between DXA and QCT-derived measurements was found for the trabecular vBMD and BMC at the vertebral body ($p < 0.01$), when the whole database is compared. The DXA-derived vBMD value was plotted against its corresponding QCT-derived vBMD measure for each subject of the DMS validation set, **Figure 4.9**.

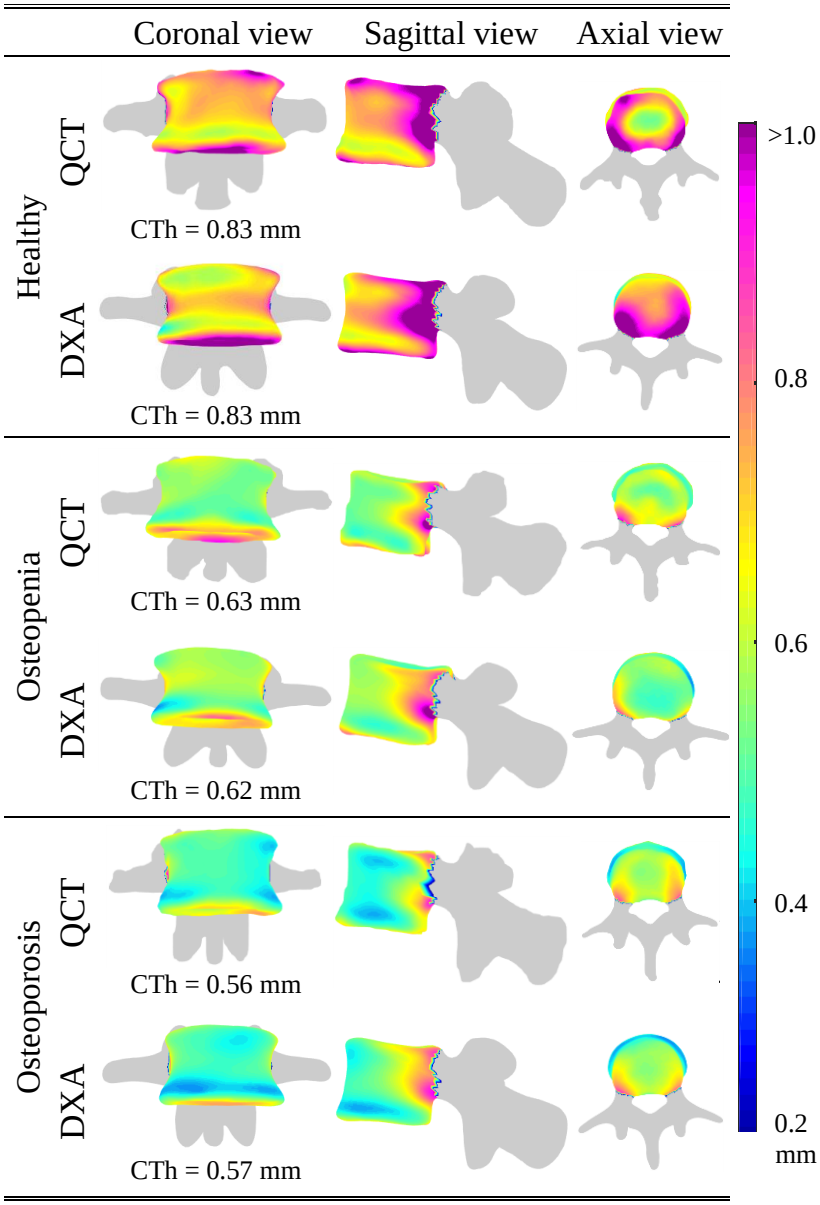

Figure 4.8: Comparison of DXA-derived and QCT-derived cortical thickness distribution for the three subjects selected as examples.

Table III: DXA and QCT-derived clinical measurements at L1-L4 segment.
Values (mean ± standard deviation) and differences (mean ± standard deviation) between DXA-derived and QCT-derived clinical measurements: Values and correlation coefficients R are provided for the total vertebra ("Total") and vertebral bodies ("Body").

L1 – L4 Segment			All (N = 180)				GE (N = 90)		DMS (N = 90)	
			QCT	DXA	Difference (DXA - QCT)		Difference (DXA - QCT)		Difference (DXA - QCT)	
			Mean ± SD	Mean ± SD	Mean ± SD	R**	Mean ± SD	R**	Mean ± SD	R**
vBMD (mg/cm³)	Integral	Total	281.65 ± 55.38	286.28 ± 57.31	4.63 ± 23.82	0.91	11.32 ± 23.73	0.91	-2.05 ± 22.08	0.93
		Body	212.61 ± 44.88	219.16 ± 43.32	6.55 ± 23.84	0.85	8.23 ± 24.36	0.83	4.87 ± 23.33	0.87
	Trabecular	Body	150.32 ± 40.35	161.57 ± 38.85	11.25 ± 23.31*	0.83	12.12 ± 23.30	0.81	10.37 ± 23.43	0.85
	Cortical	Body	611.18 ± 46.26	610.43 ± 40.77	-0.74 ± 25.14	0.84	0.82 ± 26.82	0.82	-2.30 ± 23.38	0.86
BMC (g)	Integral	Total	51.97 ± 13.90	52.46 ± 14.28	0.49 ± 4.29	0.95	1.49 ± 4.57	0.95	-0.51 ± 3.77	0.96
		Body	24.62 ± 6.79	25.86 ± 6.99	1.25 ± 2.82	0.92	1.31 ± 3.03	0.91	1.18 ± 2.61	0.93
	Trabecular	Body	15.04 ± 4.75	16.61 ± 4.95	1.56 ± 2.49*	0.87	1.54 ± 2.65	0.86	1.59 ± 2.35*	0.88
	Cortical	Body	9.58 ± 2.34	9.26 ± 2.20	-0.32 ± 0.88	0.93	-0.23 ± 0.92	0.93	-0.41 ± 0.84	0.93
Volume (cm³)	Integral	Total	184.80 ± 34.37	183.49 ± 33.78	-1.31 ± 9.33	0.96	-2.24 ± 9.65	0.96	-0.38 ± 8.95	0.97
		Body	116.17 ± 22.42	118.14 ± 21.83	1.97 ± 6.56	0.96	1.31 ± 6.48	0.96	2.63 ± 6.61	0.96
	Trabecular	Body	100.62 ± 20.12	103.08 ± 19.55	2.46 ± 6.34	0.95	1.69 ± 6.24	0.95	3.23 ± 6.39	0.95
	Cortical	Body	15.55 ± 2.92	15.05 ± 2.81	-0.49 ± 1.04	0.93	-0.38 ± 1.09	0.93	-0.60 ± 0.99	0.94
CTh (mm)	Cortical	Body	0.72 ± 0.08	0.71 ± 0.08	-0.02 ± 0.05	0.83	-0.01 ± 0.05	0.82	-0.03 ± 0.04	0.86

*p-value < 0.01, Student's Test

**R with p-value < 0.01 for all measurements.

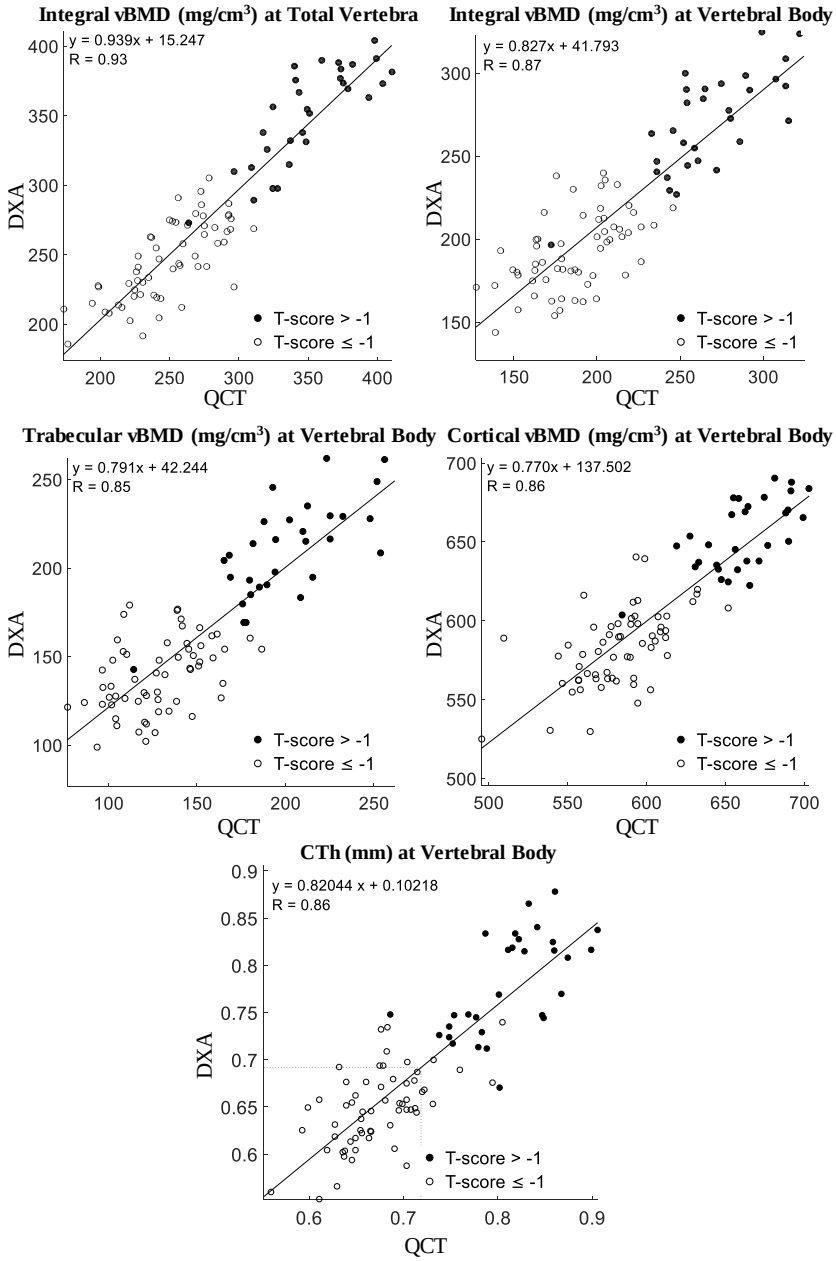

Figure 4.9: Linear regressions between DXA and QCT-derived vBMD assessed in the L1-L4 segment for different regions of interest.
Black circles represent healthy subject (T-score ≥ -1) and white circles represent patients with osteopenia or osteoporosis (T-score ≤ -1).
*p-value < 0.05, Student's Test.

The mean computing time to generate the DXA-derived 3D subject-specific models and clinical measurements was 3 min 28 s and ranged between 2 min 38 s and 5 min 31 s.

4.4. Discussion

In this chapter, we introduced a method to estimate the 3D shape and vBMD distribution of the lumbar spine (L1-L4 segment) from a single AP DXA image, and to assess the cortical and trabecular bone. The method proposed is fully automated: no user iteration is needed, **Figure 4.10**. Most of state-of-the-art 3D modelling methods require a set of landmarks to be positioned in the DXA image, [18], [19], [21]. We further developed the algorithm integrated into 3D-Shaper® for the femur to include the lumbar spine **Figure 4.11**.

An Intel Core i7-4790K CPU 3.60 GHz was used to process the AP DXA scans and obtained the 3D subject-specific models. The mean (±SD) number of iterations was 1628 ± 218, achieving a mean computing time of 3 min 28 s. The computing time mostly depended on the size of the region of interest used in the 3D-2D registration process (L1-L4 mask, **Figure 4.5**). The larger or wider the L1-L4 segment, the higher the computing time. Low computation time is one of the requirements of clinical practice. Humbert *et al.* [20] achieved the lowest computing time for the femur (1 min 30 s using an Intel Core i7-4790K CPU 4.0 GHz), in comparison with Väänänen *et al.* [19] (40 hours using an Intel Sandy Bridge 2.6 GHz) or Whitmarsh *et al.* [18] (1 hour using an Intel Core i7 CPU 920 2.67 GHz). The method developed by Whitmarsh *et al.* [21] took more than 4 h (using an Intel Core i7 CPU 920 2.67 GHz) to generate a 3D subject-specific estimation of the L2-L4 segment. We use C++, ITK and multi-core system techniques to achieve low computation times. Geometry of the spine is more complex than the one of the femur (our model had 20428 nodes, against 5546 for [20]; and four bone structures are assessed instead of one, which explains a higher computing time. This average computing time of less than 5 min, however, should be sufficiently low for the method to be used in clinical practice.

Regarding the shape accuracy, we reported mean unsigned distances between DXA and QCT-derived surfaces in a range between 1.37 mm and 1.72 mm at the total vertebra and between 0.63 mm and 0.68 mm at the vertebral body (Table I). Whitmarsh *et al.* [21] reported lower

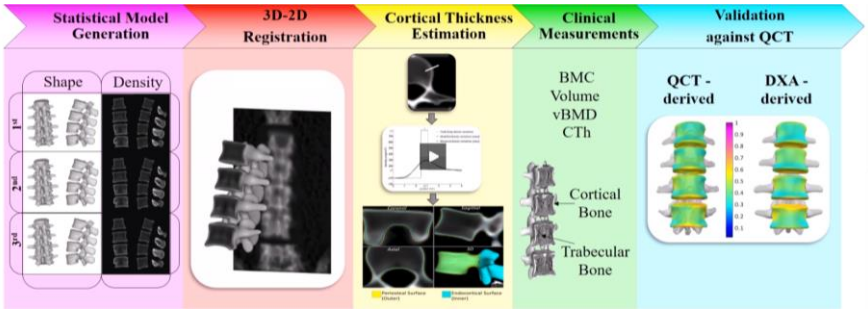

Figure 4.10: Workflow of the proposed method.
It can be seen in a video abstract available in:
https://ieeexplore.ieee.org/document/8379363
a) Statistical model variations in the three principal directions; b) 3D-2D registration process; c) Cortex analysis; d) Clinical measurements at different vertebral regions and bone compartments; e) Validation method.

errors at the total vertebra (between 1.00 mm and 1.34 mm), but larger errors at the vertebral body (between 0.73 mm and 1.12 mm). We found similar correlation coefficients (R) for the vBMD. Our R-values ranged between 0.90 and 0.92 for the integral vBMD at the total vertebra, versus 0.86 and 0.93 in [21]. At the vertebral body, we achieved R-values between 0.82 and 0.85 (integral vBMD) and between 0.79 and 0.83 (trabecular vBMD) versus 0.80 and 0.89 (integral vBMD) and 0.82 and 0.90 (trabecular vBMD) in [21]. Reported results in [21] show lower errors in modeling the shape of the posterior processes, compared to our results, which can be explained using both AP and lateral DXA projection. However, a slightly lower accuracy in modelling the vertebral body shape was found. One important limitation of the method proposed in [21] is the use of the lateral DXA scans, which are not currently used in clinical practice. Moreover, no specific algorithm was proposed to quantify the cortical bone and L1 was not assessed. In Humbert *et al.* [20], a similar approach to the one proposed in our thesis was developed for the proximal femur. They reported R-values of 0.95, 0.85 and 0.94 (integral, trabecular and cortical vBMD) at the total femur, against 0.85, 0.83 and 0.84 at the L1-L4 segment vertebral bodies in our work. Regarding the CTh, they achieved an R-value of 0.92, against 0.83 in the present thesis. The slightly lower accuracy reported in our work can be explained by the fact that the geometry of the spine is more complex than the one of the femur, the cortex is on average thinner in the vertebral body, compared to the total femur region of interest, and

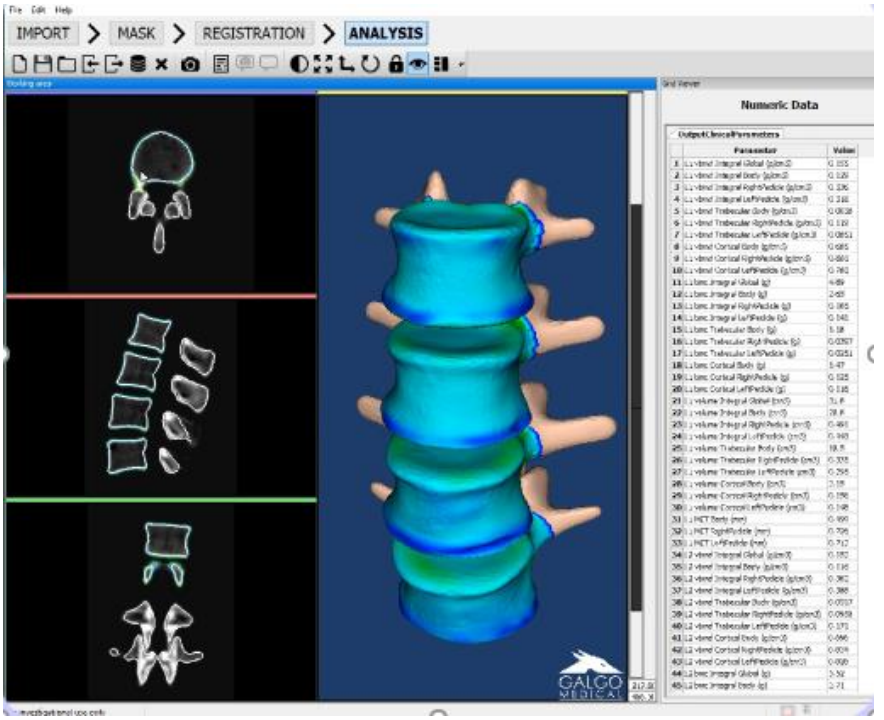

Figure 4.11: Screenshot of the developed method integrated into 3D-Shaper®. The workflow can be seen in a video abstract available in: https://ieeexplore.ieee.org/document/8379363

the spine DXA scans are noisier than hip DXA scans.

In the 180 subjects included in this study, bone masks and landmarks at L1-L4 segment (**Figure 4.5**, "Bone Mask") automatically provided by the software of the DXA manufacturers were accurate enough to provide proper identification of the "L1-L4 Mask" (**Figure 4.5**) to be used to initialize the statistical model and performed the registration. However, this process might fail, especially in the presence of pathologies such as severe scoliosis or severe osteoarthritis. In this case, manual input for the operator would be required to modify the data provided by the software of the DXA manufacturer prior to run the 2D/3D modeling process.

Modeling the outer and inner surfaces of the cortical shell was only performed in the vertebral body. The complex geometry of the back processes would make the segmentation of the cortical bone in this region of interest particularly challenging.

The lumbar vertebrae included in the training and validation databases are not only affected by bone density loss due to osteoporosis, but also by shape deformation due to degenerative osteoarthritis, compression, or the presence of calcifications (local accumulation of bone mineral) in the periphery of the vertebral body. Osteoarthritis is the most common of these conditions, with estimated rates as high as 40% in women older than 50 years, and 60% in those older than 70 years [117]. Our shape and density statistical model was mainly designed to capture global variations, while very local variations (as bone spurs, or osteophytes) were not included. Moreover, osteophytes are often not seen in the AP DXA scans. Therefore, the method proposed in our thesis could hardly model local deformities, which is an important limitation. The accuracy in measuring the cortical bone volume and CTh is directly impacted by this limitation. Future work should consider the development of advanced statistical models for the lumbar spine, including articulated and/or multi-level model, which should be more accurate in modeling local deformations and the posterior arch of the vertebra.

The presence of osteoarthritis can also lead to a wrong diagnosis of the disease, since local accumulation of bone mineral at the periosteal surface might lead to an overestimation of the aBMD computed by DXA, and hence, to a higher T-score. In this sense, the DXA-derived 3D measurements of the trabecular bone at the vertebral body could provide an alternative measurement, overcoming this limitation by discarding bone spurs, local deformations at the periosteal surface, or in the back processes.

Our algorithm cannot model fractured vertebrae since the presence of fracture was an exclusion criterion for the subjects to be included to build the statistical model. This could, however, be handled by manually, or automatically, hiding the fractured vertebra(s) in the 2D mask to be used in the registration process. The L1-L4 model would be registered as described in Section 4.2.3. The excluded region of interest (for example L3) would be statistically estimated based on the regions included (L1-L2-L4) and could be subsequently discarded in the following processing steps (cortical shell modeling, and clinical measurements). As future research, other measurements that could arise clinical interest in the lumbar spine should include: the intervertebral space, the lumbar curvature (so-called lordosis) and vertebral body heights, which are parameters associated to fracture risk.

4.5. Conclusion

To the best of our knowledge, the method proposed in this chapter is the first attempt in the literature to estimate the 3D subject-specific shape and density of the lumbar spine from a single AP DXA scan, which makes it fully compatible with current clinical practices. We proposed a separate assessment of the cortical and the trabecular compartments, and gave special emphasis to the vertebral body, which is the most affected region by osteoporotic fractures. A very good agreement was found between the DXA-derived and QCT-derived clinical measurements that were evaluated in this thesis. This method could potentially improve osteoporosis and fracture risk management in patients who had an AP DXA scan of the lumbar spine without any additional examination.

Chapter 5

5. DISCRIMINATION OF OSTEOPOROSIS-RELATED VERTEBRAL FRACTURES BY DXA-DERIVED 3D MEASUREMENTS: A RETROSPECTIVE CASE-CONTROL STUDY

Abstract - The aim of the present study was to evaluate the association of DXA-derived 3D measurements at lumbar spine with osteoporosis-related vertebral fractures. We retrospectively analyzed a database of 74 postmenopausal women: 37 subjects with incident vertebral fractures and 37 age-matched controls without any type of fracture. DXA scans at lumbar spine were acquired at baseline (i.e. before the fracture event for subjects in the fractur group) and aBMD was measured. DXA-derived 3D measurements, such as vBMD, were assessed using a DXA-based 3D modeling software (3D-Shaper® Spine). vBMD was computed at trabecular, cortical and integral bone. Cortical thickness and cortical surface BMD were also measured. Differences in DXA-derived measurements between fracture and control groups were evaluated using unpaired t-test. Odds ratio (OR) and area under the receiver operating curve (AUC) were also computed. Subgroup analyses according to fractured vertebra were performed. aBMD of fracture group was 9.3% lower compared to control group ($p<0.01$); a higher difference was found for trabecular vBMD in the vertebral body (-16.1%, $p<0.001$). Trabecular vBMD was the measurement that best discriminated between fracture and control groups, with an AUC of 0.733, against 0.682 for aBMD. Overall, similar findings were observed within the subgroup analyses. The L1 vertebral fractures subgroup had the highest AUC at trabecular vBMD (0.827), against aBMD (0.758). This study showed the ability of cortical and trabecular measurements from DXA-derived 3D models to discriminate between fracture and control groups. Large cohorts need to be analyzed to determine if these measurements could improve fracture risk prediction in clinical practice.

The content of this chapter is adapted from the following publication:

M. López Picazo, L. Humbert, S. Di Gregorio, M. A. González Ballester, and L. M. del Río Barquero. "Discrimination of osteoporosis-related vertebral fractures by DXA-derived 3D measurements: A retrospective case-control study, Osteoporosis International (Under review)

5.1. Introduction

The absence of symptoms in the early stage of the osteoporosis disease leads to millions of people remaining undiagnosed and untreated, increasing their probabilities to suffer from a fracture. Vertebral fractures, the most common osteoporosis-related fracture [118], occur after low impact trauma or by compression slowly over time [119]. These fractures are associated with chronic back pain, spinal deformity, limited physical functioning and an increased risk of hospitalization and mortality [120]; although they can also be asymptomatic. It is estimated that only one-third of vertebral fractures get clinical attention [119].

DXA is the standard exam for osteoporosis diagnosis and fracture risk [28], [37]. DXA provides 2D images in which the areal aBMD projected along the anteroposterior direction is measured. Low aBMD measured at AP DXA scans is among the strongest fracture risks [28], [37], [38]. A standard deviation decrease in aBMD leads to a 1.5- to 3.0-fold increased risk of fracture depending on site-specific measurement and fracture site [38]. However, a low aBMD is not enough to explain all fractures. State-of-the-art studies suggested that the risk of fracture is very high when a low aBMD is present, but by no means negligible when it is normal [28], [37], [38], [40], [121], [122]. Therefore, aBMD for fracture risk prediction has low sensitivity (detection rate) at acceptable specificity [121].

The majority of osteoporosis-related vertebral fractures are located in the vertebral body [43]. In spine AP DXA images, the vertebral body superimposes with the posterior vertebral elements, therefore the BMD in the vertebral body cannot be estimated separately. Fracture risk also depends on bone quality. Trabecular bone architecture and cortical bone thickness are important elements that determine bone quality [52]. However, trabecular and cortical bone compartments are difficult to assess separately in AP DXA scans.

As an alternative to DXA, QCT provides a 3D analysis of bone structures. vBMD in the vertebral body can be measured independently of the posterior vertebral elements, and even trabecular and cortical structures can be evaluated [28], [123], [124]. The association of QCT-derived vBMD with vertebral fracture has been studied previously [122], [125]–[129]. QCT-based finite element analysis is also used to know mechanical properties of the vertebrae and predict vertebral

fracture risk [129]–[132]. However, QCT results in exposure to a higher dose of radiation and is more expensive, compared to DXA. Consequently, QCT is rarely used in clinical practice for fracture risk evaluation.

To overcome the limitations of DXA and QCT, 3D modeling methods were proposed to estimate the 3D shape and density distribution of bones from a limited number of DXA scans [17], [19]–[21], [133]. Those approaches use a statistical 3D shape and density model of the bone, built from a training set of QCT scans, which is registered onto the DXA scans to obtain the 3D subject-specific QCT-like model of the bone. Whitmarsh *et al.* [21] obtain 3D subject-specific estimates of the lumbar spine (from L2 to L4) by registering a statistical model onto two DXA images (AP and lateral views). Although they performed measurements in the trabecular compartment, no specific algorithm is proposed to quantify the cortical bone. In the previous chapter [133], we proposed a similar method to estimate the 3D shape and vBMD at the lumbar spine (from vertebra L1 to L4) but using a single AP DXA image. This method also performs a separate assessment of the cortical and the trabecular compartments, giving special emphasis to the vertebral body. Accuracy of those methods [17], [19]–[21], [133] was evaluated by comparing DXA- and QCT-derived 3D models and measurements. However, to the best of our knowledge, no study has reported on the association of output measurements provided by DXA-based 3D modeling techniques with vertebral fracture.

This chapter presents a retrospective case-control study including postmenopausal Caucasian women who experienced a vertebral fracture event and age-matched controls. DXA-derived 3D measurements were obtained at baseline (at least one year before the vertebral fracture event for subjects in the fracture group) for each subject using lumbar spine AP DXA scans and a DXA-based 3D modeling technique [133]. The ability of DXA-derived 3D measurements to discriminate between fracture and control groups was assessed. As the fracture group included various types of vertebral fractures, subgroup analyses were performed to analyze the difference between groups depending on the type of fracture.

5.2. Materials and methods

5.2.1. Study population

We retrospectively analyzed a database collected at CETIR Grup Mèdic (Barcelona, Spain). The database is composed by postmenopausal Caucasian women over 40 years old with baseline and follow-up visits, both performed between the years 2000 and 2010. Subjects of the database were stratified in two groups: patients with incident vertebral fractures related to osteoporosis (fracture group) and age-matched subjects without any type of fracture (control group). Inclusion criteria for the fracture group were no prior osteoporotic fractures in any skeletal site at baseline visit (i.e. no prevalent fractures at baseline), incident vertebral fracture(s) related to osteoporosis at follow-up visit between one to ten years from baseline, and no incident osteoporotic fractures in any skeletal site other than spine during the follow-up period. Conversely, inclusion criteria for the control group were no prior osteoporotic fractures in any skeletal site at baseline and during at least seven years from baseline visit (i.e. no prevalent fractures at baseline and no incident fractures at follow-up visit). Individuals in both groups were excluded if they had skeletal disease other than osteoporosis, such as severe osteoarthritis, severe scoliosis, spondylitis, spinal infection or abnormal bone growth; or undergone spinal surgery. Vertebrae affected by mild local structural changes were not used as exclusion criteria for the subject, neither to discard vertebrae for the analysis. Each subject of the fracture group was age-matched ($\pm$5 years) with a subject of the control group. Clinical parameters such as age, weight, height, and BMI were collected for each subject at baseline.

Vertebral fractures were confirmed by a radiologist specialist using vertebral fracture assessment (VFA), in accordance with semi-quantitative Genant classification criteria [43]. The absence of fracture was determined by revising the clinical history of the subjects, by analyzing the AP DXA scans at baseline and follow-up visits, and by discarding any subjects showing a height decrease of 2 cm or more between baseline and follow-up visit.

Three subgroups were identified in the fracture group depending on the type of fracture. The first subgroup was composed by the subjects that had at least one lumbar vertebra fractured. The second subgroup was composed by the subjects that had at least the vertebra L1 fractured.

The third subgroup was composed by the subjects that had at least one thoracic vertebra fractured. Subjects from each subgroup may have, in addition to the type of fracture befitting with its group, other types of vertebral fractures.

This study was conducted as prescribed by the latest version of the Declaration of Helsinki. Ethical approval was given by the CETIR Grup Mèdic scientific committee for the use of retrospective clinical data and of results of bone measurements in the scope of this study. Each subject was ensured of anonymity which was maintained by using subject-specific numeric codes on all records.

5.2.2. Medical images and DXA-derived 2D measurements

A lumbar spine AP DXA scan was acquired at baseline for all subjects included in the study. DXA scans were performed using a Prodigy densitometer (GE Healthcare, Madison, WI, USA) and analyzed using enCORE software (v14.10, GE Healthcare, Madison, WI, USA). DXA scans and analyses were performed by a trained radiologist at CETIR Grup Mèdic according to the manufacturer's recommendations. DXA-derived 2D measurements, such as aBMD (in g/cm^2), BMC (in g) and area (in cm^2), were measured in the spine AP DXA scans at L1-L4 segment. T-scores were evaluated using GE-Lunar normative data for Spain.

5.2.3. DXA-derived 3D measurements

DXA-derived 3D measurements at L1-L4 segment were obtained using the software 3D-SHAPER (Galgo Medical, Barcelona, Spain) and the AP DXA scans acquired at baseline (before the fracture). 3D-SHAPER computes a 3D subject-specific shape and density model of the lumbar spine from a single AP DXA image, as described in the Chapter 4 [133], and briefly summarized thereafter. First, the 3D subject-specific estimation is obtained by registering and fitting a statistical shape and density model onto the AP DXA image. The statistical model was previously generated using a training database of QCT scans from Caucasian men and women. Then, the periosteal and endocortical surfaces of the cortical layer are searched by using a model-based algorithm [109], [133]. The algorithm computes the density profile along the normal vector at each node of the 3D surface mesh and fit to a

function of the cortical thickness and density, the location of the cortex, the density of surrounding tissues, and the imaging blur. Finally, DXA-derived 3D measurements are performed at different vertebral regions and bone compartments. vBMD (in mg/cm^3), BMC (in g) and volume (in cm^3) were measured at the integral bone of the total vertebra and the vertebral body. These measurements were also obtained for the trabecular and cortical compartments at the vertebral body. The mean cortical thickness (CTh, in mm) and the cortical surface BMD (cortical sBMD, in mg/cm^2) were measured at the vertebral body. The cortical sBMD is the amount of cortical bone per unit area integrated along the normal vector at each node of the 3D vertebral body surface mesh. It was computed as the multiplication of the cortical vBMD (in mg/cm^3) and the Cort. Th. (in cm).

5.2.4. Statistical Analysis

Descriptive statistics, including means and standard deviations (SD), were used to analyze the fracture and control groups. Differences between groups at baseline were assessed using the parametric Student's T-test, after checking for normality. A p-value < 0.05 was considered statistically significant. Univariate logistic regressions were used to investigate possible correlations between independent variables (weight, height, BMI, DXA-derived 2D and 3D measurements) and the status of the fracture. The ability of DXA-derived measurements to discriminate between fracture and control subjects was evaluated by using the area under the receiver operating characteristic curve (AUC). Odds ratio (OR) with 95% confidence intervals (CI) were calculated to estimate the odds of a vertebral fracture occurring for every 1 SD change in the DXA-derived measurements. To visualize the differences between groups in vBMD distribution, the mean 3D shape and density were computed for each group. Slices in the mid vertebral body plane were used to visualize the anatomical distribution of differences in vBMD. Cortical sBMD distribution was also computed for each group. Differences in cortical sBMD distribution were displayed onto the average shape instance. The statistical analysis was performed for the whole database and for each subgroup separately. Statistical analyses were conducted using MATLAB Academic (release R2015b, MathWorks, Inc., Natick, Massachusetts, United States).

5.3. Results

5.3.1. Subject´s characteristic

74 postmenopausal Caucasian women were included in this study: 37 patients with osteoporosis-related vertebral fractures (fracture group) and 37 age-matched subjects without any type of fracture (control group). No significant differences (p-value ≥ 0.05) were observed in terms of age, weight, height and BMI between fracture and control groups (Table IV). Patients in the fracture group had a vertebral fracture event on average ($\pm$ SD) at 3.2 ± 2.4 years from baseline. Absence of osteoporotic fracture event was ensured for controls over an average period of 9.0 ± 1.6 years.

The fracture group was composed by 30 patients with a single vertebral fracture and 7 with multiple vertebral fractures. A total of 48 incident vertebral fractures were found in the 37 patients of the fracture group: two T4, two T7, one T8, one T9, three T10, one T11, nine T12, fifteen L1, six L2, four L3 and four L4. The information of whether the patient in the fracture group had wedge, biconcave or crush deformity was not available for all the subjects. The grade of the fracture was classified as severe (grade 3) in 28 patients.

5.3.2. DXA-derived 2D measurements

Based on the WHO classification criteria, 97% of the patients in the fracture group and 84% of the subjects in the control group had a low aBMD (L1-L4 T-score < -1). The vertebral fracture group was composed by 29 women with osteoporosis, 7 with low bone mass and 1 with normal bone mass; whereas the control group was composed by 14 women with osteoporosis, 17 with low bone mass and 6 with normal bone mass.

Mean aBMD at L1-L4 segment of vertebral fracture group (whole database) was 9.3% lower compared to control group ($p<0.01$, Table V). No significant differences were observed in BMC and area. aBMD discriminate between fracture group and controls with an AUC = 0.682. Each incremental decrease of 1 SD in aBMD was associated with an increase of twice of the odds of presenting a vertebral fracture (OR: 2.033 95% CI [1.202 – 3.438]).

Table IV: Characteristics at baseline of the subjects included in fracture and control groups according to fracture site.

	Control	Fracture	p*
Vertebral fracture (whole database)			
Number	37	37	
Age (years)	65.3 ± 8.1 [50.0 – 79.7]	65.5 ± 7.6 [48.8 – 78.2]	0.913
Weight (kg)	60.7 ± 9.2 [46.0 – 85.0]	64.1 ± 8.7 [48.8 – 85.0]	0.115
Height (cm)	155.0 ± 7.5 [140.0 – 170.0]	155.7 ± 5.5 [144.0 – 169.5]	0.666
BMI (kg/m^2)	25.3 ± 3.4 [19.6 – 32.8]	26.4 ± 3.3 [21.1 – 32.4]	0.146
Lumbar spine fracture			
Number	26	26	
Age (years)	65.8 ± 8.3 [50.0 – 79.7]	65.6 ± 7.6 [48.8 – 78.2]	0.905
Weight (kg)	60.8 ± 8.0 [46.0 – 75.0]	64.3 ± 9.3 [48.8 – 85.0]	0.151
Height (cm)	155.3 ± 8.3 [140.0 – 170.0]	156.4 ± 6.2 [144.0 – 169.5]	0.578
BMI (kg/m^2)	25.3 ± 3.2 [19.6 – 31.6]	26.3 ± 3.5 [21.1 – 32.4]	0.279
L1 vertebral fracture			
Number	15	15	
Age (years)	64.6 ± 7.7 [50.0 – 76.6]	64.0 ± 7.7 [48.8 – 75.7]	0.839
Weight (kg)	62.7 ± 7.2 [46.0 – 75.0]	65.6 ± 9.3 [54.5 – 85.0]	0.336
Height (cm)	154.3 ± 7.8 [140.0 – 170.0]	157.0 ± 7.6 [144.0 – 169.5]	0.359
BMI (kg/m^2)	26.3 ± 2.8 [21.1 – 31.6]	26.7 ± 3.4 [22.5 – 32.4]	0.780
Thoracic spine fracture			
Number	16	16	
Age (years)	63.9 ± 7.7 [50.0 – 74.0]	64.9 ± 8.4 [48.8 – 75.7]	0.738
Weight (kg)	61.7 ± 10.1 [46.0 – 85.0]	64.2 ± 8.2 [54.0 – 83.0]	0.444
Height (cm)	154.0 ± 4.7 [143.0 – 161.0]	156.0 ± 5.1 [148.0 – 169.5]	0.251
BMI (kg/m^2)	26.0 ± 3.6 [21.0 – 32.8]	26.4 ± 2.9 [22.0 – 30.8]	0.733

Results are expressed as mean ± standard deviation [minimum – maximum]
*p-values from unpaired two-sample t-test
BMI: body mass index

5.3.3. DXA-derived 3D measurements

Integral vBMD at the total vertebra of fracture group was 10.2% lower compared to control group ($p<0.01$), (whole database, Table V). At the vertebral body, differences in vBMD were more pronounced in the trabecular bone (-16.1%, $p<0.001$) than in the integral bone (-11.3%, $p<0.001$). Cortical vBMD at the vertebral body was 1.5% lower in the fracture group, although not significant ($p=0.438$). Cortical sBMD of fracture group was 6.1% lower compared to control group ($p=0.026$). The anatomical distribution of the average differences in trabecular vBMD in the vertebral body between subjects included in the fracture

Table V: Vertebral fracture (whole database): DXA-derived measurements at baseline of control and fracture groups, differences between groups, AUC and OR.

L1-L4	Control	Fracture	Differences	p*	AUC	OR [95% CI]
DXA-derived 2D measurements						
aBMD	0.936 ± 0.144	0.849 ± 0.115	-0.087 (-9.3%)	**0.005**	0.682	2.033 [1.202 – 3.438] [a]
BMC	47.4 ± 9.9	43.5 ± 8.1	-3.9 (-8.2%)	0.070	0.615	1.562 [0.957 – 2.550] [a]
Area	50.3 ± 4.5	51.1 ± 5.4	0.8 (1.6%)	0.477	0.521	0.844 [0.531 – 1.341] [b]
DXA-derived 3D measurements						
Integral bone, total vertebra						
Int. vBMD (Total)	255.7 ± 39.6	229.7 ± 32.0	-26.0 (-10.2%)	**0.003**	0.687	2.158 [1.262 – 3.691] [a]
Int. BMC (Total)	41.1 ± 8.8	37.5 ± 7.1	-3.6 (-8.8%)	0.056	0.616	1.601 [0.979 – 2.619] [a]
Int. volume (Total)	160.6 ± 21.8	163.4 ± 20.8	2.8 (1.7%)	0.574	0.541	0.874 [0.551 – 1.388] [b]
Integral bone, vertebral body						
Int. vBMD (Body)	204.6 ± 32.8	181.4 ± 21.4	-23.2 (-11.3%)	**<0.001**	0.711	2.547 [1.410 – 4.603] [a]
Int. BMC (Body)	21.1 ± 4.4	19.0 ± 3.4	-2.1 (9.8%)	**0.026**	0.636	1.757 [1.051 – 2.937] [a]
Int. volume (Body)	103.3 ± 14.8	104.8 ± 13.3	1.4 (1.4%)	0.663	0.530	0.901 [0.568 – 1.428] [b]
Trabecular bone, vertebral body						
Trab. vBMD (Body)	132.7 ± 30.2	111.3 ± 19.2	-21.4 (-16.1%)	**<0.001**	0.733	2.637 [1.422 – 4.890] [a]
Trab. BMC (Body)	11.9 ± 2.8	10.2 ± 2.0	-1.7 (-14.0%)	**0.005**	0.682	2.101 [1.217 – 3.627] [a]
Trab. volume (Body)	90.3 ± 13.5	92.1 ± 12.1	1.8 (2.0%)	0.540	0.541	0.864 [0.544 – 1.372] [b]
Cortical bone, vertebral body						
Cort. vBMD (Body)	702.4 ± 54.6	691.7 ± 62.7	-10.7 (-1.5%)	0.438	0.550	1.203 [0.758 – 1.912] [a]
Cort. BMC (Body)	9.2 ± 1.9	8.8 ± 1.8	-0.4 (-4.5%)	0.342	0.563	1.256 [0.787 – 2.005] [a]
Cort. volume (Body)	13.0 ± 1.8	12.6 ± 1.5	-0.4 (-3.0%)	0.317	0.577	1.272 [0.796 – 2.033] [a]
Cort. Th. (Body)	0.65 ± 0.06	0.63 ± 0.05	-0.03 (-4.3%)	**0.026**	0.632	1.736 [1.056 – 2.854] [a]
Cort. sBMD (Body)	51.2 ± 6.6	48.1 ± 5.0	-3.1 (-6.1%)	**0.026**	0.630	1.736 [1.055 – 2.854] [a]

Measurements of control and fracture groups are expressed as mean ± standard deviation.
Differences between groups are expressed as mean (percentage).
*p-values from unpaired two-sample t-test. p-values < 0.05 are shown in bold.
[a] Odds ratios corresponds to a 1 SD decrease in the measurement.
[b] Odds ratios corresponds to a 1 SD increase in the measurement.
AUC: area under the receiver operating curve; OR: odds ratio; CI: confidence intervals;
aBMD: areal bone mineral density (g/cm²); BMC: bone mineral content (g); area (cm²); vBMD: volumetric bone mineral density (mg/cm³); volume (cm³); Cort. Th.: cortical thickness (mm); sBMD: surface bone mineral density (mg/cm²).
Int.: integral bone; Trab.: trabecular bone; Cort.: cortical bone; Total: total vertebra; Body: vertebral body.

and control groups are shown in **Figure 5.1**. Differences in trabecular vBMD were found to be more pronounced near the endplates.

Trabecular vBMD at the vertebral body was the measurement associated with the highest AUC (0.733) and OR (2.637 [1.422 – 4.890]). Slightly lower values were found for the integral vBMD at the vertebral body (AUC of 0.711 and OR of 2.547 [1.410 – 4.603]). Cortical sBMD were associated with lower AUC (0.630) and OR (1.736 [1.055 – 2.854]). The AUC map associated with trabecular vBMD values computed at each voxel of the volumetric images of subjects included in the fracture and control groups is shown in **Figure 5.2**. Only AUC higher than the 90th percentile (AUC > 0.720) are shown. Maximum AUC was 0.815. Trabecular vBMD measurements show highest AUC when computed near the endplates.

5.3.4. Subgroup analysis

a) Lumbar spine fracture subgroup

The lumbar spine fracture subgroup was composed by 26 subjects having at least one lumbar vertebral fracture. 19 subjects had a single lumbar vertebral fracture, and 7 subjects had multiple lumbar vertebral fractures. The 26 subjects had a total of 37 vertebral fractures: two T4, one T11, five T12, fifteen L1, six L2, four L3 and four L4.

Mean aBMD of fracture subgroup was 10.1% lower compared to control subgroup ($p=0.015$, Table VI). Difference in integral vBMD was -11.2% ($p<0.01$) at the total vertebra and -11.8% ($p<0.01$) at the vertebral body. Trabecular vBMD at the vertebral body of fracture subgroup was 17.8% lower compared to controls ($p<0.01$). No significant differences were observed in measurements at the cortical bone. Trabecular vBMD was associated with the highest AUC (0.720) and OR (2.487 [1.242 – 4.979]). General and local findings for the lumbar spine fracture subgroup were similar to those obtained with the analysis of the whole database (Table VI, **Figure 5.1** and **Figure 5.2**). The 90th percentile threshold and the maximum value at the trabecular vBMD AUC map was 0.712 and 0.812, respectively (**Figure 5.2**).

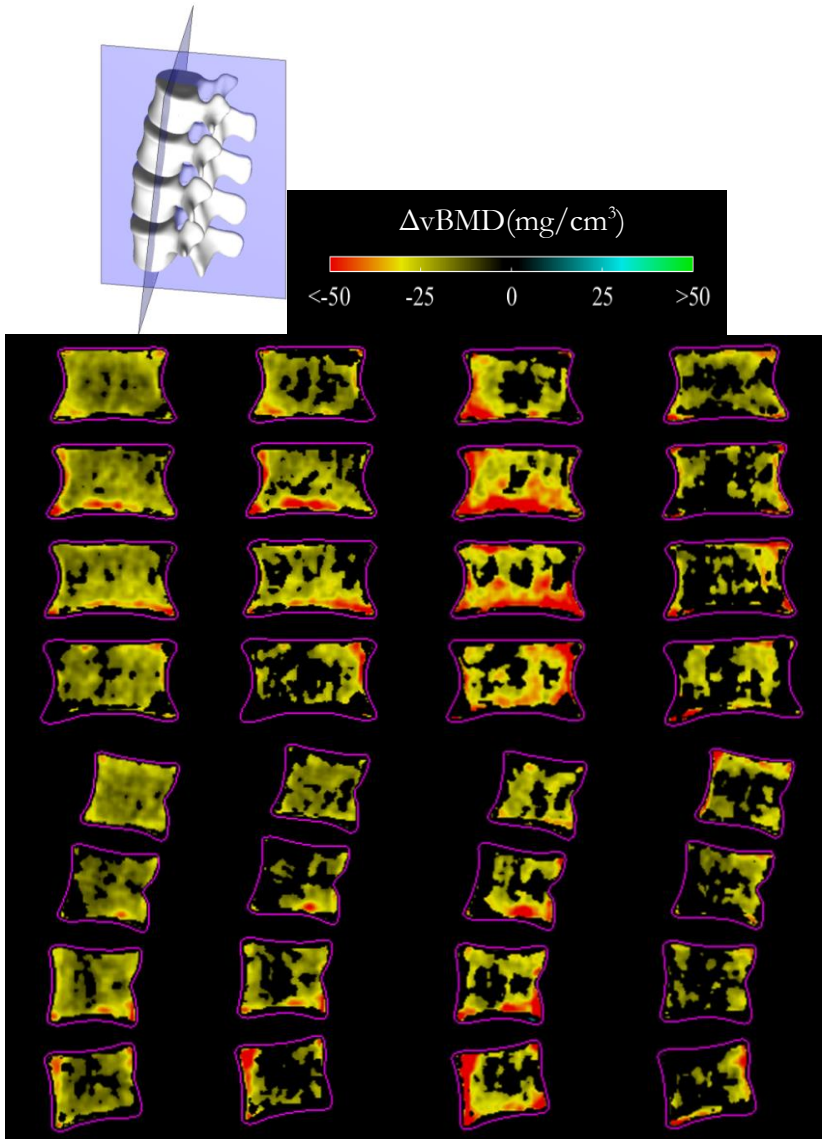

Figure 5.1: Anatomical distribution of the average changes (difference between subjects included the fracture group and subgroups, and controls) in trabecular vBMD.

Differences are shown in the mid-coronal plane (top) and mid-lateral plane (bottom) in the vertebral body. Top left image indicates the cut planes. Red-yellow (respectively blue-green) colours indicates regions where ΔvBMD is on average lower (respectively higher) for vertebral fracture subjects compared to controls. Non-significant changes (unpaired two-sample t-test) are left in black. The contour in pink indicates the periosteal surface of the vertebral body. Differences were computing using (from left to right): the whole database (N=37 in each group), the lumbar spine fracture subgroup (N=26), the L1 vertebral fracture subgroup (N=15), and the thoracic spine fracture subgroup (N=16).

b) L1 vertebral fracture subgroup

The L1 vertebral fracture subgroup was composed by 15 subjects having at least a L1 fracture. 9 subjects had only a L1 fracture and 6 subjects had multiple vertebral fractures. The 15 subjects had a total of 24 vertebral fractures: two T4, one T11, five T12, fifteen L1 and two L2.

More pronounced differences were observed in this subgroup (Table VI), especially when looking at the trabecular vBMD in the vertebral body (-23.7%, $p<0.01$). No significant differences were observed in measurements at the cortical bone. Trabecular vBMD in the vertebral body was the measurement associated with the highest AUC (0.827) and OR (5.043 [1.448 – 17.556]). Differences in trabecular vBMD were locally more pronounced (**Figure 5.1**) and associated with higher AUC (**Figure 5.2**), compared to values found when analyzing the whole database.

c) Thoracic spine fracture subgroup

The thoracic spine fracture subgroup was composed by 16 subjects having at least one thoracic vertebral fracture. 11 subjects had a single thoracic vertebral fracture and 5 subjects had multiple vertebral fractures. The 16 subjects had a total of 25 vertebral fractures: two T4, two T7, one T8, one T9, three T10, one T11, nine T12, five L1 and one L2.

No significant differences were observed in aBMD and cortical vBMD between the thoracic spine fracture subgroup and control subgroup (Table VI). In the vertebral body, differences in vBMD were more pronounced in the trabecular bone (-16.2%, $p<0.01$), than in the integral bone (-12.8%, $p<0.01$).

Trabecular vBMD was associated with the highest AUC (0.801) and OR (5.060 [1.406 – 18.208]) compared to the other DXA-derived measurements. Differences in trabecular vBMD were locally less pronounced in the thoracic spine fracture subgroup, compared to the L1 vertebral fracture subgroup (**Figure 5.1**). However, trabecular vBMD values were locally associated with higher AUC, compared to values found when analyzing the whole database (**Figure 5.2**).

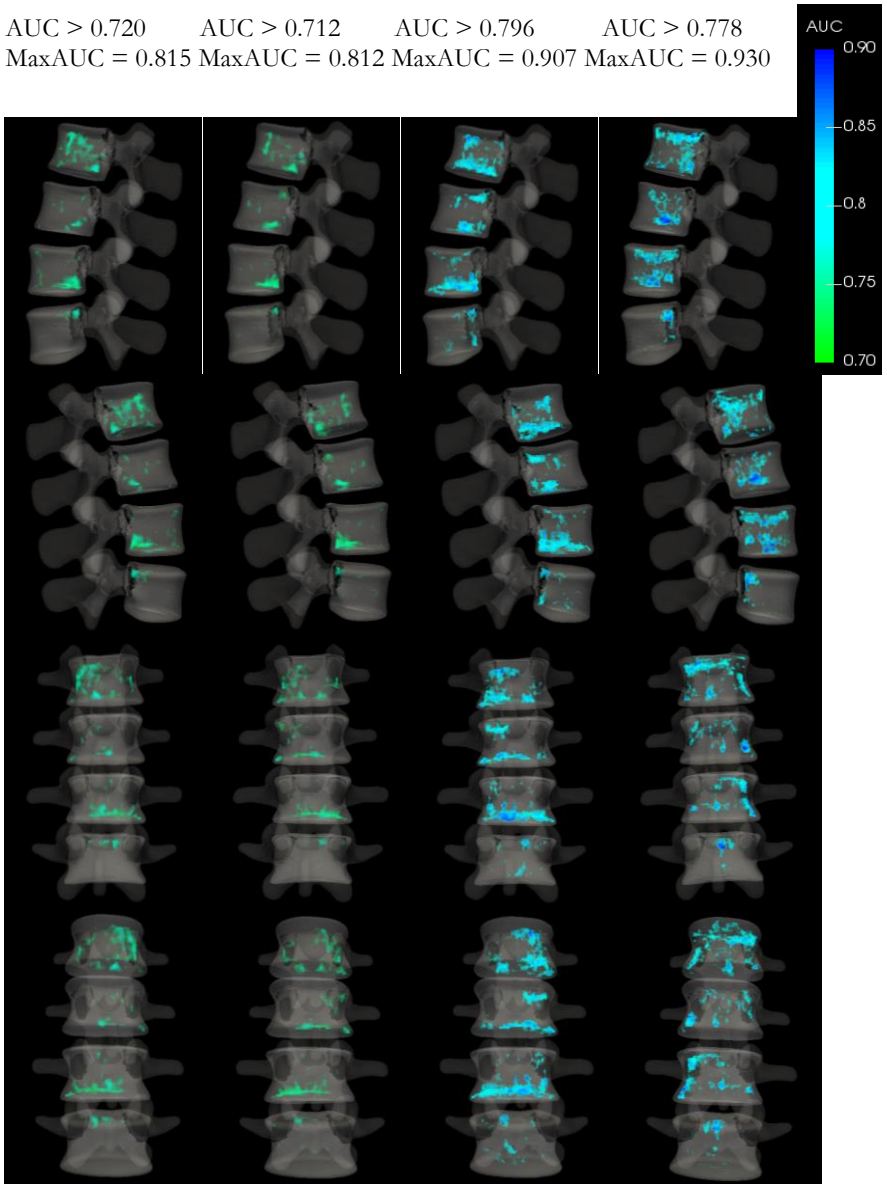

Figure 5.2: AUC map calculated using trabecular vBMD at each voxel of the volumetric images of subjects included in the fracture group and controls.
Only AUC higher than the 90th percentile are shown. Differences were computing using (from left to right): the whole database (N=37 in each group), the lumbar spine fracture subgroup (N=26), the L1 vertebral fracture subgroup (N=15), and the thoracic spine fracture subgroup (N=16).

Table VI: Subgroups analysis according to fracture site: DXA-derived measurements at baseline of subjects included in the control and fracture groups, differences between groups, AUC and OR.

L1-L4 segment	Control	Fracture	Differences	p*	AUC	OR [95% CI]
Lumbar spine fracture						
aBMD	0.945 ± 0.159	0.850 ± 0.110	-0.095 (-10.1%)	**0.015**	0.686	2.109 [1.117 – 3.982] [a]
Int. vBMD (Total)	258.9 ± 44.1	230.0 ± 32.1	-28.9 (-11.2%)	**0.009**	0.692	2.226 [1.172 – 4.226] [a]
Int. vBMD (Body)	206.0 ± 37.8	181.6 ± 22.9	-24.4 (-11.8%)	**0.007**	0.695	2.348 [1.202 – 4.589] [a]
Trab. vBMD (Body)	134.3 ± 35.1	110.4 ± 21.6	-23.9 (-17.8%)	**0.005**	0.720	2.487 [1.242 – 4.979] [a]
Cort. vBMD (Body)	700.4 ± 55.0	699.7 ± 53.8	-0.7 (-0.1%)	0.963	0.501	1.013 [0.585 – 1.754] [a]
Cort. Th. (Body)	0.66 ± 0.07	0.63 ± 0.05	-0.03 (-4.0%)	0.100	0.608	1.623 [0.907 – 2.906] [a]
Cort. sBMD (Body)	51.5 ± 7.3	48.6 ± 5.1	-2.9 (-5.7%)	0.099	0.608	1.625 [0.908 – 2.910] [a]
L1 vertebral fracture						
aBMD	0.982 ± 0.147	0.868 ± 0.115	-0.114 (-11.6%)	**0.025**	0.758	2.557 [1.068 – 6.125] [a]
Int. vBMD (Total)	272.9 ± 38.5	236.6 ± 33.6	-36.3 (-13.3%)	**0.010**	0.747	3.058 [1.186 – 7.886] [a]
Int. vBMD (Body)	220.7 ± 33.4	186.5 ± 23.6	-34.2 (-15.5%)	**0.003**	0.778	4.013 [1.354 – 11.894] [a]
Trab. vBMD (Body)	147.9 ± 30.8	112.8 ± 22.5	-35.1 (-23.7%)	**0.001**	0.827	5.043 [1.448 – 17.556] [a]
Cort. vBMD (Body)	705.6 ± 60.8	718.1 ± 54.5	12.6 (1.8%)	0.556	0.551	0.795 [0.380 – 1.661] [b]
Cort. Th. (Body)	0.67 ± 0.07	0.64 ± 0.05	-0.03 (-4.7%)	0.159	0.640	1.757 [0.803 – 3.846] [a]
Cort. sBMD (Body)	53.1 ± 7.4	49.5 ± 5.7	-3.5 (-6.6%)	0.158	0.644	1.761 [0.804 – 3.856] [a]
Thoracic spine fracture						
aBMD	0.931 ± 0.126	0.856 ± 0.133	-0.076 (-8.1%)	0.110	0.662	1.862 [0.862 – 4.022] [a]
Int. vBMD (Total)	256.2 ± 36.6	230.0 ± 34.0	-26.2 (-10.2%)	**0.044**	0.691	2.296 [0.974 – 5.413] [a]
Int. vBMD (Body)	207.6 ± 24.1	181.0 ± 20.5	-26.6 (-12.8%)	**0.002**	0.793	4.557 [1.411 – 14.718] [a]
Trab. vBMD (Body)	134.5 ± 21.2	112.7 ± 16.3	-21.8 (-16.2%)	**0.003**	0.801	5.060 [1.406 – 18.208] [a]
Cort. vBMD (Body)	704.3 ±47.9	687.9 ± 77.2	-16.3 (-2.3%)	0.477	0.543	1.307 [0.639 – 2.673] [a]
Cort. Th. (Body)	0.66 ± 0.06	0.62 ± 0.05	-0.05 (-7.1%)	**0.017**	0.734	2.659 [1.115 – 6.342] [a]
Cort. sBMD (Body)	52.2 ± 6.5	47.0 ± 5.1	-5.2 (-10.0%)	**0.018**	0.734	2.649 [1.111– 6.313]

Results are given for the subgroups analysis: lumbar spine fracture, L1 vertebral fracture and thoracic spine fracture. Measurements of control and fracture groups are expressed as mean ± standard deviation.
Differences between groups are expressed as mean (percentage). *p-values from unpaired two-sample t-test. p-values < 0.05 are shown in bold. [a] Odds ratios corresponds to a 1 SD decrease in the measurement. [b] Odds ratios corresponds to a 1 SD increase in the measurement.
AUC: area under the receiver operating curve; OR: odds ratio; CI: confidence intervals; aBMD: areal bone mineral density (g/cm^2); vBMD: volumetric bone mineral density (mg/cm^3); Cort. Th.: cortical thickness (mm); sBMD: surface bone mineral density (mg/cm^2). Int.: integral bone; Trab.: trabecular bone; Cort.: cortical bone; Total: total vertebra; Body: vertebral body.

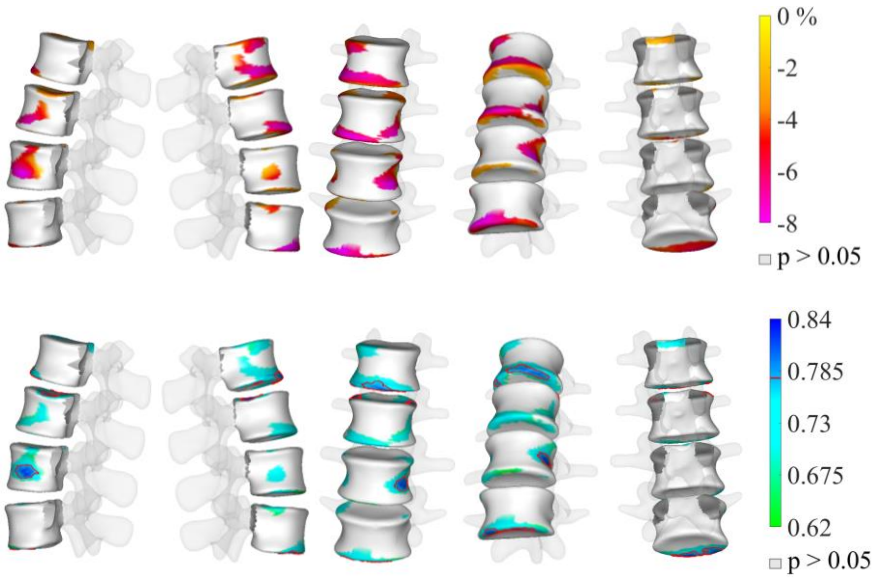

Figure 5.3: Cortical sBMD at the vertebral body.
Top: Anatomical distribution of the average differences in cortical sBMD at the vertebral body between subjects included in the thoracic spine fracture subgroup (N=16) and its respective controls (N=16). Non-significant changes (unpaired two-sample t-test) are left in grey. Bottom: AUC calculated using cortical sBMD at each vertex of the vertebral body surface of the subjects included in thoracic spine fracture and control groups. Regions where the differences in cortical sBMD were not significant (unpaired two-sample t-test) at the total vertebra region of interest are left in grey. Regions showing AUC higher than the 90th percentile (i.e. AUC > 0.777) are circled in red. Maximum AUC was 0.836.

Unlike the other subgroup's analyses, significant differences (p=0.018) were observed in cortical sBMD between the thoracic spine fracture subgroup and controls. Cortical sBMD was associated with higher AUC (0.734) and OR (2.649 [1.111 – 6.313]), compared to other measurements at the cortex. The anatomical distribution of the average differences in cortical sBMD between subjects included in thoracic spine fracture analysis and controls is shown in **Figure 5.3** (top). More pronounced differences (magenta color) were found at the endplates of vertebrae L1, L2 and L4. **Figure 5.3** also shows the AUC calculated using cortical sBMD at each vertex of the vertebral body surface. AUC higher than the 90th percentile (i.e. in the range 0.777-0.836) are circled in red and were mostly found at the endplates.

5.4. Discussion

In the present study, the ability of DXA-derived 3D measurements at lumbar spine to discriminate between postmenopausal women with and without osteoporosis-related vertebral fractures was evaluated. The DXA-derived 3D measurements were performed at baseline (at least one year before the vertebral fracture event), using standard DXA scans and a 3D modeling technique [133]. To the best our knowledge, no retrospective case-control study evaluating the association of DXA-derived 3D measurements at vertebrae L1 to L4 with osteoporosis-related vertebral fractures has been reported in the literature.

Age, sex and BMI are independent risk factors for osteoporosis-related fractures [28], [37]. In the present study, an age-matched database of postmenopausal women was used, in order to eliminate the confounding effect of age and sex. Although no inclusion criteria related to height or weight was used to recruit the subjects, no significant differences between groups were found in terms of height, weight and BMI at baseline (Table IV).

Significant differences between fracture and control groups were observed for aBMD (-9.3%, $p<0.01$), integral vBMD (-10.2%, $p<0.01$) and trabecular vBMD (-16.1%, $p<0.001$, Table V). We found slightly higher OR for DXA-derived vBMD measurements in the vertebral body (2.547 [1.410 – 4.603] at integral bone and 2.637 [1.422 – 4.890] at the trabecular bone, Table V) compared to aBMD (2.033 [1.202 – 3.438]). This is consistent with the literature, where OR for QCT-based vBMD measurements were found to be similar or higher, compared to aBMD measurements [126]–[128]. Melton *et al.* [126] reported slightly higher OR for vBMD at L1-L3 segment (2.2 [1.1 – 4.3] at the integral bone and 1.9 [1.0 – 3.6] at the trabecular bone), compared to aBMD (0.7 [0.4 – 1.2]). Anderson *et al.* [127] reported higher OR for vBMD at L3 (3.4 [1.7 – 6.8] at the integral bone and 3.4 [1.7 – 6.9] at the trabecular bone), compared to aBMD (1.9 [1.1 – 3.3]). Grampp *et al.* [128] reported higher OR for vBMD at L1-L4 segment (3.0 [1.5-6.1] at the integral bone and 4.3 [1.8 – 10.1] at the trabecular bone), compared to aBMD (2.4 [1.4 – 4.2]).

Trabecular vBMD at the vertebral body was the measurement that best discriminated between fracture and control groups, with an AUC of 0.733, against 0.682 for aBMD (Table V). Similar findings were reported

in QCT-based studies in the literature. Chalhoub *et al.* [125] reported an AUC of 0.79 for trabecular vBMD, against 0.72 for aBMD. Melton *et al.* [126] reported an AUC of 0.78 for trabecular vBMD, against 0.75 for aBMD. Grampp *et al.* [128] reported an AUC of 0.82 for trabecular vBMD, against 0.78 for aBMD. Imai *et al.* [132] reported an AUC of 0.77 for trabecular vBMD, against 0.71 for aBMD.

The use of QCT-based vBMD measurements to overcome limitations related to aBMD measurements has been proposed by several studies in the literature [28], [37], [123]–[129], [134]. DXA-derived 3D measurements have the potential to provide similar output measurements, but without the disadvantages of QCT (high financial cost and radiation dose, compared to DXA), [17], [19]–[21], [133].

Spinal degeneration, abdominal aortic calcification, and other sclerotic lesions artificially increase aBMD as measured by DXA [28], [37], [123], [134]; although patients with such pathologies have higher fracture risk. DXA-derived measurement of the trabecular vBMD in the vertebral body could be less sensitive to artefacts produced by those diseases, that are often located at the vertebral surface (cortical bone) or in the posterior arch. This could explain the higher AUC values found for trabecular vBMD measurements found in our study. In this sense, DXA-derived 3D measurements of the trabecular bone at the vertebral body could provide an alternative measurement, overcoming the limitation of aBMD-based diagnosis by discarding bone spurs, local deformations at the periosteal surface, or in the back processes [134].

In the present study, differences were less pronounced in the cortical bone (cortical sBMD: -6.1%, AUC=0.630) than in the trabecular bone (trabecular vBMD: -16.1%, AUC=0.733, Table V). Studies using biomechanical testing showed that contribution of the cortical bone to vertebral strength is usually low in normal subjects, but it could be important in older osteoporotic subjects [135], [136]. Accuracy of the DXA-derived measurements in the trabecular and cortical bone was assessed in previous work [133]. However, the cortex of the vertebral body is very thin (from 180 to 600 μm with a mean thickness of 380 μm [110]), and the DXA-based 3D modeling methods can hardly model local deformities, which could affect the accuracy of cortical bone measurements. The cortical sBMD is considered a more robust measurement of the cortical bone than cortical vBMD or Th, since it is, in general, easier to measure in low-resolution images [23], [137].

The fracture group included in this study included various types of vertebral fractures. Subgroup analyses assessing differences between groups depending on the type of fracture were also performed. The type of vertebral fractures found in the 37 cases included in this study was consistent with the literature, with a higher prevalence around the thoracolumbar junction (T12-L1) [127], [138]. Although the reason for this higher prevalence remain unknow, it has been suggested that thoracic kyphosis and the stiffness of the rib cage predispose this area to fracture by increasing vertebral loading in this location.

Overall, similar findings were observed within the subgroup's analyses (Table VI): significant differences for integral and trabecular vBMD; and no significant differences for cortical vBMD. Trabecular vBMD at the vertebral body was also the measurement that best discriminated between fracture and control subgroups. Interestingly, differences between fractured subject and controls were found to be more pronounced when analyzing the L1 vertebral fracture subgroup (trabecular vBMD: -23.7%), than when assessing the whole database (-16.1%). This can be explained by the fact that measurements were performed at L1-L4 segment, which includes the vertebra that will fracture in all subjects of the L1 vertebral fracture subgroup. This is consistent with the literature, where site-specific measurements showed higher accuracy to discriminate osteoporosis-related fractures than other sites measurements [28], [37], [38].

Although site-specific measurements showed higher accuracy, the overlying ribcage prevents the use of DXA to determine BMD in the thoracic spine. Therefore, on the third subgroup analysis, we assessed the association of DXA-derived 3D measurements at the lumbar spine with thoracic spine fractures. Interestingly, no significant differences were observed in aBMD ($p=0.110$), whereas significant differences were observed in trabecular vBMD at the vertebral body ($p<0.01$). Budoff *et al.* [139] found a high correlation between trabecular vBMD measured at the lumbar vertebrae and trabecular vBMD at thoracic vertebrae. We found higher OR and AUC for trabecular vBMD (OR = 5.060 [1.411 – 18.208], AUC = 0.801), compared to aBMD (OR = 1.862 [0.862 – 4.022], AUC = 0.662). Anderson *et al.* [127] reported higher OR for vBMD at L3 (5.3 [1.3 – 21] at the integral bone and 5.6 [1.3 – 23.4] at the trabecular bone), compared to aBMD (2.8 [1.0 – 8.0]).

Local differences between fracture and control groups were analyzed using color-coded images (**Figure 5.1**, **Figure 5.2** and **Figure 5.3**). Average differences in trabecular vBMD between subjects included in fracture groups and controls (**Figure 5.1**) and associated AUC (**Figure 5.2**) were higher near the endplates and lower in the center of the vertebral body. The endplates are the regions where tissue-level failure started, as measured in specimens with experimentally observed vertebral fracture [135], [140]–[142]. Those findings are consistent with biomechanical testing studies that show the maximum load fraction in the trabecular bone typically occurred near the endplates [132], [135], [142]. Anatomical distribution of differences in trabecular vBMD between subjects included in fracture and control groups was more uniform at the whole database than in the subgroups, and the highest difference was found in the L1 vertebral fracture subgroup (**Figure 5.1**). The L1 vertebral fracture and the thoracic spine fracture subgroups showed the highest AUCs, with maximum values of 0.907 and 0.930, respectively (**Figure 5.2**). The anatomical distribution of the average differences in cortical sBMD between subjects included in thoracic spine fracture subgroup and its respective control subgroup show more pronounced differences at the endplates (**Figure 5.3**) [135], [140]–[142]. Results showed in **Figure 5.1**, **Figure 5.2** and **Figure 5.3** were consistent with state-of-the-art studies using biomedical testing that show endplate thickness and density, and adjacent trabecular bone density as good predictors of local stiffness and strength.

The most important limitation of our study is the small number of subjects included. The main difficulties to include subjects in the fracture group were to find patients with DXA images before the incident fracture, as most of patients go to the medical office after the fracture event, and to make sure that the subjects had no prevalent osteoporosis-related fracture at any skeletal site at baseline. Besides, our study is monocentric, only includes postmenopausal Caucasian women and not all of them have the same vertebra fractured. Therefore, results can be only extrapolated to populations with similar characteristics. Also, due to the design of our study (retrospective and case-control), we cannot directly imply a causative association between reduced DXA-derived 3D measurements and osteoporosis related fracture. Another limitation is that participants included in this study did not undergo QCT examination. Therefore, we could not perform a direct comparison between the results obtained using DXA-derived 3D

measurements with QCT-derived measurements. Moreover, the presence/absence of vertebral fracture was confirmed using anteroposterior DXA scans and VFA. It would have been interesting to include other imaging modalities such as QCT or X-rays to further assess vertebral fractures.

5.5. Conclusions

This case-control study showed the association of DXA-derived 3D measurements at the lumbar spine with osteoporosis-related vertebral fractures. Lower vBMD at different vertebral regions and bone compartments were found in fracture group and subgroups compared to controls. Trabecular vBMD at the vertebral body was the measurement that best discriminated between fracture and control groups. DXA-based 3D modeling approaches could be a valuable option to complements standard DXA-derived 2D measurements in osteoporosis management. Similar studies including large cohorts will be performed in future work to determine if DXA-derived 3D measurements at the lumbar spine could improve fracture risk prediction in clinical practice.

Chapter 6

6. ASSOCIATION BETWEEN OSTEOPOROTIC FEMORAL NECK FRACTURES AND DXA-DERIVED 3D MEASUREMENTS AT LUMBAR SPINE: A CASE-CONTROL STUDY

Abstract - The aim of the present study was to evaluate the association between DXA-derived 3D measurements at lumbar spine and osteoporotic hip fractures. We analyzed a case-control database composed by 61 women with transcervical hip fractures and 61 age-matched women without any type of fracture. DXA scans at lumbar spine were acquired, and aBMD was measured. Integral, trabecular and cortical vBMD, cortical thickness and cortical sBMD at different regions of interest were assessed using a DXA-based 3D modeling software. Descriptive statistics, tests of difference, OR and AUC were used to compare hip fracture and control groups. No significant differences (p-value $\geq$ 0.05) were observed in terms of age, weight, height and BMI between fracture and control groups. Lumbar spine aBMD of fracture group was 9.9% lower compared to control group ($p<0.001$). A more pronounced difference was found for total femur aBMD (-18.8%, $p<0.001$). Integral vBMD, and cortical vBMD, sBMD and thickness were the DXA-derived 3D measurements at lumbar spine that best discriminated between fracture and control groups, with AUC's in the range of 0.685-0.726, against 0.670 for aBMD. The highest AUC (0.726) and OR (2.610) were found for integral vBMD at the posterior vertebral elements. Significantly lower AUC (0.617) and OR (1.607) were found for trabecular vBMD at the vertebral body. This study showed the association of DXA-derived measurements at lumbar spine with transcervical hip fractures. A strong association between vBMD of the posterior vertebral elements and transcervical hip fractures was observed, probably as a consequence of a global deterioration of the cortical bone component. Further studies should be carried out to investigate on the relative risk of transcervical fracture in patients with long-term cortical structural deterioration.

The content of this chapter is adapted from the following publication:

M. López Picazo, L. Humbert, R. Winzenrieth, S. Di Gregorio, M. A. González Ballester, and L. M. del Río Barquero. "Association between osteoporotic femoral neck fractures and DXA-derived 3D measurements at lumbar spine: A case-control study", Bone (Submitted).

6.1. Introduction

Osteoporosis is a common condition among postmenopausal women and is associated with a significant increase in morbidity and mortality [1], [2]. Despite being a major health condition, the absence of symptoms in the early stage of the disease leads to millions of people remaining undiagnosed and untreated, increasing their probabilities to suffer from a fracture. Hip fractures are the most serious and costly potential result of osteoporosis. Up to 20 % of patients die in the first year following hip fracture, and less than half of survivors regain the level of function that they had prior to the fracture [2]. The estimated cost of osteoporotic fractures in the EU is about 37 billion €, of which an estimated 54% account for hip fractures [33].

BMD is considered as the major determinant of bone strength and fracture risk. DXA is the reference technique in clinical practice to measure BMD for fracture risk assessment [2], [28]. DXA provides 2D images in which the aBMD (g/cm^2) projected along the anteroposterior direction is measured. State-of-the-art studies suggested that the risk of fracture is very high when a low aBMD is present, but by no means negligible when it is normal [2], [28], [40]. In fact, low aBMD only explains 60 to 80 % of bone strength under laboratory conditions [143], and only 50 % of osteoporotic fractures are observed in postmenopausal women with a T-score below -2.5 [41].

Bone quality is also an important determinant of fracture risk [42]. Bone quality refers to 3D structural characteristics of the skeleton, such as bone size, shape, mineral content distribution, trabecular bone architecture, damage accumulation, cortical bone thickness and geometry, turnover, osteon and osteocyte density and other factors such as structural proteins and crystal properties [42]. However, DXA-derived standard measurements lack information about 3D characteristics of the bone, and trabecular and cortical bone compartments cannot be assessed separately in an AP DXA scan. Besides, lumbar vertebrae are composed of a vertebral body and posterior vertebral elements. The vertebral body is a weight-bearing structure and mainly composed by trabecular bone, while the posterior vertebral elements are non-weight-bearing structures and mainly composed by cortical bone. However, AP DXA scans do not allow physicians to perform specific measurements in the vertebral body or in the posterior vertebral elements.

As an alternative, QCT provides a 3D analysis of bony structures where vBMD can be measured separately at different vertebral regions and bone compartments [28], [123], [124]. However, QCT is rarely used in clinical practice for fracture risk evaluation as it results in exposure to a higher dose of radiation and is more expensive, compared to DXA.

To overcome the limitations of DXA and QCT, 3D modelling methods were proposed to analyze bone structures in 3D from DXA scans [17], [19]–[21], [133]. Those approaches use a statistical 3D shape and density model of the bone, built from a training set of QCT scans, which is registered onto the DXA scan to obtain a 3D subject-specific QCT like model of the bone. Segmentation algorithms are used to identify the cortex in the 3D subject-specific model [19], [20], [133] and provide a separate 3D analysis of the trabecular and cortical compartments. Accuracy of those methods [17], [19]–[21], [133] was evaluated by comparing DXA-derived to QCT-derived 3D models and measurements.

The most commonly measured sites for osteoporosis and fracture risk assessment are the lumbar spine and the proximal femur. Although site-specific measurements showed higher accuracy to discriminate osteoporotic fractures than measurements at other sites [28], [37], [38], [144]–[146], the association between osteoporotic hip fractures and bone density at lumbar spine has been extensively studied using DXA [38], [144]–[147] and QCT [125], [148]–[152]. However, to the best of our knowledge, no study has reported on the association of output measurements provided by DXA-based 3D modeling techniques at lumbar spine with hip fractures.

This chapter presents a case-control study including postmenopausal women with transcervical hip fractures and postmenopausal women without any type of osteoporotic fracture. DXA-derived 3D measurements at lumbar spine were obtained for each subject using AP DXA scans and DXA-based 3D modeling techniques [133]. The association between hip fracture and DXA-derived 3D measurements at lumbar spine in different vertebral regions and bone compartments was assessed.

6.2. Materials and methods

6.2.1. Study population

A retrospective case-control study was performed using a database from CETIR Grup Mèdic (Barcelona, Spain). The database included postmenopausal Spanish women over 50 years old, referred to CETIR by their general practitioner between the years 2000 and 2005. Subjects of the database were stratified in two groups: fracture group and control group. Criterion to include the subjects in the fracture group was to present a low-energy fracture at the femoral neck (transcervical fracture). Conversely, inclusion criterion for the subjects of the control group was not present any evidence of low-energy fracture at any skeletal site. Exclusion criteria for both groups included any evidence of prior osteoporosis-related fracture at lumbar spine, any treatment that would be expected to influence bone metabolism, hormone replacement therapies, skeletal disease other than osteoporosis, such as severe osteoarthritis, severe scoliosis, spondylitis, spinal infection or abnormal bone growth, or spinal surgery. Each case who met inclusion criteria of the fracture group was randomly age-matched (±5 years) with one subject of the control group (1:1). Anthropometric measurements such as weight, height, and BMI were collected.

This study was conducted as prescribed by the latest version of the Declaration of Helsinki. Ethical approval was given by the CETIR Grup Mèdic scientific committee for the use of clinical data and of results of bone measurements in the scope of this study. Each subject was ensured of anonymity, which was maintained by using subject-specific numeric codes on all records.

6.2.2. Medical images and DXA-derived 2D measurements

DXA scans at proximal femur and at lumbar spine were performed using a Lunar Prodigy® densitometer (GE Healthcare, Madison, WI, USA) and analyzed using enCORE® software (v14.10, GE Healthcare) according to the manufacturer's recommendations. aBMD (in g/cm^2), BMC (in g) and area (in cm^2) were measured in both femur and lumbar spine DXA scans. Lumbar spine measurements were reported as the mean of the individual measurements for L1-L4 segment.

6.2.3. DXA-derived 3D measurements

3D subject-specific shape and density models and measurements at the lumbar spine were computed using the software 3D-SHAPER (Galgo Medical, Barcelona, Spain), as described in Chapter 4 [133] and briefly summarized thereafter. First, a statistical shape and density model of the L1-L4 segment, previously generated using a training database of QCT scans from Caucasian men and women, is registered and fitted onto the DXA image obtaining the 3D subject-specific model. Then, trabecular and cortical bone compartments at the vertebral body are segmented using a model-based algorithm [109], [133]. The algorithm performs the fitting of a function of the cortical thickness and density, the location of the cortex, the density of surrounding tissues, and the imaging blur to the density profile measured along the normal vector at each node of the 3D surface mesh. Finally, DXA-derived 3D measurements, such as vBMD (in mg/cm^3), BMC (in g) and volume (in cm^3), are performed at different vertebral regions (total vertebra, vertebral body and posterior vertebral elements, i.e. pedicles, transverse processes, articular processes and spinous process) and bone compartments (integral, trabecular and cortical bone). The mean cortical thickness (CTh, in mm) of the vertebral body is also computed. The cortical sBMD (in mg/cm^2) measures the amount of cortical bone per unit area integrated along the normal vector at each node of the 3D vertebral body surface mesh. It is computed as the multiplication of the cortical vBMD (in mg/cm^3) and the CTh (in cm).

6.2.4. Statistical Analysis

Descriptive statistics, including means and standard deviations (SD), were used for each group. Differences between groups were assessed using parametric two tailed Student's T-test, after checking for normality. Odds ratio (OR) with 95% confidence intervals (**CI**) were calculated to estimate the odds of a fracture occurring for every 1 SD change in the DXA-derived measurements. Area under the receiver operating curve (AUC) was also computed for each DXA-derived measurement to investigate possible associations between DXA-derived measurements and fracture. Statistical comparison between AUCs was also assessed. Statistical analyses were conducted using MATLAB Academic (release R2015b, MathWorks, Inc., Natick, Massachusetts, United States). A p-value < 0.05 was considered statistically significant.

To visualize the anatomical distribution of the differences in vBMD between fracture and control groups, the mean 3D shape and density volume were computed for each group and compared. Slices in the mid-coronal plane and mid-lateral plane were used to visualize the anatomical distribution of changes in vBMD. The mean cortical sBMD distribution was also computed for each group. Differences in cortical sBMD distribution between fracture and control groups were displayed onto the average shape instance.

6.3. Results

6.3.1. Population characteristics

One hundred twenty-two postmenopausal women met our inclusion/exclusion criteria and were included in this study: 61 patients with osteoporotic transcervical fractures (fracture group) and 61 without any type of low-energy fracture (control group). No significant differences (p-value ≥ 0.05) were observed in terms of age, weight, height and BMI between fracture and control groups (Table VII).

6.3.2. Differences in DXA-derived measurements between subjects with and without fractures

Mean aBMD was significantly lower in fracture group (Total Femur: 0.893 g/cm^2 vs. 0.725 g/cm^2, $p< 0.0001$; Femoral Neck: 0.823 g/cm^2 vs. 0.694 g/cm^2, $p<0.0001$; L1-L4: 0.964 g/cm^2 vs. 0.869 g/cm^2, $p<0.001$) (Table VIII).

Statistically significant differences were observed in all DXA-derived 3D density measurements at L1-L4 segment between fracture and control group ($p<0.05$, Table VIII). Integral vBMD at the vertebral body was significantly lower in fracture group (261.6 mg/cm^3 vs. 230.9 mg/cm^3, $p< 0.01$). A more pronounced difference between groups was found for the integral vBMD at the posterior vertebral elements (359.2 mg/cm^3 vs. 302.6 mg/cm^3, $p<0.0001$).

6.3.3. Association between DXA-derived measurements and hip fracture

An AUC of 0.838 [0.747 – 0.896] was found for aBMD at total femur and each decrease of 1 SD in the measurement correspond to an OR of

Table VII: Characteristics of the subjects included in fracture and control groups.

	Control	Hip Fracture	p*
N	61	61	
Age (years)	67.0 ± 8.0	67.4 ± 7.9	0.776
Weight (kg)	64.6 ± 8.8	62.1 ± 8.8	0.126
Height (cm)	154.1 ± 5.8	154.0 ± 6.3	0.917
BMI (kg/m^2)	27.2 ± 3.1	26.2 ± 3.3	0.099

Results are expressed as mean ± standard deviation [minimum – maximum]
*p-values from unpaired two-sample t-test
BMI: Body Mass Index

6.240 [3.145 – 12.381] (Table VIII). An AUC of 0.670 [0.573 – 0.760] and OR of 2.044 [1.343 – 3.112] were found for aBMD at L1-L4 segment. Comparison between AUCs showed that total femur aBMD was a significantly better predictor of transcervical fractures than lumbar spine aBMD (AUC=0.838 vs. 0.670, $p < 0.001$).

An AUC of 0.691 [0.599 – 0.781] and OR of 2.319 [1.493 – 3.601] were found for the integral vBMD at the total vertebra (Table IX). Similar values were found for the cortical sBMD at the vertebral body (AUC of 0.696 [0.598 – 0.781] and OR of 2.234 [1.448 – 3.447]). Lower AUC (0.617 [0.517 – 0.721]) and OR (1.607 [1.085 – 2.379]) were found for the trabecular vBMD at the vertebral body. The highest AUC (0.726 [0.633 – 0.808]) and OR (2.610 [1.662 – 4.098]) were found for the integral vBMD at the posterior vertebral elements. Comparison between AUC showed that integral vBMD at the posterior vertebral elements was a significantly better predictor of transcervical fractures than trabecular vBMD at the vertebral body (AUC = 0.726 vs. 0.617, $p < 0.001$). A borderline significant trend was found in the AUC comparison between lumbar spine aBMD and integral vBMD at the posterior vertebral elements (AUC = 0.670 vs. 0.726, $p = 0.068$). Overall, total femur aBMD remains a significantly better predictor for hip fracture, compared to aBMD or vBMD measurements at lumbar spine ($p < 0.05$).

Table VIII: DXA-derived 2D measurements of control and fracture groups, differences between groups, AUC and OR.

	Control	Fracture	Differences	p*	AUC [95% CI]	OR [95% CI]
DXA-derived 2D measurements at total femur						
aBMD	0.893 ± 0.143	0.725 ± 0.100	-0.168 (-18.8%)	**<0.0001**	0.838 [0.747 – 0.896]	6.240 [3.145 –12.381] [a]
BMC	26.8 ± 4.3	22.3 ± 3.6	-4.6 (-17.0%)	**<0.0001**	0.749 [0.702 – 0.860]	3.974 [2.288 – 6.901] [a]
Area	30.1 ± 1.8	30.7 ± 2.6	0.6 (2.1%)	0.129	0.561 [0.455 – 0.664]	1.335 [0.916 – 1.945] [b]
DXA-derived 2D measurements at femoral neck						
aBMD	0.823 ± 0.126	0.694 ± 0.071	-0.129 (-15.7%)	**<0.0001**	0.798 [0.705 – 0.870]	5.206 [2.725 – 9.946] [a]
BMC	3.9 ± 0.5	3.4 ± 0.4	-0.5 (-12.9%)	**<0.0001**	0.760 [0.668 – 0.841]	3.231 [1.967 – 5.307] [a]
Area	4.7 ± 0.3	4.9 ± 0.4	0.1 (3.1%)	**0.030**	0.603 [0.494 – 0.703]	1.512 [1.031 – 2.217] [b]
DXA-derived 2D measurements at L1 – L4 segment						
aBMD	0.964 ± 0.153	0.869 ± 0.133	-0.095 (-9.9%)	**<0.001**	0.670 [0.573 – 0.760]	2.044 [1.343 – 3.112] [a]
BMC	49.5 ± 10.3	44.7 ± 9.5	-4.8 (-9.8%)	**0.008**	0.632 [0.524 – 0.721]	1.691 [1.130 – 2.532] [a]
Area	51.1 ± 5.3	51.1 ± 5.2	-0.1 (-0.1%)	0.939	0.497 [0.391 – 0.595]	1.014 [0.710 – 1.448] [a]

Measurements of control and fracture groups are expressed as mean ± standard deviation. Differences between groups are expressed as mean (percentage).

*p-values from unpaired two-sample t-test. p-values < 0.05 are shown in bold.

[a (b)] Odds ratios corresponds to a 1 SD decrease (increase) in the measurement.

AUC: area under the receiver operating curve; OR: odds ratio; CI: confidence intervals; aBMD: areal bone mineral density (g/cm^2); BMC: bone mineral content (g); area (cm^2)

Table IX: DXA-derived 3D measurements of control and fracture groups, differences between groups, AUC and OR.

	Control	Fracture	Differences	p*	AUC [95% CI]	OR [95% CI]
DXA-derived 3D measurements at L1 – L4 segment						
Integral bone, total vertebra						
vBMD	261.6 ± 43.4	230.9 ± 36.2	-30.7 (-11.7%)	**<0.0001**	0.691 [0.599 – 0.781]	2.319 [1.493 – 3.601] [a]
BMC	43.0 ± 9.1	38.6 ± 8.7	-4.4 (-10.3%)	**0.007**	0.635 [0.538 – 0.735]	1.708 [1.138 – 2.562] [a]
Volume	164.8 ± 22.8	167.3 ± 27.2	2.5 (1.5%)	0.590	0.529 [0.432 – 0.628]	1.104 [0.772 – 1.581] [b]
Integral bone, posterior vertebral elements (pedicles, processes and facets)						
vBMD	359.2 ± 66.9	302.6 ± 61.0	-56.6 (-15.8%)	**<0.0001**	0.726 [0.633 – 0.808]	2.610 [1.662 – 4.098] [a]
BMC	20.9 ± 5.1	18.4 ± 4.8	-2.5 (-12.0%)	**0.006**	0.640 [0.532 – 0.732]	1.708 [1.147 – 2.542] [a]
Volume	58.3 ± 9.7	61.0 ± 11.9	2.7 (4.7%)	0.169	0.568 [0.457 – 0.665]	1.298 [0.892 – 1.887] [b]
Integral bone, vertebral body						
vBMD	208.4 ± 34.8	190.6 ± 30.1	-17.8 (-8.5%)	**0.003**	0.646 [0.542 – 0.743]	1.794 [1.197 – 2.689] [a]
BMC	22.1 ± 4.7	20.2 ± 4.5	-1.9 (-8.7%)	**0.022**	0.626 [0.517 – 0.718]	1.564 [1.053 – 2.322] [a]
Volume	106.5 ± 14.7	106.2 ± 17.2	-0.3 (-0.3%)	0.925	0.495 [0.376 – 0.594]	1.017 [0.712 – 1.453] [a]
Trabecular bone, vertebral body						
vBMD	150.8 ± 31.5	137.8 ± 26.1	-13.0 (-8.6%)	**0.015**	0.617 [0.517 – 0.721]	1.607 [1.085 – 2.379] [a]
BMC	14.0 ± 3.4	12.8 ± 3.1	-1.1 (-8.0%)	0.063	0.599 [0.490 – 0.698]	1.429 [0.973 – 2.098] [a]
Volume	92.9 ± 13.4	93.5 ± 15.5	0.6 (0.6%)	0.819	0.524 [0.420 – 0.628]	1.043 [0.730 – 1.490] [b]
Cortical bone, vertebral body						
vBMD	598.2 ± 31.3	574.7 ± 35.3	-23.5 (-3.9%)	**<0.001**	0.685 [0.591 – 0.772]	2.122 [1.395 – 3.226] [a]
BMC	8.2 ± 1.4	7.4 ± 1.6	-0.8 (-9.9%)	**0.003**	0.654 [0.560 – 0.745]	1.786 [1.192 – 2.676] [a]
Volume	13.6 ± 1.8	12.8 ± 2.1	-0.9 (-6.4%)	**0.016**	0.625 [0.524 – 0.727]	1.588 [1.080 – 2.335] [a]
CTh	0.67± 0.06	0.63 ± 0.06	-0.04 (-6.53%)	**<0.0001**	0.696 [0.597 – 0.788]	2.229 [1.446 – 3.437] [a]
sBMD	53.1 ± 6.4	48.3 ± 6.7	-4.8 (-9.1%)	**<0.0001**	0.696 [0.598 – 0.781]	2.234 [1.448 – 3.447] [a]

Measurements of control and fracture groups are expressed as mean ± standard deviation. Differences between groups are expressed as mean (percentage).
*p-values from unpaired two-sample t-test. p-values < 0.05 are shown in bold.
[a] [(b)] Odds ratios corresponds to a 1 SD decrease (increase) in the measurement.
AUC: area under the receiver operating curve; OR: odds ratio; CI: confidence intervals; BMC: bone mineral content (g); vBMD: volumetric bone mineral density (mg/cm^3); volume (cm^3); sBMD: surface BMD (mg/cm^2). CTh: Cortical Thickness.

6.3.4. Anatomical distribution of differences between groups

Anatomical distribution of differences between fracture and control groups were analyzed using color-coded images (**Figure 6.1**, **Figure 6.2** and **Figure 6.3**). The anatomical distribution of the average differences in integral vBMD between subjects with and without fracture is presented in **Figure 6.1**. Analysis of the distribution highlighted that differences in integral vBMD were more pronounces at the posterior vertebral elements than at the vertebral body. In the vertebral body, differences in vBMD were found to be more pronounced at the cortical bone than at the trabecular bone. In addition, differences in trabecular vBMD were more pronounced at the posterior part of the vertebral body.

An AUC map calculated using vBMD values computed at each voxel of the volumetric images of subjects included in the fracture and control groups is shown in **Figure 6.2**. Only AUC higher than the 90th percentile (AUC > 0.649) are shown. vBMD measurements show higher AUC in the posterior part of the vertebral body and at the endplates. Maximum local AUC (0.768) was observed in the superior articular processes of L1.

The anatomical distribution of the average differences in cortical sBMD between subjects included in fracture and control groups is showed in **Figure 6.3** (top). More pronounced differences (magenta color) were found at the posterior part of the vertebral body. **Figure 6.3** (bottom) shows the AUC map calculated using cortical sBMD at each vertex of the vertebral body surface. AUC higher than the 95th percentile (i.e. in the range 0.704-0.777) are circled in red.

6.4. Discussion

In the present study, we evaluated the association of DXA-derived measurements at L1-L4 segment with osteoporotic hip fractures by comparing women with transcervical hip fracture and age-matched controls.

Although no inclusion criteria related to height or weight was used to recruit the subjects, no significant differences between groups were found in terms of height, weight and BMI (Table VII). The current

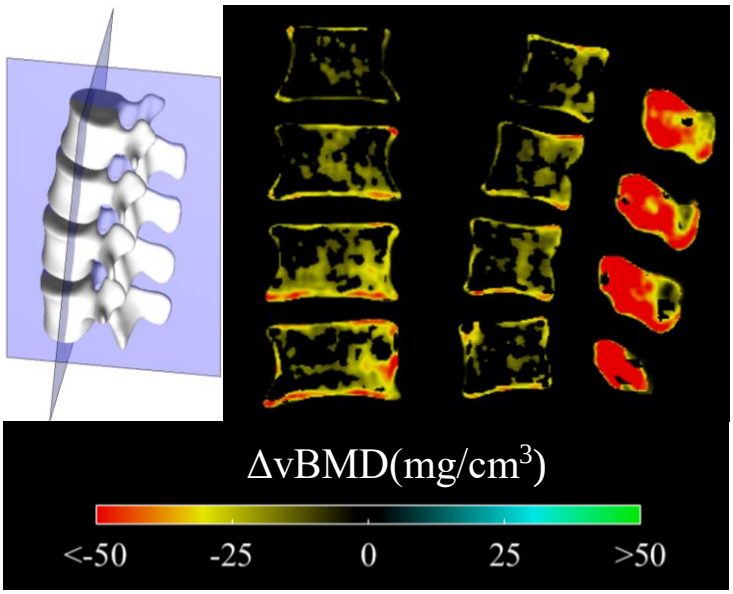

Figure 6.1: Anatomical distribution of the average differences in vBMD between subjects included the fracture group and controls.
Differences are shown in the mid-coronal plane (top centre) and mid-lateral plane (top right). Top left image indicates the cut planes. Red-yellow (respectively blue-green) colours indicate regions where ΔvBMD is on average lower (respectively higher) for hip fracture subjects compared to controls. Non-significant changes (unpaired two-sample t-test) are left in black.

study therefore compares two groups with similar age and anthropometric measures.

The OR associated with total femur aBMD (6.240 [3.145 – 12.381]) was three times the OR associated with lumbar spine aBMD (2.044 [1.343 – 3.112]) (Table VIII). Similar results were found in state-of-the-art studies evaluating the ability of aBMD measurements at different skeletal sites to predict osteoporotic fractures [38], [144]–[146]. Marshall *et al.* [38] observed that aBMD had higher predictive abilities when measured at spine for predicting vertebral fractures (Relative Risk [95% CI] of 2.3 [1.9 – 2.8]) and when measured at hip for hip fractures (2.6 [2.0 – 3.5]), compared to when measured at non- specific sites for any type of fracture (1.5 [1.4 – 1.6]), or when measured at lumbar spine for hip fracture (1.6 [1.2 to 2.2]).

In the current study, trabecular vBMD at the vertebral body showed a weak association with transcervical hip fracture (Table IX). This

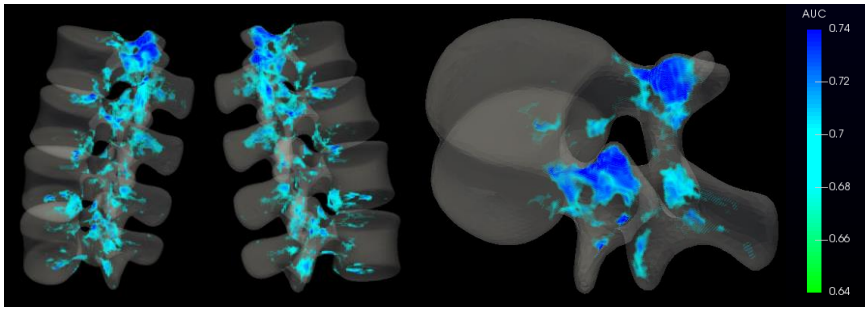

Figure 6.2: AUC map calculated using vBMD at each voxel of the volumetric images of subjects included in the fracture group and controls.
L1-L4 segment (left and middle) and L1 (right) are shown. Only AUC higher than the 90th percentile (i.e. AUC > 0.649) are shown. Maximum AUC was 0.768.

assertion is supported by findings reported in [148], [150], [152], where trabecular vBMD at lumbar spine were found to be mild or even no related with transcervical hip fractures. Moreover, studies suggested that trabecular bone measurements at lumbar spine were strongly associated with trochanteric fractures but weakly associated with transcervical ones [147], [150].

Higher AUC were found for DXA-derived 3D measurements at the cortical bone (cortical vBMD, thickness and sBMD) compared to measurements at the trabecular bone (trabecular vBMD) (Table IX). From these results, we can hypothesize that transcervical hip fractures could be associated with a more pronounced impairment at the cortical bone, compared to trabecular bone. To the best of our knowledge, our study is the first one to evaluate the association between osteoporotic hip fractures and 3D measurements at the cortical bone at the lumbar spine. Previously published studies evaluating the association between osteoporotic hip fractures and bone density measurements at the lumbar spine using QCT [125], [148], [150]–[152] focused on integral and/or trabecular vBMD assessment, mainly because analyzing the cortical bone requires to segment the thin cortical layer of the vertebral body which is, indeed, very challenging. The previous assertion, however, could be supported by findings obtained by Yang *et al.* [153] at the proximal femur. Their case-control study using QCT and including patients with transcervical hip fractures reported higher AUCs for cortical vBMD and apparent CTh at the proximal femur, compared to trabecular vBMD. Those findings are also consistent with biomechanical studies performed with human cadaver femurs that

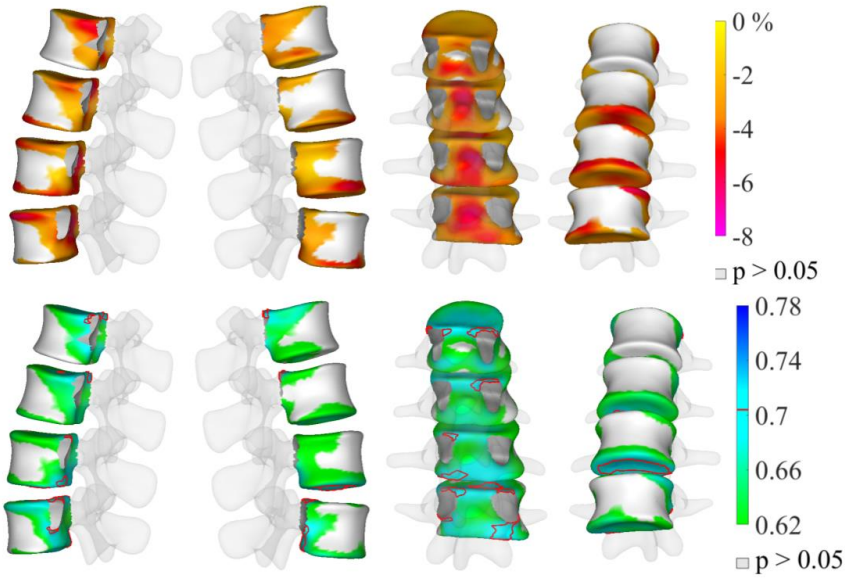

Figure 6.3: Cortical sBMD at the vertebral body.
Top: Anatomical distribution of the average differences in cortical sBMD at the vertebral body between subjects included in the fracture group (N =61) and control group (N =61). Non-significant changes (unpaired two-sample t-test) are left in grey. Bottom: AUC calculated using cortical sBMD at each vertex of the vertebral body surface of the subjects included in fracture and control groups. Regions where the differences in cortical sBMD were not significant (unpaired two-sample t-test) at the total vertebra region of interest are left in grey. Regions showing AUC higher than the 95th percentile (i.e. AUC > 0.704) are circled in red. Maximum AUC was 0.777.

showed the relatively small contribution of trabecular versus cortical bone in respect to bone strength in the femoral neck [154], [155].

To the best of our knowledge, our study is the first one to evaluate the association between transcervical hip fractures and vBMD of the posterior vertebral elements. We found a strong association between the integral vBMD of the posterior vertebral elements and transcervical hip fractures. The vertebral body is composed mainly by trabecular bone, and the posterior vertebral elements by cortical bone. This suggests, once again, a stronger association of the cortical bone density with transcervical hip fractures, compared to the trabecular bone density.

The strong association between transcervical hip fracture and cortical bone can also be seen in **Figure 6.1**, where local differences in vBMD

between subjects included in fracture groups and controls were shown to be more pronounced at the outer shell of the vertebral body and at the posterior vertebral elements, i.e. in regions that are mainly formed by cortical bone. This was confirmed by **Figure 6.2**, where vBMD measurements at each voxel showed locally high AUCs in the endplates, posterior part of the vertebral body, pedicles and articular processes. These regions were found in the literature to be associated with an abnormal load transmission as a result of intervertebral disc degeneration [156], [157]. These results are also consistent with studies that showed a strong association between CTh and endocortical trabecular vBMD (the average density in the trabecular compartment close to the cortex) at the femoral neck with transcervical hip fractures [158], [159]. The anatomical distribution of the average differences in cortical sBMD between subjects included in fracture and control groups showed more pronounced differences at the endplates and at the posterior surface of the vertebral body (**Figure 6.3**). This is consistent with state-of-the-art studies that showed that endplate and adjacent regions are the vertebral regions where tissue-level failure started, as measured in specimens using biomechanical testing [135], [140]–[142]. **Figure 6.1**, **Figure 6.2** and **Figure 6.3** suggest that endplates, posterior part of the vertebral body, pedicles and articular processes could be ROIs of importance in the assessment of transcervical hip fracture risk. Further analysis has to be done to investigate whether other type of hip fracture, such as trochanteric fracture, are associated with other specific patterns.

An important limitation of the present study is the small number of subjects that were included. In addition, only postmenopausal Caucasian women were included. Therefore, larger cohorts will be analyzed in future work, including men and other ethnicities. The DXA-based 3D modeling technique used in this study has the potential to be used in the context of very large, multicenter and prospective studies. One of the technical limitations of the present study is related to the segmentation of the cortex, which was only performed at the vertebral body. Therefore, DXA-derived 3D measurements at the posterior vertebral elements were only performed at the integral bone. However, as posterior vertebral elements are mainly formed by cortical bone, specific assessment of posterior vertebral elements cortical bone should provide similar results to those reported in the current study at integral bone. Another limitation is that participants included in this study did

not undergo QCT examination. Therefore, we could not perform a direct comparison between the results obtained using DXA-derived 3D measurements in our study with QCT-derived measurements. Lastly, in order to obtain a DXA-derived 3D measurement with the software (3D-SHAPER) that was used in our study, no vertebrae of the L1-L4 segment could be fractured or have severe osteoarthritis. Therefore, subjects included in our study had to meet stricter criteria, compared to other study using QCT where having at least two non-fractured lumbar vertebrae was enough to perform the analysis [125], [148]–[152]. The method could be adapted to exclude vertebrae with fracture and/or severe osteoarthritis and compute the 3D subject-specific shape and density model using the non-affected vertebrae.

6.5. Conclusion

The association of DXA-derived 3D measurements at lumbar spine with osteoporotic transcervical hip fractures in postmenopausal women was assessed in this case-control study. Integral vBMD at the posterior vertebral elements, CTh at the vertebral body and cortical sBMD at the vertebral body were the measurements at L1-L4 segment that best discriminated between fracture and control groups. The association of trabecular vBMD at the vertebral body with fracture was significantly lower, compared to measurements at the integral or cortical bone. These findings suggested that cortical bone measurements at lumbar spine had stronger association with transcervical hip fractures, compared to trabecular bone measurements. The DXA-derived 3D model proposed in this study offers an insightful assessment of the lumbar spine at different vertebral regions (vertebral body and posterior vertebral elements) and bone compartments (integral, trabecular and cortical), which could potentially improve osteoporosis assessment and fracture prevention, using standard lumbar spine AP DXA scans. Similar studies including large cohorts will be performed in future work to determine if DXA-derived 3D measurements at the lumbar spine could improve fracture risk prediction in clinical practice.

Chapter 7

7. CONCLUSION

7.1. Overview

The main objective of this thesis was the development and clinical evaluation of methods to analyze in 3D the bone shape and density of the lumbar spine, using 2D DXA images. The main motivation resided in providing automatic methods to offer an insightful 3D analysis of the lumbar spine, which could potentially improve osteoporosis and fracture risk assessment in patients who had a standard DXA scan of the lumbar spine without any additional examination. We next summarize the main concepts introduced in this thesis and highlight the strengths and limitations of the contributions presented in each chapter.

In **Chapter 4**, we developed a method for the construction of a statistical model encompassing shape, BMD, and pose variations of the lumbar spine using a training database of 90 QCT scans. Vertebral bones (from L1 to L4) were semi-automatically segmented in each QCT volume providing a surface mesh for each vertebra. Registration techniques were used to establish point-to-point correspondences between the surface meshes, and voxel-to-voxel correspondences between the QCT volumes. Statistical shape and BMD variations were computed in a global model of the L1-L4 segment. Subjects included in the model were adult men and women; with normal bone density, osteopenia and osteoporosis. However, the model did not included subjects with skeletal disease other than osteoporosis, such as severe osteoarthritis, severe scoliosis or abnormal bone growth and vertebral fracture. Moreover, the model was mainly designed to capture global variations, while very local variations (as bone spurs, or osteophytes) were not included.

We developed a method for the 3D subject-specific modeling of the lumbar spine from a single AP DXA image using the generated statistical model and a 3D-2D registration algorithm (**Chapter 4**). The 3D-2D registration algorithm used optimization methods searching for the pose, shape and density parameters of the statistical model that maximize the similarity between a simulated projection generated from the model and the DXA image. The use of a single AP DXA image makes the method fully compatible with current clinical practices. The accuracy of the method was evaluated by comparing DXA-derived with QCT-derived 3D subject-specific models. The validation was performed with 180 AP DXA images from two different manufacturers. Subjects included in the validation were adult men and

women; with normal bone density, osteopenia and osteoporosis. As the subjects were not in the same position in the two modalities (DXA and CT), registration methods were used to align them. The shape accuracy was 1.51 mm at the total vertebra and 0.66 mm at the vertebral body. The main drawback of the 3D modelling method is that it could hardly model local deformities (e.g. osteophytes), which are often not seen in the AP DXA scans and were not included in the statistical model.

We developed a model-based algorithm to segment the periosteal and endocortical surfaces of the cortical layer at the vertebrae (**Chapter 4**). Model-based techniques have been shown to be more accurate than thresholding techniques when estimating thin cortices, as the vertebral body cortex. Modeling the outer and inner surfaces of the cortical shell was only performed in the vertebral body. The complex geometry of the back processes makes the segmentation of the cortical bone in this region of interest particularly challenging.

We developed a method to provide clinical measurements at different vertebral regions (vertebral body and posterior vertebral elements) and bone compartments (integral, trabecular and cortical) using the 3D subject-specific model of the lumbar spine (**Chapter 4**). We validated the accuracy of the clinical measurements by comparing DXA-derived with QCT-derived 3D subject-specific shape and density measurements (**Chapter 4**). The accuracy of the measurements was evaluated by comparing the validation set of 180 subjects. Correlation coefficients between DXA and QCT-derived measurements ranged from 0.81 to 0.97. The method proposed, integrated into the 3D-Shaper® software, is fully automated and compatible with current clinical practices.

In **Chapters 5**, we evaluated the association of DXA-derived 3D measurements at lumbar spine assessed with osteoporosis-related vertebral fractures. We performed a retrospective case-control study including 37 postmenopausal Caucasian women who experienced a vertebral fracture event (at 3.2 $\pm$ 2.4 years from baseline) and 37 age-matched controls. The ability of DXA-derived 3D measurements to discriminate between fracture and control groups was assessed at baseline using the DXA-based 3D modeling methods developed in **Chapter 4**. Trabecular vBMD was the measurement that best discriminated between fracture and control groups, with an AUC of 0.733, against 0.682 for aBMD. As the fracture group included various types of vertebral fractures, subgroup analyses were also performed to

analyze the difference between groups depending on the type of fracture. Overall, similar findings were observed within the subgroup analyses. The L1 vertebral fractures subgroup had the highest AUC at trabecular vBMD (0.827), against aBMD (0.758).

Finally, in **Chapters 6,** we evaluated the association of DXA-derived 3D measurements at lumbar spine with osteoporosis-related hip fractures. We analyzed a case-control database composed by 61 women with transcervical hip fractures and 61 age-matched women without any type of fracture using the DXA-based 3D modeling methods developed in **Chapter 4**. Integral vBMD, and cortical vBMD, sBMD and thickness were the DXA-derived 3D measurements at lumbar spine that best discriminated between fracture and control groups, with AUC's in the range of 0.685-0.726, against 0.670 for aBMD. The highest AUC (0.726) and OR (2.610) were found for integral vBMD at the posterior vertebral elements. Significantly lower AUC (0.617) and OR (1.607) were found for trabecular vBMD at the vertebral body. These findings suggested that cortical bone measurements at lumbar spine had stronger association with transcervical hip fractures, compared to trabecular bone measurements.

Further studies including larger cohorts should be performed to confirm the results presented in **Chapters 5 and 6** and determine if DXA-derived 3D measurements at the lumbar spine could improve fracture risk prediction in clinical practice.

7.2. Outlook and future work

The work carried out in this thesis constitutes a first step towards a new technique which could potentially improve osteoporosis and fracture risk management. For this new technique to be widely used in the daily clinical practice, some improvements of the presented work are required, as described in the following section.

Precision study

To monitor treatment- and age-related changes using the DXA-derived 3D measurements, precision studies should be performed to derive the least significant change associated with each measurement [160]. Least significant change supports clinicians in the interpretation of the measured change, indicating if the changes calculated are meaningful and clinically relevant. Humbert *et al.* [161] assessed, for the first time,

the precision of 3D modeling techniques of the proximal femur from DXA scans. Subjects included in their precision study were scanned twice, with repositioning for duplicate hip scans. A similar study should be performed in future work to assess the least significant changes of measurements provided by the 3D modeling method of the lumbar spine developed in this thesis.

Age-related reference ranges

The T-score is the recommended measurement for diagnosing osteoporosis disease in postmenopausal women and men over 50 years. T-score indicates how the individual aBMD deviates from reference measurements obtained in a healthy young adult population. Z-score indicates how the individual aBMD deviates from reference measurements obtained in a population of similar age. Reference measurements from different populations can be used. Therefore, as future work, age-related reference ranges will be established in order to use the DXA-derived 3D measurements obtained by the 3D modelling methods osteoporosis diagnosis and patient monitoring.

Software integration

3D-Shaper® software, developed by *Galgo* Medical, is currently the only technology in the market that provides 3D subject-specific analysis of bony structures from a standard DXA image (**Figure 1.1**). 3D-Shaper® provides additional information about the 3D geometry and bone mineral distribution of the proximal femur that can be used to improve osteoporosis management. Some of the features are: automated workflow, retrospective data analysis, follow-up and automated report generation. In the Industrial Doctorate in which this thesis was developed, we further developed the algorithm integrated into 3D-Shaper® for the femur to include the lumbar spine, providing an automated workflow that analyzes the 3D bony structure of the lumbar spine in 3D from an AP DXA scan. However, to provide an insightful 3D analysis of the lumbar spine, which could be widely used in the daily clinical practice to improve osteoporosis and fracture risk assessment, age-related reference ranges and least significant change of measurements have to be integrated. As future work, these improvements of the presented work will be integrated into the 3D-Shaper® software.

Treatment

Trabecular and cortical bone can respond differently to drug treatments, which cannot be monitored using standard DXA exams. Winzenrieth *et al.* [23] evaluated the ability of 3D modeling methods to monitor osteoporosis drug effect on the cortical and trabecular bone at the proximal femur. We performed a preliminary study to assess changes in trabecular and cortical vBMD and CTh in L1-L4 vertebral bodies using a cohort of patients treated with Denosumab (Dmab). We retrospectively analyzed a cohort of 18 patients treated with Dmab and 33 controls naïve of treatment. Spine AP DXA scans were acquired at baseline and 24 months. Integral, trabecular and cortical vBMD as well as CTh were assessed using the DXA-based 3D modeling software developed in this thesis. Changes from baseline were analyzed using paired t-tests and differences between naïve and Dmab groups were analyzed using unpaired t-tests. As expected, no changes have been observed in the naïve group after 24 months of follow-up, while significant increases in density were observed in both the cortical and trabecular compartments in patients treated with Dmab. DXA-based 3D measurement of the cortical and trabecular bone could potentially improve the monitoring of patient under pharmacological treatment for osteoporosis. Further studies including larger cohorts and other osteoporosis drug treatments should be performed to confirm these promising results.

Osteoarthritis

The presence of osteoarthritis at the lumbar spine can lead to a wrong diagnosis of the osteoporosis diseased, since local accumulation of bone mineral at the periosteal surface might lead to an overestimation of the aBMD computed by DXA, and hence, to a higher T-score [117]. Guglielmi *et al.* [134] evaluated the impact of degenerative changes at the spine on DXA- and QCT-derived BMD. They observed that degenerative changes influence DXA-derived aBMD and cortical and integral QCT-derived vBMD. However, they found no evidence supporting that degenerative changes influence trabecular QCT-derived vBMD. As future work, the association of DXA-derived 3D measurements introduced in this thesis with degenerative changes due to osteoarthritis at the lumbar spine could be studied. The trabecular vBMD at the vertebral body could provide an insightful measurement, by discarding the posterior vertebral elements and local deformations at the periosteal surface due to osteoarthritis that bias aBMD

measurements.

Secondary osteoporosis

Secondary osteoporosis is defined as osteoporosis that develops because of an unrelated underlying cause, including drug treatment (chronic corticosteroid use) or other pathologies as: genetic, endocrine, gastrointestinal, hematologic, rheumatologic, nutritional, pharmacological diseases, or a combination of them. The resulting increase in fracture risk is presumed to be mediated by low aBMD. Some exceptions, such as glucocorticoid exposure, rheumatoid arthritis and diabetes mellitus, have been identified as clinical risk independent of low aBMD [35], [162], [163]. However, DXA examination measures the aBMD of the integral bone, which induces a lack of sensitivity to monitor changes caused by these pathologies. Trabecular and cortical bone can also react differently to those diseases, such as under glucocorticoids where the trabecular bone is impaired before the cortical bone [162]. As future work, it would be interesting to assess changes in the DXA-derived 3D measurements at the lumbar spine associated with secondary osteoporosis.

Vertebral fracture assessment

Vertebral fracture is the most common osteoporosis-related fracture. However, only one-third of vertebral fractures get clinical attention [119]; yet, their presence is associated with an increased morbidity and mortality, a substantial increased risk for subsequent fractures (independent of BMD) and may alter the choice of pharmacotherapy. Conventional radiography was the primary modality used to identify vertebral fractures. De Bruijne *et al.* [164] proposed a method for vertebral fracture quantification from X-ray images using neighbor-conditional shape models. Lately, lateral spine imaging with densitometric Vertebral Fracture Assessment (VFA) is used in clinical practices to evaluate the presence of vertebral fractures. Densitometric VFA images can be obtained at the same time as BMD measurement at lower cost and radiation exposure than standard radiography images of the spine. VFA images also avoids the projection parallax effects of radiographs. However, standard spine radiography images are less noisy and have higher spatial resolution than VFA images. There are different methods for diagnosing vertebral fractures with VFA. The ISCD endorses the Genant semi-quantitative method as the clinical technique of choice to this end [22]. Roberts *et al.* [165] presented a semi-automatic

determination of detailed vertebral shape from lateral DXA-based images using active appearance models. Although the accuracy in general is good, its performance is deteriorated when increasing the fracture grade. As future work, it would be interesting to develop and validate a method to assess vertebral fractures based on the statistical model developed in this thesis. A method for vertebral fracture quantification, similar than proposed by Bruijne *et al.* [164] but using DXA images, could be implemented. The fractured vertebra(s) would be hidden in the 2D mask to be used in the registration process. The L1-L4 model would be registered as described in Section 4.2.3. The excluded region of interest (for example L3) would be statistically estimated based on the regions included (L1-L2-L4). The difference between the true shape (obtained by the lateral DXA) and the estimated normal shape (obtained by the 3D modeling method) would be used as a measure of abnormality.

Complex anatomical structures modeling

In the present thesis, 3D statistical variations of shape and BMD were computed in a global model of the L1-L4 segment. As vertebrae are modelled together, not only shape and bone density are included in the model but also spatial relationships between neighbor vertebrae. Using a global statistical model of the lumbar spine instead one model for each vertebra increases specificity and avoid unlikely shapes and vertebrae overlapping. However, the generality could be impaired.

Multi-organ approaches, unlike traditional organ-specific strategies, incorporate inter-organ relations into the model, thus leading to a more accurate representation of the complex human anatomy. In order to generate a specific but also generic model of the lumbar spine, a multi-object statistical model could be developed in future work. Methodological framework for building accurate multi-object statistical shape models that incorporate both the relationships between objects and particularities of each object individually could be developed.

During this thesis a thorough review of the state-of-the-art on multi-organ analysis in medical imaging, with more than 300 papers reviewed, discussed, and categorized methodologically and anatomically, has been performed, and is currently under revision in Medical Image Analysis (Publications: 4). This review proposes, for the first time, a methodology-based classification of the different techniques available

for the analysis of multi-organ anatomical complex, from the simple global modelling, to the more sophisticated sequential and multi-resolution techniques. The different methodologies for multi-organ analysis are classified using the following categorization: global and individual models, coupled deformable models, multi-level models, sequential models, atlas-based models, machine-learning models, graphical models, and articulated models. The manuscript also reflects on the trends and challenges of multi-organ analysis, the peculiarities of each anatomical region, and its impact on the future of healthcare.

In the context of the 3D subject-specific modelling method of the spine introduced in this thesis, some ideas for further developments include: decomposing lumbar spine in patches and applying a multi-level statistical shape model to them, extending it looking for shape constraints between structures in hierarchical shape decomposition due to their proximity or connectivity, embedding pose priors into the statistical models for articulated models (i.e. include polar coordinates in the multi-level approach), incorporating texture models in the existing multi-object statistical method, analyzing alternative dimension reduction methods in the multi-object environment, and extending the matrix notation of the multi-level method relying on wavelet decomposition by introducing the multi-resolution analysis of surfaces with arbitrary topology. The 3D-2D registration method will also have to be adapted to include the multi-object statistical model.

Fracture risk estimation using finite element modeling

Finite element modeling simulates mechanical testing and assesses the response of bones to external forces. The effect of forces associated with low impact trauma can be simulated, and the risk of fracture estimated. In the literature, QCT-based finite element analysis is used to assess mechanical strength of the vertebrae and predict fracture risk [129]–[132]. As future work, we will explore the possibility to perform the finite element analysis from the 3D subject-specific shape and BMD model of the lumbar spine to evaluate for fracture risk assessment.

In summary, the methods developed throughout this thesis offers an insightful 3D analysis of the lumbar spine at different vertebral regions and bone compartments from clinical practice imaging modality. Future work presented above must be addressed for these new methods to be widely used in the daily clinical practice. Nonetheless, we believe that this thesis has presented key contributions towards the future development of new advanced tools for osteoporosis and fracture risk assessment.

APPENDICES

A. Segmentation

A semi-automated method was used to segment the vertebrae in the QCT volumes. The segmentation process is briefly described in this appendix. The same process was used to semi-automatically segment all the QCT scans, i.e. the 90 QCT scans used to generate the model (training set) and the 180 QCT scans used to validate the method (validation set).

DICOM images from QCT scans were converted in volumetric images (i.e. 3-dimensional matrices where each element is a sampled density) and calibrated using the Mindways phantom. The calibration process was performed for each L1-L4 segment, following the protocol recommended by the manufacturer.

A series of filters were applied to the QCT DICOM images to enhance the contrast in the facet joints region of interest [112], thereby helping the segmentation of each vertebra. These filters are:

1. An opening filter to dark small groups of bright voxels at vertebral joint space.

$$\boldsymbol{A'} = \boldsymbol{A} \circ \boldsymbol{B} = (\boldsymbol{A} \ominus \boldsymbol{B}) \oplus \boldsymbol{B}$$

2. A top-hat filter to highlight the brightest areas (vertebral bone).

$$\boldsymbol{A_{TH}} = \boldsymbol{A'} - ((\boldsymbol{A'} \ominus \boldsymbol{B}) \oplus \boldsymbol{B'}$$

3. A bottom-hat filter to highlight the darkest areas (facet joints).

$$\boldsymbol{A_{BH}} = (\boldsymbol{A'} \oplus \boldsymbol{B}) \ominus \boldsymbol{B}) - \boldsymbol{A'}$$

4. Finally, the top-hat filtered volume $\boldsymbol{A_{TH}}$ is added, and the bottom-hat filtered $\boldsymbol{A_{BH}}$ is subtracted to the QCT volume $\boldsymbol{A'}$.

where $\boldsymbol{A}(x, y, z)$ is the QCT volume, $\boldsymbol{B}(u, v, w)$ a ball-shaped structural element, and erosion and dilatation operations:

$$\mathbf{A} \ominus \mathbf{B} = \min_{u,v,w} \{\boldsymbol{A}(x+u, y+v, z+w) - \boldsymbol{B}(u,v,w)\}$$

$$\mathbf{A} \oplus \mathbf{B} = \max_{u,v,w} \{\boldsymbol{A}(x-u, y-v, z-w) + \boldsymbol{B}(u,v,w)\}$$

Examples of images obtained as a result of each filter are show in **Figure A. 1:**. The QCT volumes before and after filtering are shown for the three subjects selected as examples for each group **Figure A. 2,** showing enhanced contrast in the facet joints region of interest.

Vertebrae were semi-automatically segmented in the pre-processed QCT volumes using the software TurtleSeg [113], [114], which implements the following process. The vertebral contours are manually identified in a set of non-parallel slices. The software automatically interpolates the contours to form a 3D segmentation, resulting in a volumetric mask for each vertebra. If the results are not satisfactory, additional contours are identified and the interpolation is repeated. Local deformities, such as spurs, were manually segmented by painting and erasing techniques. The segmentation process was performed for each vertebra, and for the 90 subjects in the training set. The segmentation process took between forty minutes and two hours to segment each vertebra of the L1-L4 segment, depending on the image quality and the presence of local deformities of the vertebrae.

The segmentation process resulted in a 3D binary mask for each vertebra. The binary masks were smoothed using a Gaussian filter.

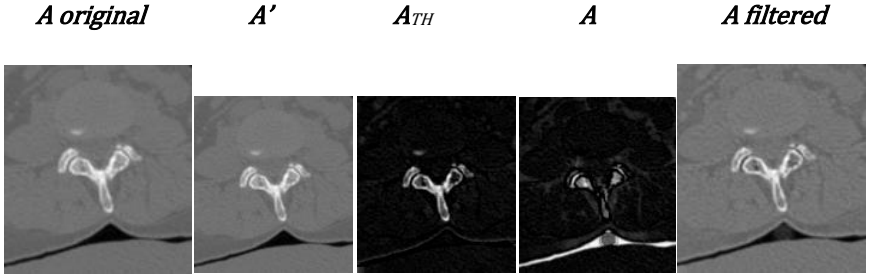

Figure A. 1: Pre-processing filters pipeline.
A' is the resulting image after applying the 3D opening filter to ***A*** (the original calibrated QCT image). $\boldsymbol{A_{TH}}$ is the image after applying the top-hap filter (brightest areas highlighted) to ***A'***. $\boldsymbol{A_{BH}}$ is the image after applying the bottom-hat filter (darkest areas highlighted) to ***A'***. Finally, ***A filtered*** is obtained by adding to ***A'*** the $\boldsymbol{A_{TH}}$ filtered volume and subtracting the $\boldsymbol{A_{BH}}$ filtered volume.

Surface mesh were obtained using the marching cubes algorithm. Surface meshes generated before and after smoothing (**Figure A. 3**) show the effect of smoothing.

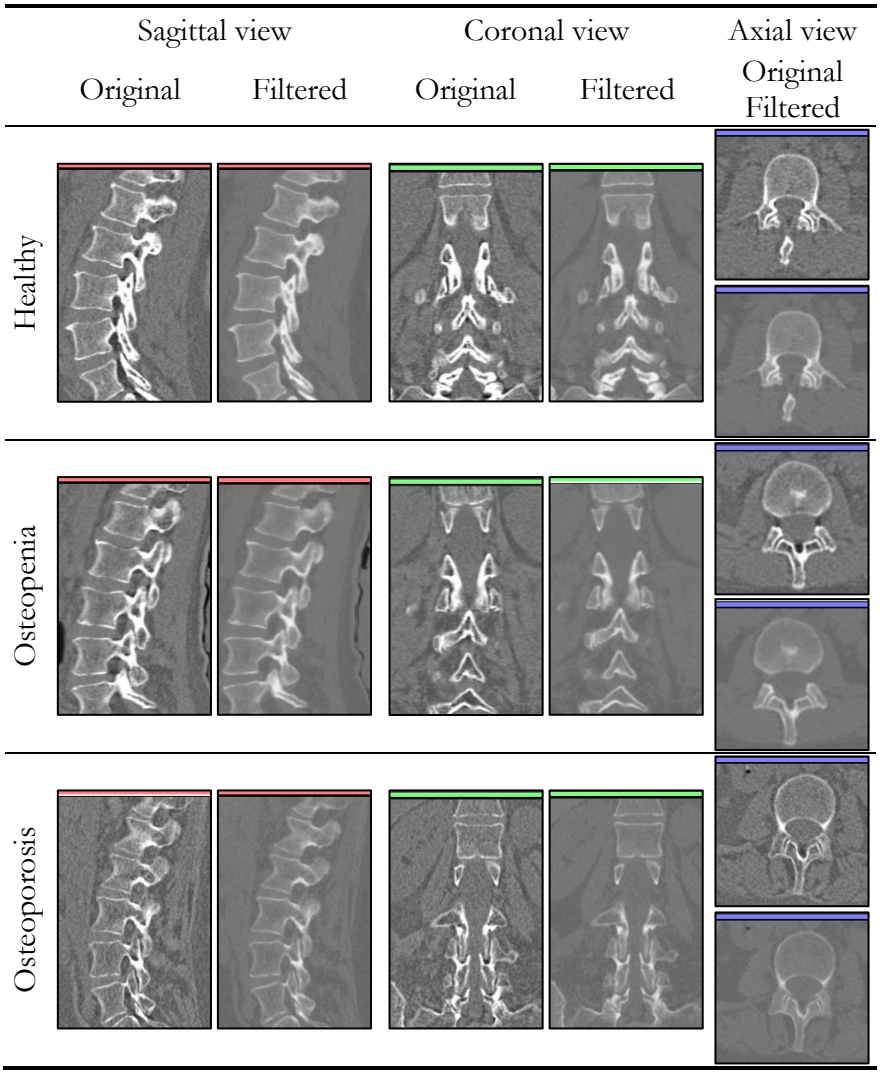

Figure A. 2: Comparison of QCT volumes before and after pre-processing filters for the three subjects selected as examples.

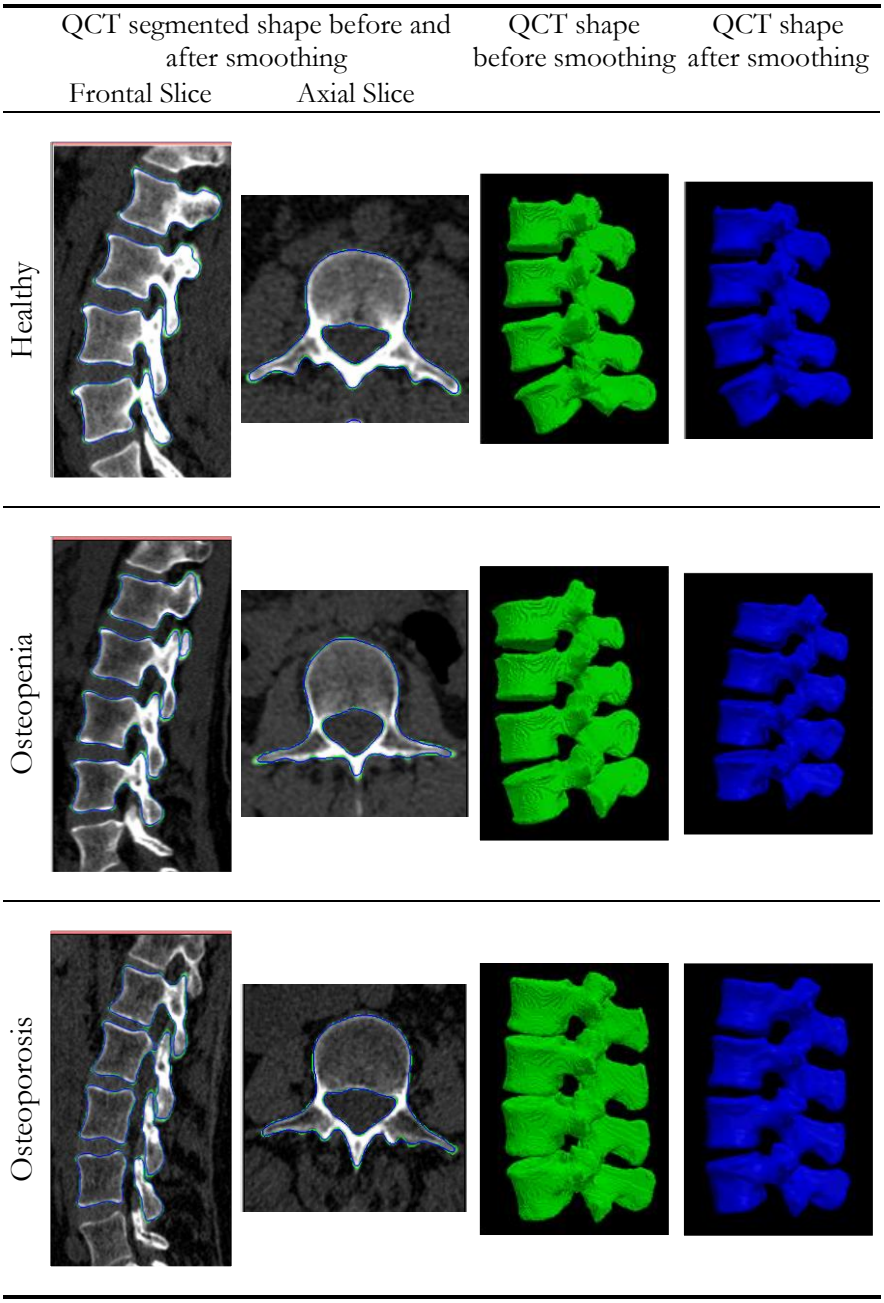

Figure A. 3: Segmented QCT volumes before and after smoothing for the three subjects selected as examples.

B. Clinical measurements

Table X. DXA and QCT-derived clinical measurements at L1, L2, L3, L4 and L1-L4 segment.
Values (mean ± standard deviation) and differences (mean ± standard deviation) between DXA-derived and QCT-derived clinical measurements: Values and correlation coefficients R are provided for the total vertebra ("Total") and vertebral bodies ("Body").

				ALL (N = 180 study subjects)				GE (N = 90)		DMS (N = 90)	
				QCT	DXA	Difference (DXA - QCT)		Difference (DXA - QCT)		Difference (DXA - QCT)	
				Mean ± SD	Mean ± SD	Mean ± SD	R**	Mean ± SD	R**	Mean ± SD	R**
vBMD (mg/cm³)	Integral	Total	L1	274.73 ± 52.95	288.00 ± 55.89	13.27 ± 24.90	0.90	19.84 ± 25.18	0.88	6.70 ± 22.93	0.92
			L2	283.45 ± 55.30	281.08 ± 56.86	-2.37 ± 24.54	0.90	4.71 ± 24.61	0.90	-9.45 ± 22.46	0.92
			L3	283.03 ± 56.68	284.03 ± 57.21	1.00 ± 25.42	0.90	8.59 ± 23.78	0.91	-6.59 ± 24.85	0.91
			L4	298.16 ± 59.89	303.90 ± 63.21	5.74 ± 25.49	0.92	10.75 ± 25.95	0.91	0.73 ± 24.14	0.93
			L1-L4	281.65 ± 55.38	286.28 ± 57.31	4.63 ± 23.82	0.91	11.32 ± 23.73	0.91	-2.05 ± 22.08	0.93
		Body	L1	208.55 ± 43.11	233.27 ± 42.92	24.72 ± 26.01*	0.82	25.76 ± 27.03*	0.77	23.68 ± 25.06*	0.85
			L2	212.77 ± 44.81	213.64 ± 42.53	0.88 ± 24.90	0.84	3.06 ± 25.04	0.82	-1.31 ± 24.70	0.86
			L3	212.26 ± 46.04	213.46 ± 42.54	1.20 ± 24.27	0.85	3.65 ± 24.02	0.84	-1.25 ± 24.41	0.87
			L4	216.46 ± 48.27	217.62 ± 47.18	1.16 ± 27.04	0.84	2.10 ± 28.58	0.82	0.22 ± 25.53	0.86
			L1-L4	212.61 ± 44.88	219.16 ± 43.32	6.55 ± 23.84	0.85	8.23 ± 24.36	0.83	4.87 ± 23.33	0.87
	Trabecular	Body	L1	148.13 ± 38.88	174.71 ± 38.94	26.58 ± 24.98*	0.79	27.07 ± 25.39*	0.75	26.08 ± 24.69*	0.83
			L2	150.06 ± 39.87	156.63 ± 37.88	6.57 ± 23.67	0.82	8.21 ± 23.32	0.80	4.93 ± 24.03	0.83
			L3	149.43 ± 41.18	157.07 ± 38.24	7.64 ± 23.33	0.83	8.82 ± 22.84	0.81	6.46 ± 23.88	0.84
			L4	153.46 ± 43.04	159.23 ± 41.88	5.76 ± 25.55	0.82	5.97 ± 26.31	0.80	5.56 ± 24.92	0.84
			L1-L4	150.32 ± 40.35	161.57 ± 38.85	11.25 ± 23.31*	0.83	12.12 ± 23.30	0.81	10.37 ± 23.43	0.85
	Cortical	Body	L1	595.57 ± 45.47	617.64 ± 39.94	22.07 ± 28.77*	0.78	23.34 ± 30.26*	0.75	20.79 ± 27.31*	0.81
			L2	610.81 ± 47.78	603.70 ± 42.20	-7.11 ± 28.92	0.80	-5.48 ± 31.21	0.77	-8.73 ± 26.51	0.83
			L3	616.59 ± 49.57	603.59 ± 41.54	-13.00 ± 28.84*	0.81	-11.10 ± 31.28	0.79	-14.90 ± 26.21	0.84
			L4	618.61 ± 50.43	616.22 ± 45.16	-2.39 ± 33.10	0.77	-1.10 ± 35.26	0.75	-3.67 ± 30.94	0.78
			L1-L4	611.18 ± 46.26	610.43 ± 40.77	-0.74 ± 25.14	0.84	0.82 ± 26.82	0.82	-2.30 ± 23.38	0.86

Table X.b

				ALL (N = 180 study subjects)				GE (N = 90)		DMS (N = 90)	
				QCT	DXA	Difference (DXA - QCT)		Difference (DXA - QCT)		Difference (DXA - QCT)	
				Mean ± SD	Mean ± SD	Mean ± SD	R**	Mean ± SD	R**	Mean ± SD	R**
BMC (g)	Integral	Total	L1	11.27 ± 3.02	11.95 ± 3.25	0.68 ± 1.13	0.94	0.92 ± 1.26	0.93	0.44 ± 0.95	0.95
			L2	12.73 ± 3.40	12.57 ± 3.46	-0.15 ± 1.08	0.95	0.16 ± 1.13	0.95	-0.46 ± 0.93	0.96
			L3	14.03 ± 3.79	13.90 ± 3.70	-0.14 ± 1.14	0.95	0.13 ± 1.09	0.96	-0.40 ± 1.13	0.96
			L4	14.84 ± 4.01	14.79 ± 4.12	-0.05 ± 1.35	0.95	0.08 ± 1.43	0.95	-0.18 ± 1.26	0.95
			L1-L4	51.97 ± 13.90	52.46 ± 14.28	0.49 ± 4.29	0.95	1.49 ± 4.57	0.95	-0.51 ± 3.77	0.96
		Body	L1	5.46 ± 1.55	6.34 ± 1.70	0.88 ± 0.75*	0.90	0.88 ± 0.84*	0.88	0.88 ± 0.66*	0.92
			L2	5.98 ± 1.65	6.16 ± 1.70	0.18 ± 0.72	0.91	0.24 ± 0.76	0.90	0.12 ± 0.66	0.92
			L3	6.45 ± 1.82	6.57 ± 1.74	0.12 ± 0.71	0.92	0.14 ± 0.70	0.93	0.09 ± 0.72	0.92
			L4	6.72 ± 1.87	6.79 ± 1.93	0.07 ± 0.90	0.89	0.05 ± 0.98	0.88	0.09 ± 0.81	0.90
			L1-L4	24.62 ± 6.79	25.86 ± 6.99	1.25 ± 2.82	0.92	1.31 ± 3.03	0.91	1.18 ± 2.61	0.93
	Trabecular	Body	L1	3.36 ± 1.10	4.12 ± 1.21	0.76 ± 0.63*	0.85	0.75 ± 0.69*	0.83	0.78 ± 0.58*	0.88
			L2	3.65 ± 1.15	3.94 ± 1.20	0.30 ± 0.62	0.86	0.33 ± 0.65	0.85	0.26 ± 0.58	0.88
			L3	3.92 ± 1.26	4.22 ± 1.24	0.29 ± 0.62	0.88	0.28 ± 0.62	0.88	0.30 ± 0.62	0.88
			L4	4.11 ± 1.28	4.33 ± 1.35	0.22 ± 0.75	0.84	0.18 ± 0.81	0.83	0.25 ± 0.69	0.86
			L1-L4	15.04 ± 4.75	16.61 ± 4.95	1.56 ± 2.49*	0.87	1.54 ± 2.65	0.86	1.59 ± 2.35*	0.88
	Cortical	Body	L1	2.10 ± 0.52	2.22 ± 0.53	0.12 ± 0.26	0.88	0.13 ± 0.29	0.86	0.10 ± 0.23	0.89
			L2	2.34 ± 0.57	2.22 ± 0.54	-0.11 ± 0.25	0.90	-0.09 ± 0.26	0.90	-0.14 ± 0.24	0.90
			L3	2.53 ± 0.64	2.35 ± 0.55	-0.18 ± 0.26*	0.91	-0.14 ± 0.27	0.92	-0.22 ± 0.25	0.91
			L4	2.61 ± 0.67	2.47 ± 0.61	-0.15 ± 0.31	0.89	-0.14 ± 0.33	0.88	-0.16 ± 0.28	0.89
			L1-L4	9.58 ± 2.34	9.26 ± 2.20	-0.32 ± 0.88	0.93	-0.23 ± 0.92	0.93	-0.41 ± 0.84	0.93

Table X.c

				ALL (N = 180 study subjects)				GE (N = 90)		DMS (N = 90)	
				QCT	DXA	Difference (DXA - QCT)		Difference (DXA - QCT)		Difference (DXA - QCT)	
				Mean ± SD	Mean ± SD	Mean ± SD	R**	Mean ± SD	R**	Mean ± SD	R**
Volume (cm³)	Integral	Total	L1	41.14 ± 8.06	41.57 ± 7.98	0.42 ± 2.64	0.95	0.28 ± 2.65	0.94	0.56 ± 2.64	0.95
			L2	44.96 ± 8.45	44.80 ± 8.44	-0.16 ± 2.61	0.95	-0.22 ± 2.75	0.95	-0.10 ± 2.49	0.96
			L3	49.66 ± 9.23	49.03 ± 8.84	-0.63 ± 2.72	0.96	-1.01 ± 2.78	0.95	-0.25 ± 2.61	0.96
			L4	49.82 ± 9.07	48.69 ± 8.75	-1.13 ± 2.92	0.95	-1.55 ± 2.90	0.94	-0.70 ± 2.89	0.95
			L1-L4	184.80 ± 34.37	183.49 ± 33.78	-1.31 ± 9.33	0.96	-2.24 ± 9.65	0.96	-0.38 ± 8.95	0.97
		Body	L1	26.30 ± 5.44	27.23 ± 5.33	0.93 ± 1.96	0.93	0.78 ± 1.95	0.93	1.09 ± 1.96	0.94
			L2	28.23 ± 5.54	28.86 ± 5.48	0.64 ± 1.82	0.95	0.58 ± 1.87	0.94	0.69 ± 1.78	0.95
			L3	30.48 ± 5.83	30.81 ± 5.60	0.34 ± 1.77	0.95	0.11 ± 1.69	0.95	0.56 ± 1.84	0.96
			L4	31.17 ± 5.87	31.23 ± 5.62	0.06 ± 1.99	0.94	-0.17 ± 1.94	0.94	0.29 ± 2.02	0.95
			L1-L4	116.17 ± 22.42	118.14 ± 21.83	1.97 ± 6.56	0.96	1.31 ± 6.48	0.96	2.63 ± 6.61	0.96
	Trabecular	Body	L1	22.79 ± 4.92	23.66 ± 4.76	0.87 ± 1.85	0.93	0.70 ± 1.84	0.93	1.04 ± 1.85	0.93
			L2	24.43 ± 5.00	25.21 ± 4.91	0.78 ± 1.77	0.94	0.69 ± 1.81	0.93	0.87 ± 1.74	0.94
			L3	26.42 ± 5.23	26.95 ± 5.03	0.53 ± 1.75	0.94	0.26 ± 1.65	0.94	0.81 ± 1.80	0.95
			L4	26.98 ± 5.23	27.26 ± 5.03	0.28 ± 1.91	0.93	0.05 ± 1.86	0.93	0.52 ± 1.93	0.94
			L1-L4	100.62 ± 20.12	103.08 ± 19.55	2.46 ± 6.34	0.95	1.69 ± 6.24	0.95	3.23 ± 6.39	0.95
	Cortical	Body	L1	3.50 ± 0.67	3.57 ± 0.68	0.07 ± 0.33	0.88	0.08 ± 0.36	0.87	0.06 ± 0.30	0.90
			L2	3.80 ± 0.72	3.65 ± 0.70	-0.14 ± 0.30	0.91	-0.11 ± 0.31	0.91	-0.18 ± 0.29	0.91
			L3	4.06 ± 0.77	3.86 ± 0.71	-0.20 ± 0.29	0.93	-0.14 ± 0.27	0.94	-0.25 ± 0.29	0.93
			L4	4.19 ± 0.84	3.97 ± 0.76	-0.22 ± 0.38*	0.89	-0.21 ± 0.42	0.88	-0.23 ± 0.33	0.91
			L1-L4	15.55 ± 2.92	15.05 ± 2.81	-0.49 ± 1.04	0.93	-0.38 ± 1.09	0.93	-0.60 ± 0.99	0.94
CTh (mm)	Cortical	Body	L1	0.69 ± 0.08	0.71 ± 0.08	0.01 ± 0.06	0.73	0.02 ± 0.06	0.67	0.01 ± 0.05	0.79
			L2	0.72 ± 0.08	0.69 ± 0.08	-0.03 ± 0.05*	0.80	-0.02 ± 0.05	0.79	-0.04 ± 0.05*	0.82
			L3	0.73 ± 0.08	0.70 ± 0.08	-0.03 ± 0.05*	0.81	-0.02 ± 0.05	0.81	-0.04 ± 0.05*	0.83
			L4	0.75 ± 0.09	0.73 ± 0.09	-0.02 ± 0.06	0.79	-0.01 ± 0.06	0.77	-0.03 ± 0.05	0.82
			L1-L4	0.72 ± 0.08	0.71 ± 0.08	-0.02 ± 0.05	0.83	-0.01 ± 0.05	0.82	-0.03 ± 0.04	0.86

REFERENCES

[1] Consensus Development Conference, "Diagnosis, prophylaxis, and treatment of osteoporosis," *Am. J. Med.*, vol. 90, no. June, pp. 107–110, 1991.

[2] J. A. Kanis and WHO Scientific Group, "Assesment of osteoporosis at the primary health care level. Technical report.," 2007.

[3] L. J. Melton, E. A. Chrischilles, C. Cooper, A. W. Lane, and B. L. Riggs, "Perspective. How many women have osteoporosis?," *J. Bone Miner. Res.*, vol. 7, no. 9, pp. 1005–1010, 1992.

[4] L. J. Melton, E. J. Atkinson, M. K. O'Connor, W. M. O'Fallon, and B. L. Riggs, "Bone Density and Fracture Risk in Men," *J. Bone Miner. Res.*, vol. 13, no. 12, pp. 1915–1923, 1998.

[5] T. F. Cootes, C. J. Taylor, D. H. Cooper, and J. Graham, "Training models of shape from sets of examples," in *British Machine Vision Conference*, 1992, pp. 9–18.

[6] T. F. Cootes and C. J. Taylor, "Active Shape Models - 'Smart Snakes,'" in *British Machine Vision Conference*, 1992, no. 3, pp. 266–275.

[7] T. F. Cootes, C. J. Taylor, A. Lanitis, D. H. Cooper, and J. Graham, "Building and using flexible models incorporating grey-level information," in *International Conference on Computer Vision*, 1993, vol. 4, pp. 242–246.

[8] T. Cootes, A. Hill, C. Taylor, and J. Haslam, "Use of active shape models for locating structures in medical images," *Image Vis. Comput.*, vol. 12, no. 6, pp. 355–365, 1994.

[9] T. F. Cootes, C. J. Taylor, D. H. Cooper, and J. Graham, "Active Shape Models - Their Training and Application," *Comput. Vis. Image Underst.*, vol. 61, no. 1, pp. 38–59, Jan. 1995.

[10] T. F. Cootes, G. J. Edwards, and C. J. Taylor, "Active Appearance Models," in *Proceedings of European Conference on Computer Vision*, 1998, vol. 23, no. 6, pp. 681–685.

[11] G. J. Edwards, C. J. Taylor, and T. F. Cootes, "Interpreting Face Images using Active Appearance Models," in *International Conference on Automatic Face and Gesture Recognition*, 1998, pp. 300–305.

[12] T. F. Cootes, "An Introduction to Active Shape Models," in *Image Processing and Analysis*, vol. 243657, E. R. Baldock and J. Grahanm, Eds. Oxford University Press, 2000, pp. 223–248.

[13] M. Fleute and S. Lavallée, "Nonrigid 3-d/2-d registration of images using statistical models," *Med. Image Comput. Comput.*, vol. LNCS1679, pp. 138–147, 1999.

[14] G. Zheng, S. Gollmer, S. Schumann, X. Dong, T. Feilkas, and M. Á. González Ballester, "A 2D/3D correspondence building method for reconstruction of a patient-specific 3D bone surface model using point distribution models and calibrated X-ray images," *Med. Image Anal.*, vol. 13, no. 6, pp. 883–899, 2009.

[15] N. Baka, B. L. Kaptein, M. de Bruijne, T. van Walsum, J. E. Giphart, W. J. Niessen, and B. P. F. Lelieveldt, "2D-3D shape reconstruction of the distal femur from stereo X-ray imaging using statistical shape models," *Med. Image Anal.*, vol. 15, no. 6, pp. 840–850, 2011.

[16] L. Belenguer Querol, P. Büchler, D. Rueckert, L. P. Nolte, and M. Á. González Ballester, "Statistical finite element model for bone shape and biomechanical properties," in *MICCAI*, 2006, vol. 9, no. LNCS 4190, pp. 405–411.

[17] O. Ahmad, K. Ramamurthi, K. E. Wilson, K. Engelke, R. L. Prince, and R. H. Taylor, "Volumetric DXA (VXA): A new method to extract 3D information from multiple in vivo DXA images," *J. Bone Miner. Res.*, vol. 25, no. 12, pp. 2744–2751, 2010.

[18] T. Whitmarsh, L. Humbert, M. De Craene, L. M. Del Rio Barquero, A. F. Frangi, L. M. Del Río Barquero, and A. F. Frangi,

"Reconstructing the 3D shape and bone mineral density distribution of the proximal femur from dual-energy x-ray absorptiometry," *IEEE Trans. Med. Imaging*, vol. 30, no. 12, pp. 2101–2114, 2011.

[19] S. P. Väänänen, L. Grassi, G. Flivik, J. S. Jurvelin, and H. Isaksson, "Generation of 3D shape, density, cortical thickness and finite element mesh of proximal femur from a DXA image," *Med. Image Anal.*, vol. 24, pp. 125–134, 2015.

[20] L. Humbert, Y. Martelli, R. Fonolla, M. Steghofer, S. Di Gregorio, J. Malouf, J. Romera, and L. M. Del Río Barquero, "3D-DXA: Assessing the Femoral Shape, the Trabecular Macrostructure and the Cortex in 3D from DXA images," *IEEE Trans. Med. Imaging*, vol. 36, no. 1, pp. 27–39, 2017.

[21] T. Whitmarsh, L. Humbert, L. M. Del Río Barquero, S. Di Gregorio, and A. F. Frangi, "3D reconstruction of the lumbar vertebrae from anteroposterior and lateral dual-energy X-ray absorptiometry," *Med. Image Anal.*, vol. 17, no. 4, pp. 475–487, 2013.

[22] ISCD, "Adult Official Positions of the International Society for Clinical Densitometry (ISCD)." 2015.

[23] R. Winzenrieth, L. Humbert, S. Di Gregorio, J. Rodriguez-Tolra, E. Bonel, M. García, and L. M. Del Río Barquero, "Effects of osteoporosis drug treatments on cortical and trabecular bone in the femur using DXA-based 3D modeling," *Osteoporos. Int.*, 2018.

[24] J. Clotet, Y. Martelli, S. Di Gregorio, L. M. Del Río Barquero, and L. Humbert, "Structural Parameters of the Proximal Femur by 3-Dimensional Dual-Energy X-ray Absorptiometry Software: Comparison With Quantitative Computed Tomography," *J. Clin. Densitom.*, no. 10, pp. 1–13, 2017.

[25] WHO Scientific Group, "Prevention and management of osteoporosis," 2000.

[26] J. A. Kanis, L. J. Melton, C. Christiansen, C. C. Johnston, and N. Khaltaev, "The diagnosis of osteoporosis," *J. Bone Miner. Res.*,

vol. 9, no. 8, pp. 1137–1141, 1994.

[27] T. D. Rachner, S. Khosla, and L. C. Hofbauer, "Osteoporosis: Now and the future," *Lancet*, vol. 377, no. 9773, pp. 1276–1287, 2011.

[28] J. A. Kanis, "Diagnosis of osteoporosis and assessment of fracture risk," *Lancet*, vol. 359, no. 9321, pp. 1929–1936, 2002.

[29] J. A. Kanis, "Osteoporosis III: Diagnosis of osteoporosis and assessment of fracture risk," *Lancet*, vol. 359, pp. 1929–1936, 2002.

[30] A. Svedbom, E. Hernlund, M. Ivergård, J. Compston, C. Cooper, J. Stenmark, E. V. McCloskey, B. Jönsson, and J. A. Kanis, "Osteoporosis in the European Union: A compendium of country-specific reports," *Arch. Osteoporos.*, vol. 8 (1-2), no. 137, 2013.

[31] N. C. Harvey and E. V. McCloskey, "Gaps and solutions in bone health," *International Osteoporosis Foundation*, 2016. [Online]. Available: https://www.iofbonehealth.org/thematic-report-2016.

[32] O. Johnell and J. A. Kanis, "An estimate of the worldwide prevalence and disability associated with osteoporotic fractures," *Osteoporos. Int.*, vol. 17, no. 12, pp. 1726–1733, 2006.

[33] E. Hernlund, A. Svedbom, M. Ivergård, J. Compston, C. Cooper, J. Stenmark, E. V. McCloskey, B. Jönsson, and J. A. Kanis, "Osteoporosis in the European Union: Medical management, epidemiology and economic burden: A report prepared in collaboration with the International Osteoporosis Foundation (IOF) and the European Federation of Pharmaceutical Industry Associations (EFPIA)," *Arch. Osteoporos.*, vol. 8, no. 1–2, p. 136, 2013.

[34] J. A. Cauley, N. S. Wampler, J. M. Barnbhart, L. Wu, M. Allison, Z. Chen, S. Hendrix, J. Robbins, R. D. Jackson, J. M. Barnhart, L. Wu, M. Allison, Z. Chen, S. Hendrix, J. Robbins, and R. D. Jackson, "Incidence of fractures compared to cardiovascular

disease and breast cancer: the Women's Health Initiative Observational Study," *Osteoporos. Int.*, vol. 19, no. 12, pp. 1717–1723, 2008.

[35] J. A. Kanis, E. V. McCloskey, H. Johansson, C. Cooper, R. Rizzoli, and J. Y. Reginster, "European guidance for the diagnosis and management of osteoporosis in postmenopausal women," *Osteoporos. Int.*, vol. 24, no. 1, pp. 23–57, 2013.

[36] C. Cyrus, E. J. Atkinson, W. M. O'Fallon, and L. J. Melton, "Incidence of clinically diagnosed vertebral fractures: A population-based study in rochester, minnesota, 1985-1989," *J. Bone Miner. Res.*, vol. 7, no. 2, pp. 221–227, 1992.

[37] J. A. Kanis, H. Johansson, A. Oden, and E. V. McCloskey, "Assessment of fracture risk," *Eur. J. Radiol.*, vol. 71, no. 3, pp. 392–397, 2009.

[38] D. Marshall and H. Wedel, "Meta-analysis of how well measures of bone mineral density predict occurrence of osteoporotic fractures," *BMJ*, vol. 312, no. May, pp. 1254–59, 1996.

[39] P. Ammann, R. Rizzoli, and P. A. Æ. R. Rizzoli, "Bone strength and its determinants," *Osteoporos. Int.*, vol. 14, no. S3, pp. 13–18, 2003.

[40] E. S. Siris, Y.-T. Chen, T. A. Abbott, E. Barrett-Connor, P. D. Miller, L. E. Wehren, and M. L. Berger, "Bone Mineral Density Thresholds for Pharmacological Intervention to Prevent Fractures," *Arch. Intern. Med.*, vol. 164, no. 10, pp. 1108–1112, 2004.

[41] J. S. Bauer and T. M. Link, "Advances in osteoporosis imaging," *Eur. J. Radiol.*, vol. 71, no. 3, pp. 440–449, 2009.

[42] NIH Consensus Development Panel on Osteoporosis Prevention, "Osteoporosis: prevention, diagnosis, and management," *Am. J. Med.*, vol. 285, no. 6, pp. 785–95, 2001.

[43] H. K. Genant, C. Y. Wu, C. van Kuijk, and M. C. Nevitt, "Vertebral Fracture Assessment Using a Semiquantitative

Technique," *J. Bone Miner. Res.*, vol. 8, no. 9, pp. 1137–1148, 1993.

[44] R. E. Small, "Uses and limitations of bone mineral density measurements in the management of osteoporosis.," *MedGenMed*, vol. 7, no. 2, p. 3, 2005.

[45] G. M. Blake and I. Fogelman, "Technical principles of dual energy x-ray absorptiometry," in *Seminars in Nuclear Medicine*, 1997, vol. 27, no. 3, pp. 210–228.

[46] Radiological Society of North America, "Radiologyinfo," 2017. [Online]. Available: http://www.radiologyinfo.org/en/info.cfm?pg=safety-xray.

[47] K. Engelke, J. E. Adams, G. Armbrecht, P. Augat, C. E. Bogado, M. L. Bouxsein, D. Felsenberg, M. Ito, S. Prevrhal, D. B. Hans, and E. M. Lewiecki, "Clinical Use of Quantitative Computed Tomography and Peripheral Quantitative Computed Tomography in the Management of Osteoporosis in Adults: The 2007 ISCD offical positions," *J. Clin. Densitom.*, vol. 11, no. 1, pp. 123–162, 2008.

[48] M. A. Krieg, R. Barkmann, S. Gonnelli, A. Stewart, D. C. Bauer, L. M. Del Río Barquero, J. J. Kaufman, R. S. Lorenc, P. D. Miller, W. P. Olszynski, C. Poiana, A. M. Schott, E. M. Lewiecki, D. B. Hans, L. M. del Río Barquero, J. J. Kaufman, R. S. Lorenc, P. D. Miller, W. P. Olszynski, C. Poiana, A. M. Schott, E. M. Lewiecki, and D. B. Hans, "Quantitative Ultrasound in the Management of Osteoporosis: The 2007 ISCD Official Positions," *J. Clin. Densitom.*, vol. 11, no. 1, pp. 163–187, 2008.

[49] J. J. Carey and B. Buehring, "Current imaging techniques in osteoporosis," *Clin. Exp. Rheumatol.*, pp. 115–126, 2018.

[50] P. Martineau and W. D. Leslie, "Trabecular bone score (TBS): Method and applications," *Bone*, vol. 104, pp. 66–72, 2017.

[51] Y. Bala, R. Zebaze, and E. Seeman, "Role of cortical bone in bone fragility," *Curr. Opin. Rheumatol.*, vol. 27, no. 4, pp. 406–13, 2015.

[52] S. Prevrhal, J. C. Fox, J. A. Shepherd, and H. K. Genant, "Accuracy of CT-based thickness measurement of thin structures : Modeling of limited spatial resolution in all three dimensions," *Med. Phys.*, vol. 30, no. 1, pp. 1–8, 2003.

[53] F. L. Bookstein, *Morphometric Tools for Landmark Data: Geometry and Biology*. Cambridge University Press, 1991.

[54] I. L. Dryden and K. V Mardia, *Statistical shape analysis*. Chichester [u.a.]: Wiley, 1998.

[55] J. Jeong, S. M. Pizer, and S. Ray, "Statistics on Anatomic Objects Reflecting Inter-Object Relations," *1st MICCAI Work. Math. Found. Comput. Anat. Geom. Stat. Regist. Methods Model. Biol. Shape Var.*, 2006.

[56] H. Blum, "Biological shape and visual science. I.," *J. Theor. Biol.*, vol. 38, no. 2, pp. 205–287, Feb. 1973.

[57] F. Poupon, J.-F. Mangin, D. Hasboun, C. Poupon, I. Magnin, and V. Frouin, "Multi-object deformable templates dedicated to the segmentation of brain deep structures," in *Medical Image Computing and Computer-Assisted Intervention --- MICCAI'98: First International Conference Cambridge, MA, USA, October 11--13, 1998 Proceedings*, W. M. Wells, A. Colchester, and S. Delp, Eds. Berlin, Heidelberg: Springer Berlin Heidelberg, 1998, pp. 1134–1143.

[58] M. E. Leventon, W. E. L. Grimson, and O. Faugeras, "Statistical shape influence in geodesic active contours," in *IEEE Conference on Computer Vision and Pattern Recognition*, 2000, vol. 1, pp. 316–323.

[59] C. Brechbühler, G. Gerig, and O. Kübler, "Parametrization of Closed Surfaces for 3-D Shape Description," *Comput. Vis. Image Underst.*, vol. 61, no. 2, pp. 154–170, 1995.

[60] L. H. Staib and J. S. Duncan, "Deformable Fourier models for surface finding in 3D images.," in *Visualization in Biomedical Computing*, 1992, vol. 1808 SPIE, pp. 90–104.

[61] T. Heimann and H.-P. Meinzer, "Statistical shape models for 3D

medical image segmentation: A review," *Med. Image Anal.*, vol. 13, no. 4, pp. 543–563, 2009.

[62] P. Besl and N. McKay, "A Method for Registration of 3-D Shapes," *IEEE Trans. Pattern Anal. Mach. Intell.*, vol. 14, no. 2, pp. 239–256, 1992.

[63] S. Gold, a. Rangarajan, C. P. Lu, and S. Pappu, "New algorithms for 2D and 3D point matching:: pose estimation and correspondence," *Pattern Recognit.*, vol. 31, no. 8, pp. 1019–31, 1998.

[64] R. H. Davies, C. J. Twining, T. F. Cootes, J. C. Waterton, and C. J. Taylor, "A minimum description length approach to statistical shape modeling," *IEEE Trans. Med. Imaging*, vol. 21, no. 5, pp. 525–537, 2002.

[65] T. F. Cootes, C. J. Twining, V. Petrovic, R. Schestowitz, and C. J. Taylor, "Groupwise construction of appearance models using piece-wise affine deformations," in *British Machine Vision Conference*, 2005, vol. 2, no. Mdl, pp. 879–888.

[66] E. Syrkina, M. Á. González Ballester, and G. Szekely, "Correspondence Establishment in Statistical Modeling of Shapes with Arbitrary Topology," in *IEEE International Conference on Computer Vision*, 2007, pp. 1–7.

[67] Y. Tsin and T. Kanade, "A Correlation-Based Approach to Robust Point Set Registration," in *ECCV*, 2004, vol. 3023 LNCS, pp. 558–569.

[68] B. Jian and B. C. Vemuri, "A Robust Algorithm for Point Set Registration Using Mixture of Gaussians," in *International Conference on Computer Vision*, 2005, vol. 2, pp. 1246–1251.

[69] B. Jian and B. C. Vemuri, "Robust Point Set Registration Using Gaussian Mixture Models," *IEEE Trans. Pattern Anal. Mach. Intell.*, vol. 33, no. 8, pp. 1633–1645, 2011.

[70] A. Myronenko and X. Song, "Point-Set Registration: Coherent Point Drift," *IEEE Trans. Pattern Anal. Mach. Intell.*, vol. 32, no.

12, pp. 2262–2275, 2010.

[71] A. Myronenko, X. Song, and M. Á. Carreira-Perpiñán, "Non-rigid point set registration: Coherent Point Drift," in *Neural Information Processing Systems*, 2007, vol. 19, pp. 1009–1016.

[72] J. C. Gower, "Gerenalized Procustes Analysis," *Psychometirka*, vol. 40, pp. 33–51, 1975.

[73] I. T. Jolliffe, *Principal Component Analysis*. Berlin, Germany, 1986.

[74] M. B. Stegmann and R. Fisker, "On properties of active shape models," *Math. Model.*, 2000.

[75] J. J. Cerrolaza, A. Villanueva, and R. Cabeza, "Shape Constraint Strategies: Novel Approaches and Comparative Robustness," in *British Machine Vision Conference*, 2011, p. 7.1-7.11.

[76] T. F. Cootes and C. J. Taylor, "A mixture model for representing shape variation," *Image Vis. Comput.*, vol. 17, no. October 1997, pp. 567–573, 1999.

[77] G. Ruiz, E. Ramon, J. García, F. M. Sukno, and M. A. G. Ballester, "Weighted regularized statistical shape space projection for breast 3D model reconstruction," *Med. Image Anal.*, vol. 47, pp. 164–179, 2018.

[78] M. Á. González Ballester, M. G. Linguraru, M. Reyes Aguirre, and N. Ayache, "On the adequacy of principal factor analysis for the study of shape variability," in *SPIE*, 2005, vol. 5747, p. 1393.

[79] M. Reyes, M. Á. González Ballester, R. M. Summers, and M. G. Linguraru, "Interpretability of Anatomical Variability Analysis of Abdominal Organs via Clusterization of Decomposition Modes," in *IEEE Engineering in Medicine and Biology Society*, 2009, pp. 355–358.

[80] M. Üzümcü, A. F. Frangi, J. H. C. Reiber, and B. P. F. Lelieveldt, "Independent component analysis in statistical shape models," *Med. Imaging*, vol. 31, pp. 375–383, 2003.

[81] C. J. Twining and C. J. Taylor, "Kernel Principal Component

Analysis and the construction of non-linear Active Shape Models.," in *British Machine Vision Conference*, 2001.

[82] S. T. Roweis and L. K. Saul, "Nonlinear dimensionality reduction by locally linear embedding.," *Science (80-.).*, vol. 290, no. 5500, pp. 2323–2326, 2000.

[83] M. Belkin and P. Niyogi, "Laplacian eigenmaps for dimensionality reduction and data representation," 2002.

[84] M. Turk and A. Pentland, "Face recognition using eigenfaces," *J. Cogn. Neurosci.*, vol. 3, no. 1, 1991.

[85] U. Bagci, X. Chen, and J. K. Udupa, "Hierarchical scale-based multiobject recognition of 3-D anatomical structures," *IEEE Trans. Med. Imaging*, vol. 31, no. 3, pp. 777–789, 2012.

[86] A. A. Asl and H. Soltanian-Zadeh, "Constrained optimization of nonparametric entropy-based segmentation of brain structures," *2008 5th IEEE Int. Symp. Biomed. Imaging From Nano to Macro, Proceedings, ISBI*, pp. 41–44, 2008.

[87] J. Yao and R. M. Summers, "Statistical location model for abdominal organ localization.," *Med. Image Comput. Comput. Assist. Interv.*, vol. 12, no. Pt 2, pp. 9–17, 2009.

[88] S. Jung and J. S. Marron, "PCA CONSISTENCY IN HIGH DIMENSION, LOW SAMPLE SIZE CONTEXT," *Ann. Stat.*, vol. 37, no. 6B, pp. 4104–4130, 2009.

[89] N. Duta and M. Sonka, "Segmentation and interpretation of MR brain images: an improved active shape model.," *IEEE Trans. Med. Imaging*, vol. 17, no. 6, pp. 1049–1062, 1998.

[90] A. F. Frangi, D. Rueckert, J. A. Schnabel, and W. J. Niessen, "Automatic construction of multiple-object three-dimensional statistical shape models: Application to cardiac modeling," *IEEE Trans. Med. Imaging*, vol. 21, no. 9, pp. 1151–1166, 2002.

[91] B. van Ginneken, M. B. Stegmann, and M. Loog, "Segmentation of anatomical structures in chest radiographs using supervised

methods: a comparative study on a public database," *Med. Image Anal.*, vol. 10, no. 1, pp. 19–40, 2006.

[92] J. Fripp, S. Crozier, S. K. Warfield, and S. Ourselin, "Automatic segmentation of the bone and extraction of the bone-cartilage interface from magnetic resonance images of the knee.," *Phys. Med. Biol.*, vol. 52, no. 6, pp. 1617–1631, Mar. 2007.

[93] P. P. Smyth, C. J. Taylor, and J. E. Adams, "Automatic measurement of vertebral shape using active shape models," *Image Vis. Comput.*, vol. 15, no. 8, pp. 575–581, 1997.

[94] T. Schwarz, T. Heimann, D. Lossnitzer, C. Mohrhardt, H. Steen, U. Rietdorf, I. Wolf, and H.-P. Meinzer, "Multiobject segmentation using coupled shape space models," *Proc. SPIE*, vol. 7623. p. 76233V–76233V–8, 2010.

[95] D. Li, P. Zang, X. Chai, Y. Cui, R. Li, and L. Xing, "Automatic multiorgan segmentation in CT images of the male pelvis using region-specific hierarchical appearance cluster models.," *Med. Phys.*, vol. 43, no. 10, p. 5426, Oct. 2016.

[96] A. Mansoor, J. J. Cerrolaza, G. Perez, E. Biggs, G. Nino, and M. G. Linguraru, "Marginal shape deep learning: applications to pediatric lung field segmentation," *Proc. SPIE*, vol. 10133. pp. 1013304–1013306, 2017.

[97] C. J. F. F. Reyneke, M. Luthi, V. Burdin, T. S. Douglas, T. Vetter, and T. E. M. M. Mutsvangwa, "Review of 2D/3D reconstruction using statistical shape and intensity models and X-ray image synthesis: towards a unified framework," *IEEE Rev. Biomed. Eng.*, vol. (in press), pp. 1–17, 2018.

[98] P. Markelj, D. Tomazevic, B. Likar, and F. Pernus, "A review of 3D/2D registration methods for image-guided interventions," *Med. Image Anal.*, vol. 16, no. 3, pp. 642–661, 2012.

[99] S. Benameur, M. Mignotte, S. Parent, H. Labelle, W. Skalli, and J. A. de Guise, "3D/2D registration and segmentation of scoliotic vertebrae using statistical models," *Comput. Med. Imaging Graph.*, vol. 27, no. 5, pp. 321–337, 2003.

[100] A. Hurvitz and L. Joskowicz, "Registration of a CT-like atlas to fluoroscopic X-ray images using intensity correspondences," *Int. J. Comput. Assist. Radiol. Surg.*, vol. 3, pp. 493–504, 2008.

[101] G. Zheng, M. Á. González Ballester, M. Styner, and L. P. Nolte, "Reconstruction of Patient-Specific 3D Bone Surface from 2D Calibrated Fluoroscopic Images," in *MICCAI*, 2006, pp. 25–32.

[102] J. Boisvert, F. Cheriet, X. Pennec, H. Labelle, N. Ayache, J. Boisvert^ast, F. Cheriet, X. Pennec, H. Labelle, N. Ayache, J. Boisvert, F. Cheriet, X. Pennec, H. Labelle, and N. Ayache, "Articulated spine models for 3-D reconstruction from partial radiographic data," *IEEE Trans. Biomed. Eng.*, vol. 55, no. 11, pp. 2565–2574, 2008.

[103] D. C. Moura, J. Boisvert, J. G. Barbosa, H. Labelle, and J. M. R. S. Tavares, "Fast 3D reconstruction of the spine from biplanar radiographs using a deformable articulated model," *Med. Eng. Phys.*, vol. 33, no. 8, pp. 924–933, 2011.

[104] H. Lamecker, T. H. Wenckebach, H. Hans-Christian, and H.-C. Hege, "Atlas-based 3D-Shape Reconstruction from X-Ray Images," in *ICPR*, 2006, vol. 1, pp. 371–374.

[105] T. S. Tang and R. E. Ellis, "2D/3D deformable registration using a hybrid atlas," *Med Image Comput Comput Assist Interv*, vol. 8, no. Pt 2, pp. 223–230, 2005.

[106] L. Humbert, Y. Martelli, R. Fonollà, M. Steghöfer, S. Di Gregorio, and L. M. L. M. del Río Barquero, "3D-DXA: Analyzing the Femoral Shape, the Trabecular Macrostructure and the Cortical layer in 3D from DXA images," *IEEE Trans. Med. Imaging*, vol. 36, no. 1, pp. 27–39, 2017.

[107] N. Sarkalkan, H. Weinans, and A. A. Zadpoor, "Statistical shape and appearance models of bones," *Bone*, vol. 60, pp. 129–140, 2014.

[108] T. N. Hangartner, "Thresholding technique for accurate analysis of density and geometry in QCT, pQCT and mCT images," *J. Musculoskelet. Neuronal Interact.*, vol. 7, no. 1, pp. 9–16, 2007.

[109] L. Humbert, J. Hazrati Marangalou, L. M. Del Río Barquero, G. H. van Lenthe, and B. van Rietbergen, "Technical Note: Cortical thickness and density estimation from clinical CT using a prior thickness-density relationship," *Med. Phys.*, vol. 43, no. 4, pp. 1945–1954, 2016.

[110] H. Chen, X. Zhou, H. Fujita, M. Onozuka, and K.-Y. Kubo, "Age-related changes in trabecular and cortical bone microstructure," *Int. J. Endocrinol.*, vol. 2013, no. 213234, 2013.

[111] H. Ritzel, M. Amling, M. Pösl, M. Hahn, and G. Delling, "The thickness of human vertebral cortical bone and its changes in aging and osteoporosis: a histomorphometric analysis of the complete spinal column from thirty-seven autopsy specimens.," *J. Bone Miner. Res.*, vol. 12, no. 1, pp. 89–95, 1997.

[112] H. Hassanpour, N. Samadiani, and S. M. Mahdi Salehi, "Using morphological transforms to enhance the contrast of medical images," *Egypt. J. Radiol. Nucl. Med.*, vol. 46, no. 2, pp. 481–489, 2015.

[113] A. Top, G. Hamarneh, and R. Abugharbieh, "Spotlight: Automated confidence-based user guidance for increasing efficiency in interactive 3D image segmentation," in *MICCAI*, 2010, vol. 6533 LNCS, pp. 204–213.

[114] A. Top, G. Hamarneh, and R. Abugharbieh, "Active learning for interactive 3D image segmentation.," in *MICCAI*, 2011, vol. 14, pp. 603–10.

[115] F. L. Bookstein, "Principal warps: Thin-Plate Splines and the decomposition of deformations," in *IEEE Transactions on Pattern Analysis and Machine Intelligence*, 1989, vol. 11, no. 6, pp. 567–585.

[116] W. H. Press, B. Flannery, S. Teukolsky, and W. Vetterling, *Numerical recipes in C: The art of scientic computing*. Cambridge University Press, 1992.

[117] D. L. Schneider, R. Bettencourt, and E. Barrett-Connor, "Clinical Utility of Spine Bone Density in Elderly Women," *J. Clin. Densitom.*, vol. 9, no. 3, pp. 255–260, 2006.

[118] G. Ballane, J. A. Cauley, M. M. Luckey, and G. El-Hajj Fuleihan, "Worldwide prevalence and incidence of osteoporotic vertebral fractures," *Osteoporos. Int.*, vol. 28, no. 5, pp. 1531–1542, 2017.

[119] S. R. Cummings and L. J. Melton, "Epidemiology and outcomes of osteoporotic fractures," *Lancet*, vol. 359, no. 9319, pp. 1761–1767, 2002.

[120] T. Jalava, S. Sarna, L. Pylkka, P. Selby, M. Davies, J. E. Adams, R. M. Francis, J. Robinson, and E. V. McCloskey, "Association Between Vertebral Fracture and Increased Mortality in Osteoporotic Patients," *J. Bone Miner. Res.*, vol. 18, no. 7, pp. 1254–1259, 2003.

[121] H. P. Dimai, "Use of dual-energy X-ray absorptiometry (DXA) for diagnosis and fracture risk assessment; WHO-criteria, T- and Z-score, and reference databases," *Bone*, vol. 104, pp. 39–43, 2017.

[122] C. M. Gordon, T. F. Lang, P. Augat, and H. K. Genant, "Image-based assessment of spinal trabecular bone structure from high-resolution CT images," *Osteoporos. Int.*, vol. 8, no. 4, pp. 317–325, 1998.

[123] N. Li, X. M. Li, L. Xu, W. J. Sun, X. G. Cheng, and W. Tian, "Comparison of QCT and DXA: Osteoporosis detection rates in postmenopausal women," *Int. J. Endocrinol.*, vol. 2013, pp. 5–10, 2013.

[124] K. Engelke, C. Libanati, T. Fuerst, P. Zysset, and H. K. Genant, "Advanced CT based in vivo methods for the assessment of bone density, structure, and strength," *Curr. Osteoporos. Rep.*, vol. 11, no. 3, pp. 246–255, 2013.

[125] D. Chalhoub, E. S. Orwoll, P. M. Cawthon, K. E. Ensrud, R. Boudreau, S. Greenspan, A. B. Newman, J. Zmuda, D. C. Bauer, S. R. Cummings, and J. A. Cauley, "Areal and volumetric bone mineral density and risk of multiple types of fracture in older men," *Bone*, vol. 92, pp. 100–106, 2016.

[126] L. J. Melton, B. L. Riggs, T. M. Keaveny, S. J. Achenbach, P. F.

Hoffmann, J. J. Camp, P. A. Rouleau, M. L. Bouxsein, S. Amin, E. J. Atkinson, R. A. Robb, and S. Khosla, "Structural Determinants of Vertebral Fracture Risk," *J. Bone Miner. Res.*, vol. 22, no. 12, pp. 1885–1892, 2007.

[127] D. E. Anderson, S. Demissie, B. T. Allaire, A. G. Bruno, D. L. Kopperdahl, and T. M. Keaveny, "The associations between QCT-based vertebral bone measurements and prevalent vertebral fractures depend on the spinal locations of both bone measurement and fracture," *Osteoporos. Int.*, vol. 25, no. 2, pp. 559–566, 2014.

[128] S. Grampp, H. K. Genant, A. Mathur, P. Lang, M. Jergas, M. Takada, C. C. Glüer, Y. Lu, and M. Chavez, "Comparisons of noninvasive bone mineral measurements in assessing age- related loss, fracture discrimination, and diagnostic classification," *J. Bone Miner. Res.*, vol. 12, no. 5, pp. 697–711, 1997.

[129] D. L. Kopperdahl, T. Aspelund, P. F. Hoffmann, K. Siggeirsdottir, T. B. Harris, and T. M. Keaveny, "Assessment of Incident Spine and Hip Fractures in Women and Men using Finite Element Analysis of CT Scans," *J. Bone Miner. Res.*, vol. 29, no. 3, pp. 570–580, 2014.

[130] X. Wang, A. Sanyal, P. Cawthon, L. Palermo, M. Jekir, J. Christensen, K. E. Ensrud, S. R. Cummings, E. Orwoll, D. Black, and O. Fractures, "Prediction of new clinical vertebral fractures in elderly men using FEA of CT scans," *J. Bone Miner. Res.*, vol. 27, no. 4, pp. 808–816, 2012.

[131] P. Zysset, L. Qin, T. Lang, S. Khosla, W. D. Leslie, J. A. Shepherd, J. T. Schousboe, and K. Engelke, "Clinical Use of Quantitative Computed Tomography–Based Finite Element Analysis of the Hip and Spine in the Management of Osteoporosis in Adults: the 2015 ISCD Official Positions—Part II," *J. Clin. Densitom.*, vol. 18, no. 3, pp. 359–392, Jan. 2015.

[132] K. Imai, I. Ohnishi, T. Matsumoto, S. Yamamoto, and K. Nakamura, "Assessment of vertebral fracture risk and therapeutic effects of alendronate in postmenopausal women using a quantitative computed tomography-based nonlinear

finite element method," *Osteoporos. Int.*, vol. 20, no. 5, pp. 801–810, 2009.

[133] M. López Picazo, A. Magallón Baro, L. M. del Rio Barquero, S. Di Gregorio, Y. Martelli, J. Romera, M. Steghofer, M. A. González Ballester, and L. Humbert, "3D Subject-Specific Shape and Density Estimation of the Lumbar Spine from a Single Anteroposterior DXA Image Including Assessment of Cortical and Trabecular Bone," *IEEE Trans. Med. Imaging*, vol. 37, no. 12, pp. 2651–2662, 2018.

[134] G. Guglielmi, I. Floriani, V. Torri, J. Li, C. van Kuijk, H. K. Genant, and T. F. Lang, "Effect of spinal degenerative changes on volumetric bone mineral density of the central skeleton as measured by quantitative computed tomography," *Acta radiol.*, vol. 46, no. 3, pp. 269–275, 2005.

[135] S. K. Eswaran, A. Gupta, M. F. Adams, and T. M. Keaveny, "Cortical and Trabecular Load Sharing in the Human Vertebral Body," *J. Bone Miner. Res.*, vol. 21, no. 2, pp. 307–314, 2006.

[136] J. P. Roux, J. Wegrzyn, M. E. Arlot, O. Guyen, P. D. Delmas, R. Chapurlat, and M. L. Bouxsein, "Contribution of trabecular and cortical components to biomechanical behavior of human vertebrae: an ex vivo study.," *J. Bone Miner. Res.*, vol. 25, no. 2, pp. 356–361, 2010.

[137] G. M. Treece and A. H. Gee, "Independent measurement of femoral cortical thickness and cortical bone density using clinical CT," *Med. Image Anal.*, vol. 20, no. 1, pp. 249–264, 2015.

[138] M. Van der Klift, C. E. De Laet, E. V McCloskey, A. Hofman, and H. A. Pols, "The incidence of vertebral fractures in men and women: the Rotterdam Study," *J. Bone Miner. Res.*, vol. 17, no. 6, pp. 1051–1056, 2002.

[139] M. J. J. Budoff, W. Khairallah, D. Li, Y. L. Gao, H. Ismaeel, F. R. Flores, J. Child, S. Carson, and S. S. S. Mao, "Trabecular Bone Mineral Density Measurement Using Thoracic and Lumbar Quantitative Computed Tomography," *Acad. Radiol.*, vol. 19, no. 2, pp. 179–183, 2012.

[140] A. Noshchenko, A. Plaseied, V. Patel, E. Burger, T. Baldini, and Y. Luo, "Correlation of vertebral strength topography with 3-dimensional computed tomographic structure," *Spine (Phila. Pa. 1976).*, vol. 38, no. 4, 2013.

[141] T. M. Jackman, A. I. Hussein, A. M. Adams, K. K. Makhnejia, and E. F. Morgan, "Endplate deflection is a defining feature of vertebral fracture and is associated with properties of the underlying trabecular bone," *J. Orthop. Res.*, vol. 32, no. 7, pp. 880–886, 2014.

[142] T. M. Jackman, A. I. Hussein, C. Curtiss, P. M. Fein, A. Camp, L. De Barros, and E. F. Morgan, "Quantitative, 3D Visualization of the Initiation and Progression of Vertebral Fractures Under Compression and Anterior Flexion," *J. Bone Miner. Metab.*, vol. 31, no. 4, pp. 777–788, 2016.

[143] B. C. Silva, S. B. Broy, S. Boutroy, J. T. Schousboe, J. A. Shepherd, and W. D. Leslie, "Fracture Risk Prediction by Non-BMD DXA Measures: the 2015 ISCD Official Positions Part 2: Trabecular Bone Score," *J. Clin. Densitom.*, vol. 18, no. 3, pp. 309–330, Jan. 2015.

[144] S. R. Cummings, W. S. Browner, J. A. Cauley, K. E. Ensrud, J. Scott, and T. M. Vogt, "Bone density at various sites for prediction of hip fractures," *Lancet*, vol. 341, no. 8837, pp. 72–75, 1993.

[145] L. J. Melton, E. J. Atkinson, W. M. O'Fallon, H. W. Wahner, and B. L. Riggs, "Long-term fracture prediction by bone mineral assessed at different skeletal sites," *J. Bone Miner. Res.*, vol. 8, no. 10, pp. 1227–1233, 1993.

[146] K. L. Stone, D. G. Seeley, L. Lui, J. A. Cauley, K. E. Ensrud, W. S. Browner, M. C. Nevitt, and S. R. Cummings, "BMD at Multiple Sites and Risk of Fracture of Multiple Types: Long-Term Results From the Study of Osteoporotic Fractures," *J. Bone Miner. Res.*, vol. 18, no. 11, 2003.

[147] E. Vega, C. Mautalen, H. Gomez, A. Garrido, L. Melo, and A. O. Sahores, "Bone mineral density in patients with cervical and

trochanteric fractures of the proximal femur," *Osteoporos Int*, vol. 1, no. 2, pp. 81–86, 1991.

[148] J. P. Heneghan, P. N. Kirke, B. L. Murphy, E. Darcy, L. Daly, G. J. Bourke, E. Dinn, and J. Masterson, "Evaluation of quantitative CT vertebral bone mineral density measurement and the Singh index in elderly females with hip fractures--a case control study.," *Br. J. Radiol.*, vol. 70, no. 837, pp. 923–8, 1997.

[149] H. Kröger, M. Lunt, J. Reeve, J. Dequeker, J. E. Adams, J. C. Birkenhager, M. Diaz Curiel, D. Felsenberg, L. Hyldstrup, P. Kotzki, A. M. Laval-Jeantet, P. Lips, O. Louis, R. Perez Cano, C. Reiners, C. Ribot, P. Ruegsegger, P. Schneider, P. Braillon, and J. Pearson, "Bone density reduction in various measurement sites in men and women with osteoporotic fractures of spine and hip: The European quantitation of osteoporosis study," *Calcif. Tissue Int.*, vol. 64, no. 3, pp. 191–199, 1999.

[150] T. F. Lang, P. Augat, N. E. Lane, and H. K. Genant, "Trochanteric hip fracture: strong association with spinal trabecular bone mineral density measured with quantitative CT," *Radiology*, vol. 209, no. 2, pp. 525–530, 1998.

[151] S. J. Lee, P. A. Anderson, and P. J. Pickhardt, "Predicting future hip fractures on routine abdominal CT using opportunistic osteoporosis screening measures: A matched case-control study," *Am. J. Roentgenol.*, vol. 209, no. 2, pp. 395–402, 2017.

[152] S. Schwartz and P. Ort, "Trabecular mineral content of the spine in women with hip fracture," *Musculoskelet. Radiol.*, vol. 159, pp. 737–740, 1986.

[153] L. Yang, W. J. M. Udall, E. V. McCloskey, and R. Eastell, "Distribution of bone density and cortical thickness in the proximal femur and their association with hip fracture in postmenopausal women: A quantitative computed tomography study," *Osteoporos. Int.*, vol. 25, no. 1, pp. 251–263, 2014.

[154] G. Holzer, G. Von Skrbensky, L. A. Holzer, and W. Pichl, "Hip fractures and the contribution of cortical versus trabecular bone to femoral neck strength," *J. Bone Miner. Res.*, vol. 24, no. 3, pp.

468–474, 2009.

[155] N. Crabtree, N. Loveridge, M. Parker, N. Rushton, J. Power, K. L. Bell, T. J. Beck, and J. Reeve, "Intracapsular hip fracture and the region-specific loss of cortical bone: Analysis by peripheral quantitative computed tomography," *J. Bone Miner. Res.*, vol. 16, no. 7, pp. 1318–1328, 2001.

[156] J. A. Iorio, A. M. Jakoi, and A. Singla, "Biomechanics of Degenerative Spinal Disorders," *Asian Spine hournal*, vol. 10, no. 2, pp. 377–384, 2016.

[157] M. A. Adams, "Degenerative disc and vertebral disease - basic sciences," *Surgery*, vol. 27, no. 7, pp. 297–300, 2009.

[158] K. E. S. Poole, G. M. Treece, P. M. Mayhew, J. Vaculík, P. Dungl, M. Horák, J. J. Štěpán, and A. H. Gee, "Cortical thickness mapping to identify focal osteoporosis in patients with hip fracture," *PLoS One*, vol. 7, no. 6, pp. 1–7, 2012.

[159] G. M. Treece, A. H. Gee, C. Tonkin, S. K. Ewing, P. M. Cawthon, D. M. Black, and K. E. S. Poole, "Predicting Hip Fracture Type with Cortical Bone Mapping (CBM) in the Osteoporotic Fractures in Men (MrOS) Study," *J. Bone Miner. Res.*, vol. 30, no. 11, pp. 2067–2077, 2015.

[160] J. J. Carey and M. F. Delaney, "Utility of DXA for monitoring, technical aspects of DXA BMD measurement and precision testing," *Bone*, vol. 104, pp. 44–53, 2017.

[161] L. Humbert, R. Winzenrieth, S. Di Gregorio, T. Thomas, L. Vico, J. Malouf, and L. M. del Río Barquero, "3D Analysis of Cortical and Trabecular Bone From Hip DXA:Precision and Trend Assessment Interval in PostmenopausalWomen," *J. Clin. Densitom.*, vol. (in press), 2018.

[162] I. R. Reid, "Glucocorticoid osteoporosis - mechanisms and management," pp. 209–217, 1997.

[163] K. F. Moseley, "Type 2 diabetes and bone fractures," *Curr Opin Endocrinol Diabetes Obes.*, vol. 19, no. 2, pp. 128–135, 2012.

[164] M. de Bruijne, M. T. Lund, L. B. Tankó, P. C. Pettersen, M. Nielsen, M. de Bruijne, M. T. Lund, L. B. Tankó, P. C. Pettersen, and M. Nielsen, "Quantitative vertebral morphometry using neighbor-conditional shape models," *Med. Image Anal.*, vol. 11, no. 5, pp. 503–512, 2007.

[165] M. G. Roberts, E. M. B. Pacheco, R. Mohankumar, T. F. Cootes, and J. E. Adams, "Detection of vertebral fractures in DXA VFA images using statistical models of appearance and a semi-automatic segmentation," *Osteoporos. Int.*, vol. 21, no. 12, pp. 2037–2046, 2010.

[166] International Osteoporosis Foundation, "Osteoporosis," 2015. [Online]. Available: http://www.iofbonehealth.org/osteoporosis.

ACKNOWLEDGEMENTS

This thesis would not have been possible without all the people who helped me along the way.

Firstly, I would like to express my sincere gratitude to my supervisors, Prof. Miguel Ángel Gónzalez and Dr Ludovic Humbert, for providing me with the unique opportunity to work in this Industrial phD program and for their constant encouragement which was vital throughout all the stages of my dissertation. I would like to especially thank Prof. Miguel Ángel Gónzalez for his patience and guidance throughout this thesis, regardless of the constant changes in the direction. I would like to especially thank Dr. Ludovic Humbert for his day-to-day guidance. He spent endless hours reviewing my research papers and giving me excellent suggestions, which always resulted in improved versions of the documents.

I am very thankful to all my colleagues (past and present) of Galgo Medical. Thanks for their continuous support, delicious breakfasts, interesting conversations and fun lunches. I am especially grateful to Alba, Julia and Soraya for their contribution of this thesis. The ocean would be nothing without the drops of water that make it up.

I owe my deepest gratitude to Luis Del Río and Silvana Di Gregorio; they managed to collect a vast amount of people as volunteer in this research. I am also indebted to them for their clinical advice, without which this thesis would not make sense. My sincere appreciation to Luis Del Río for his enthusiasm to motivate me and continuous support.

I would like to express my deepest gratitude to all my family and friends who, wherever they were (Férez, Letur, Barcelona…), they listened to me, understood and encouraged me not to ever give up. The distance has not prevented them from being with me both in the good times and in the hard times.

My sincere appreciation to my yoguinis. You know how much your support meant to me throughout this year. I could not have finished this journey without your friendship.

Special thanks to my parents, Matías and Josefa, for all the unconditional support they have always given me. I am very grateful to them for teaching me by example, to work and fight to get my dreams. Thanks also to the support and encouragement of my sister Virginia, and her visits that make me so happy. I am very thankful to my new family, Téllez Gabriel, for your warm hospitality and moral support.

Heartfelt thanks to the members of my family who are no longer with us, especially my aunt Matilde. She unconditional love has come to me from wherever she is to continue fighting even in the worst moments.

Thanks to my immune system, although it has put a lot of bumps in my way, in the end it has allowed me to fulfill my dream. Warriors with IBD, nothing stops us!

I could no leave to thanks to Miku. Although it does not understand any of this, he has not separated from me during the whole thesis.

Finally, I would like to dedicate this work to Joan. This thesis is as much his as mine. I cannot imagine how I would have gone through this without his support. His love gave me the strength to face every obstacle I encountered. Thanks for not stopping to believe in me no matter what.

Gracias a todos por vuestro apoyo incondicional, por alegraros por mí en los buenos momentos y por darme ánimo en los no tan buenos. Sin vosotros no podría haber llegado donde estoy.

Namasté

PUBLICATIONS

Journal papers

1. **M. López Picazo**, A. Magallón Baro, L. M. del Río Barquero, S. Di Gregorio, Y. Martelli, J. Romera, M. Steghöfer, M. A. González Ballester, and L. Humbert."3D Subject-Specific Shape and Density Estimation of the Lumbar Spine from a Single Anteroposterior DXA Image Including Assessment of Cortical and Trabecular Bone", IEEE Transactions on Medical Imaging, vol. 37, no. 12, pg. 2651-2662, 2018.

2. **M. López Picazo,** L. Humbert, S. Di Gregorio, M. A. González Ballester, and L. M. del Río Barquero. "Discrimination of osteoporosis-related vertebral fractures by DXA-derived 3D measurements: A retrospective case-control study, Osteoporosis International (Under review).

3. **M. López Picazo**, L. Humbert, R. Winzenrieth, S. Di Gregorio, M. A. González Ballester, and L. M. del Río Barquero. "Association between osteoporotic femoral neck fractures and DXA-derived 3D measurements at lumbar spine: A case-control study", Bone (Submitted).

4. J. Cerrolaza, **M. López Picazo**, L. Humbert, Y. Sato, D. Rueckert, M. A. González Ballester, M. G. Linguraru. "Computational Anatomy for Multi-Organ Analysis in Medical Imaging: A Review", Medical Image Analysis (Under review).

Conference abstracts

1. **M. López Picazo**, L. Humbert, A. Magallón, L. M. del Rio, S. Di Gregorio, M. A. Gonzalez Ballester. "3D-DXA Spine: Modelling the lumbar Spine in 3D from DXA images," ASBMR 2016 Annual Meeting.

2. A. Magallón Baro, **M. López Picazo**, L. M. del Rio, S. Di Gregorio, M. A. González Ballester, L. Humbert. "*Medidas sobre la geometría y la densidad mineral ósea de la columna lumbar obtenidas mediante la tecnología 3D-DXA*", SEIOMM 2016.

3. **M. Lopez Picazo**, L. Humbert, M. A. Gonzalez Ballester, L. M. Del Rio, R. Winzenrieth, S. Di Gregorio. "Changes in volumetric BMD and cortical thickness measured by 3D-DXA in the lumbar spine after 24 months of Denosumab treatment", ASBMR 2017 Annual Meeting.

4. **M. Lopez Picazo**, L. Humbert, S. Di Gregorio, M. A. Gonzalez Ballester, L. Del Rio. "Can DXA-derived 3D measurements at the lumbar spine predict thoracic spine fractures?", ASBMR 2018 Annual Meeting. *SEIOMM-ASBMR award

CURRICULUM VITAE

Mirella López Picazo was born in Férez, Albacete. She received a BSc in Telecommunication Engineering from *Universidad Politécnica de Valencia* in 2010. During her studies, she did 9-month stay at Lund University, Sweden. She worked as Knowledge Transfer Partnership Associate between the University of Portsmouth and Karis Ltd., United Kingdom, during which she carried out management and research tasks in the development of an intelligent system of care for the elderly. She received 'La Caixa' scholarship to study a M.Sc. in Spain in 2011. She received her M.Sc. in Biomedical Engineering from both the *Universitat de Barcelona* and *Universitat Politècnica de Catalunya* in 2013. She worked as a junior research at the Institute for Bioengineering of Catalonia, focusing her research in new methods of medical diagnosis from biomedical signals. She joined the research group SIMBioSys at *Universitat Pompeu Fabra* and the company *Galgo Medical*, in 2015, as Industrial Ph.D student under the supervision of Prof. Miguel Ángel Gónzalez Ballester and Dr. Ludovic Humbert. Her work, carried out within the framework of the European project EuroStarts and Industrial Phs program, is focused on development and clinical evaluation of methods to analyze in 3D the bone shape and density of the lumbar spine.

Scan this QR code to visualize
a graphical abstract.